UNIVERSITY OF CALIFORNIA, SAN DIEGO

The Sadovskii Vortex

A dissertation submitted in partial satisfaction of the
requirements for the degree
Doctor of Philosophy

in

Engineering Sciences (Aerospace Engineering)

by

Daniel Victor Freilich

Committee in charge:

Stefan Llewellyn Smith, Chair
George Carnevale
Myrl Hendershott
Alison Marsden
Forman Williams

2016

The dissertation of Daniel Victor Freilich is approved, and it is acceptable in quality and form for publication on microfilm and electronically:

_____

_____

_____

_____

_____

Chair

University of California, San Diego

2016

TABLE OF CONTENTS

LIST OF FIGURES

ACKNOWLEDGEMENTS

I would like to thank Stefan Llewellyn Smith first and foremost. It has been a pleasure to work with him, and he has taught me more than I ever imagined I would know about math. I would also like to thank Darren Crowdy for many helpful discussions over the years.

I would be a very different person if I had never discovered the joys of track cycling at UCSD, and I'd like to thank the whole UCSD Cycling Team for all the fun times on the road and velodromes.

My family has always been important in getting me to where I am today. I wouldn't be here without all of you, and I hope you all know how grateful I am for all the support you've given me.

Chapters 2, 3, and 4 are currently being prepared for submission for publication. Freilich, Daniel; Llewellyn Smith, Stefan. "The Sadovskii Vortex in Strain". The dissertation author was the primary investigator and author of this material.

Chapter 5 is currently being prepared for submission for publication. Freilich, Daniel; Llewellyn Smith, Stefan. "The Sadovskii Vortex in Strain with Surface Tension". The dissertation author was the primary investigator and author of this material.

VITA

2010	B. S. in Physics *cum laude*, Amherst College
2011	M. S. in Engineering Sciences (Aerospace Engineering), University of California, San Diego
2016	Ph. D. in Engineering Sciences (Aerospace Engineering), University of California, San Diego

ABSTRACT OF THE DISSERTATION

The Sadovskii Vortex

by

Daniel Victor Freilich

Doctor of Philosophy in Engineering Sciences (Aerospace Engineering)

University of California, San Diego, 2016

Stefan Llewellyn Smith, Chair

The point vortex has been used as a simple model for flows with circulation, and has been desingularized into vortex patches and vortex sheets. In this work, we investigate the steady states of a combination of these two formulations, the Sadovskii vortex. The Sadovskii vortex is a uniform patch of vorticity surrounded by a vortex sheet. Numerical continuation is used to follow families of solutions. In the limiting cases of the vortex patch and vortex sheet cases, we confirm previous research, and in the vortex patch case show new solutions.

In the regime where both sources of circulation exist, we show the relationship between the vortex patch and vortex sheet solution families. The more complicated

vortex patch solution families lead to the simpler vortex sheet solution family due to a splitting of the vortex patch families at bifurcation points in the presence of the vortex sheet. The more circular elliptical family remains attached to the family with a single pinch off, and this family extends all the way to the pure vortex sheet solutions. More elongated families below this one also split at bifurcation points, and these families do not exist in the vortex sheet regime.

In the presence of surface tension, vortex patch shapes are deformed where the background straining flow is into the vortices. This leads to oscillations on the boundary, similar to those found by Tanveer (1986) for bubbles in Hele-Shaw cells. The pinch off cusp for the patch vortex becomes desingularized in the presence of surface tension, and no longer touches. The effects of surface tension on the vortex sheet and Sadovskii vortex shapes are shown to be similar but smaller.

Chapter 1

Introduction

Vortices, regions in which fluids rotate, abound in nature. The most visual examples include hurricanes, tornadoes, and the way bath water goes down the drain. The concepts of vorticity, the rotation of fluid, and the physical vortex structures, are fundamental concepts in the study of turbulence. Experimental works such as Winant and Browand (1974) and Head and Bandyopadhyay (1981) found vortices in turbulent flow, and different methods for analyzing the data from these flows can be found in Adrian et al. (2000). Numerical simulations of vortex structures in turblence have also been performed, such as Jiménez et al. (1993).

While vortices in nature are three-dimensional, a simpler problem is to consider flows that have weak variations in one dimension. This allows the flow to be modeled as a two-dimensional problem, which makes some problems more tractable. Research into vortices has used simple mathematical models to investigate their behavior, in particular by using formulations including the point vortex. When a fluid is irrotational, inviscid, and incompressible, we can define a complex potential. In the point vortex model, the complex potential is

$$w = -\frac{\mathrm{i}\Gamma}{2\pi}\ln z, \tag{1.1}$$

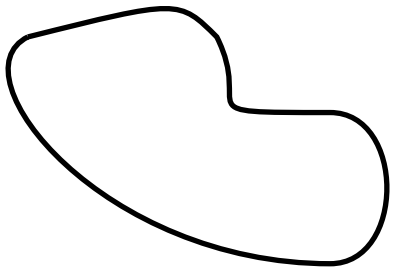

Figure 1.1: A vortex sheet model. There is a discontinuity in velocity across the vortex sheet, shown by the solid line. The vorticity is into (or out of) the page.

where w is the complex potential, Γ is the circulation of the vortex, and $z = x + \mathrm{i}y$. The complex potential is $w = \phi + \mathrm{i}\psi$, where ϕ is the velocity potential and ψ is the stream function. While the point vortex is a useful model for the behavior of the fluid outside the vortex (where the distance from the vortex is much larger than the core size), it is less useful for modeling the behavior and dynamics of the vortex core and the fluid very close to the edge of the vortex, since the point vortex is a two dimensional delta-function of vorticity. This has motivated research into desingularizations of the point vortex, in particular the vortex sheet and vortex patch, which are discussed below.

The vortex sheet is a contour where the vorticity is concentrated in a single dimension. In the two dimensional case, the vorticity of the sheet is out of (or into) the page. The vortex sheet leads to a discontinuity in the velocity of the fluid, and the strength of the sheet is related to the jump in velocity tangential to the sheet as one crosses from one side to the other. This configuration is a delta function of vorticity, but now in one dimension. If we take a vortex sheet and form it into a closed loop, we have one possible desingularization of a point vortex. An example of a contour is shown in Fig. 1.1. In this case, the vortex has a finite area, enclosed by the sheet. The flow due to the vortex goes to Eq. 1.1 as $|\mathbf{z}| \to \infty$, where $\mathbf{z}$ is the position vector from the vortex to the point of interest.

Previous work on the vortex sheet formulation has focused on the hollow vortex,

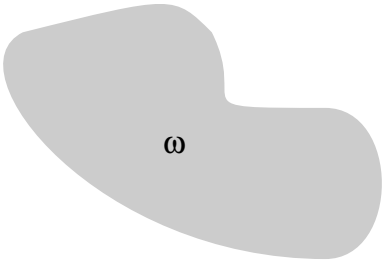

Figure 1.2: A vortex patch model. The grey area has uniform vorticity ω.

where $\rho = 0$ inside the vortex sheet. Research on hollow vortices originally focused on the dynamics of groups of these vortices, whether pairs (Pocklington (1895), Moore and Pullin (1987), Leppington (2006)), rows, or arrays (Baker et al. (1976), Ardalan et al. (1995)). Recently, Llewellyn Smith and Crowdy (2012) investigated both the shape and stability of a single steady hollow vortex in a straining field, publishing the full stability of this model of vortex for the first time. More recent work has focused on a von Kármán street of hollow vortices (Crowdy and Green (2011)) and hollow vortices in various flow configurations such as channels, behind cylinders, and in a Hele-Shaw channel (Green (2013)).

For a vortex patch, we imagine smearing the circulation of the point vortex over a finite area. This area, with non-zero vorticity, is a vortex patch. As with the vortex sheet, far from the patch, the flow looks like the flow due to a point vortex with the same circulation. Here, we focus only on patches of uniform vorticity. To reduce the dimensionality of the problem further, Zabusky et al. (1979) used contour dynamics, by calculating the entire problem based on the boundary of the vortex patches. This method was also used to calculate new vortex patch configurations called V-states. In Deem and Zabusky (1978), the contour dynamics algorithm was used to find new rotating and translating states of vortex patches, besides the known Kirchhoff vortices (Lamb (1932)). The contour dynamics method was used for both individual vortex patches and to look at the interactions between multiple vortex patches.

Moore and Saffman (1971) used elliptic coordinates to calculate steady states of a vortex patch in a straining field. This work also did a stability analysis, and pinpointed the locations where the growth mode disappeared. This work was followed by Kamm (1987), who used Schwarz functions to investigate the shape and stability of some non-elliptical configurations of vortex patches, including the vortex patch in strain. The bifurcation points of the family matched those predicted by Moore and Saffman (1971), and all the non-elliptical vortices in strain were found to be unstable. Three dimensional vortex filaments and their stability have been investigated in Robinson and Saffman (1984) and Miyazaki et al. (1995).

Studies on the stability of vortices have mainly focused on linear analysis. However, there has also been discussion about the use of energy and bifurcation diagrams to determine the stability of vortex configurations. In these bifurcation diagrams, flow properties of solution families are plotted against a control parameter. Luzzatto-Fegiz and Williamson (2012) used this method to study the stability of various configurations of vortex patches. By plotting equilibrium shapes of the vortices on a fluid impulse versus velocity diagram, they were able to find the turning points on the bifurcation diagrams. To do this, they used perturbations such as small point vortices or sources and sinks at stagnation points in flows to break symmetries, which creates distinct branches at bifurcation points. This allowed them to find all the bifurcations on the families of vortices they studied. To check these results, and to ensure they had found all the bifurcation points, they used a full linear stability analysis.

The Sadovskii vortex, the main focus of this work, is a combination of the previously discussed vortex desingularizations. It is a vortex patch surrounded by a vortex sheet, as shown in Fig. 1.3. This type of flow was previously investigated in works on bluff body wakes, including in Chernyshenko (1998). The Prandtl–Batchelor theorem shows that under typical assumptions, the vorticity inside a closed streamline tends to a

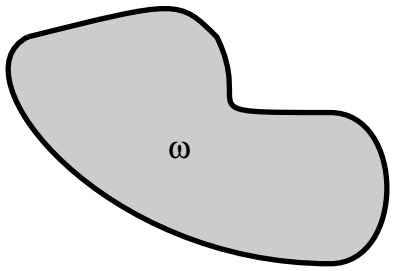

Figure 1.3: The Sadovskii vortex model. The grey area has uniform vorticity ω, while the black line is a vortex sheet.

constant value in the high Reynolds number limit (Batchelor (1956a)). Batchelor (1956b) argued that in bluff body wakes, the region of constant vorticity is bounded by a jump in tangential velocity (a vortex sheet). Further research into this approach to bluff body wakes led Sadovskii to study these kinds of flows. Sadovskii (1971) investigated a flow in which there is a jump in the Bernoulli constant on the boundary of the vortex, and the vorticity is organized into two patches of equal and opposite vorticity. Outside this region, the flow is incompressible and irrotational.

Another related work that focused on a similar flow field is Saffman and Tanveer (1984). The goal of the paper was to show that a Prandtl-Batchelor flow could be consistent with flow past a body with a forward facing flap. This leads to an area of constant vorticity inside this angled section, and irrotational flow outside a streamline going from one edge of the plate to the other. On this streamline, they also allow a vortex sheet (manifested by a jump in the Bernoulli constant). This problem was solved using conformal mappings for the inside and outside of the vortex, and then finding the correspondence between the boundary points in each mapping. Bunyakin et al. (1996), Bunyakin et al. (1998), and Chernyshenko et al. (2003) investigated flows with vortex patches trapped in airfoil cavities.

Zannetti has looked at how the stability of vortices on a flat plate can be controlled (Zannetti and Iollo (2003)). In this paper, a sink was used to create suction and keep the

plate from shedding a vortex. He has also studied flows past various shapes and bluff bodies using point vortex models in Zannetti (2006), and vortex patches in Gallizio et al. (2010). Elcrat et al. (2001) studied vortex flows around spherical bluff bodies. There has also been some research into hollow vortices in wakes past Chaplygin cusps (Zannetti and Lasagna (2013)), which are solid bodies located at stagnation points in flow, where the boundary of the body is a streamline.

Boundary conditions

We use two boundary conditions for the solution of the vortex problems in this work. One is the kinematic condition, which requires fluid on the boundary of the vortex to remain on the boundary of the vortex. Since we are solving an invisicid problem with constant densities inside and outside the vortex, and the flow is incompressible, we can describe the flow by a stream function ψ, with:

$$u = \frac{\partial \psi}{\partial y} \quad \text{and} \quad v = -\frac{\partial \psi}{\partial x}. \tag{1.2}$$

The stream function, and its relationship to the velocities, holds whether the flow is rotational or irrotational.

In this dissertation, we focus on steady flows in strain. Paths along which the stream function ψ is constant are streamlines, which in this case are also streaklines. From the definition of the stream function, the velocity at any point is tangential to the streamline and has a speed of $|\mathrm{d}\psi/\mathrm{d}n|$, where n is in the direction normal to the streamline. The kinematic condition, requiring that fluid on the vortex boundary must remain on the boundary, can be rewritten as

$$\psi|_{\partial S} = \text{constant}, \tag{1.3}$$

where ∂S is the vortex boundary. Since the velocity is tangential to streamlines in this problem, this condition can also be written in terms of the velocity as

$$\mathbf{u} \cdot \hat{\mathbf{n}} = 0, \tag{1.4}$$

where $\mathbf{u} = (u, v)$ is the velocity, and $\hat{\mathbf{n}}$ is the normal vector to the vortex boundary.

The second condition is the dynamic condition, which we also call the pressure condition or Bernoulli condition. The following derivation is similar to that in Saffman (1992). The dynamic condition comes from the incompressible Euler equations, which are

$$\nabla \cdot \mathbf{u} = 0, \tag{1.5}$$

$$\frac{\partial \mathbf{u}}{\partial t} + (\mathbf{u} \cdot \nabla)\mathbf{u} = -\frac{1}{\rho}\nabla p + \mathbf{F}, \tag{1.6}$$

where ρ is the density, p is the pressure, and $\mathbf{F}$ are any conservative body forces. Since we focus on steady problems, there is no time dependence. There are also no body forces, so $\mathbf{F} = 0$. Using vector identities, the momentum equation can be rewritten as

$$\nabla\left(\frac{|\mathbf{u}|^2}{2}\right) - \mathbf{u} \times \boldsymbol{\omega} = -\frac{1}{\rho}\nabla p, \tag{1.7}$$

where $\boldsymbol{\omega} = \nabla \times \mathbf{u}$ is the vorticity, and the time dependence and body forces have been eliminated. Since this work is in two dimensions, $\boldsymbol{\omega} = \omega\hat{z}$. The cross product term can be rewritten in terms of the stream function as

$$\mathbf{u} \times \boldsymbol{\omega} = (-v\omega, u\omega) = \omega\nabla\psi. \tag{1.8}$$

If a region has constant vorticity, the gradient can be moved outside, leading to

$$\nabla\left(\frac{|\mathbf{u}|^2}{2}-\omega\psi+\frac{p}{\rho}\right)=0. \tag{1.9}$$

This can be written as the Bernoulli condition for steady, inviscid, incompressible flows in regions with constant vorticity and no body forces:

$$\frac{\rho}{2}|\mathbf{u}|^2-\rho\omega\psi+p=\text{constant}. \tag{1.10}$$

In irrotational regions (in this work, everywhere outside the vortex), $\omega=0$ and this condition is the common

$$\frac{\rho}{2}|\mathbf{u}|^2+p=\text{constant}. \tag{1.11}$$

On the boundary of the vortex, the pressure must be equal inside and outside. Since there is an arbitrary additive constant in the definition of the stream function, we can choose $\psi=0$ on the boundary of the vortex. This leads to the dynamic condition

$$\frac{\rho_{out}}{2}|\mathbf{u}_{out}|^2-\frac{\rho_{in}}{2}|\mathbf{u}_{in}|^2=Q, \tag{1.12}$$

where Q is the difference in Bernoulli constant between the inside and outside of the vortex. In cases where $\rho_{in}=\rho_{out}$, if $Q=0$ the velocity is continuous at the vortex boundary and there is no vortex sheet. If $Q\neq 0$, there is jump in the Bernoulli constant and velocity at the boundary, which is a vortex sheet. When $\rho_{in}\neq\rho_{out}$, it is possible to have $Q=0$ and a vortex sheet, since a vortex sheet exists wherever $|\mathbf{u}_{out}|\neq|\mathbf{u}_{in}|$.

Outline of the dissertation

This research uses numerical continuation to follow families of steady Sadovskii vortices in strain. Chapter 2 calculates the vortex patch solutions, when there is no

vortex sheet on the boundary. The previously discovered solutions are confirmed, as well as new solutions farther from the circular solution. Chapter 3 uses two methods to calculate vortex sheet solutions, and finds solutions consistent with the previously known hollow solutions. Chapter 4 uses two methods to calculate solutions to the full Sadovskii problem, and shows the link between the patch and sheet solutions, as well as the solution families that don't seem to exist for the vortex sheet. Chapter 5 calculates some steady vortices in the presence of surface tension, focusing on the patch, sheet, and some Sadovskii solutions. Chapter 6 discusses future directions for research into Sadovskii vortices.

Chapter 2

The Vortex Patch

In this chapter, we describe the steady-state problem of a vortex patch in a two dimensional straining field. We review previous research on the elliptical family and expected bifurcation points, and the previously discovered bifurcating families. We then show that our inverse velocity parameterization and numerical continuation software is able to calculate the previously known solutions, as well as more bifurcating families.

Problem description

The vortex patch in a straining field can be defined in terms of the stream function and the velocity of the flow. The basic configuration is shown in Fig. 2.1. The vortex core is a patch of uniform vorticity with

$$\nabla^2\Psi = -\omega_0, \tag{2.1}$$

where the stream function is Ψ. Outside this vortex core, the flow is irrotational, and

$$\nabla^2\Psi = 0. \tag{2.2}$$

For steady states, the boundary of the core (and the division between Poisson's equation and Laplace's equation) will be a streamline, with

$$\Psi|_{z_0} = 0, \tag{2.3}$$

where z_0 is any point on the boundary of the vortex. Also at the vortex boundary, the velocity must be equal on both sides, which is really a condition on the normal derivative of the stream function

$$\lim_{z \to z_0} \frac{\partial \Psi(z)}{\partial n} = \frac{\partial \Psi(z_0)}{\partial n}. \tag{2.4}$$

In the far field, the flow looks like a straining field with a point vortex at the origin, so

$$\Psi \sim \frac{e}{2}\left(x^2 - y^2\right) - \frac{\Gamma}{2\pi} \ln|z| \quad \text{as} \quad |z| \to \infty, \tag{2.5}$$

where e is related to the strength of the straining field.

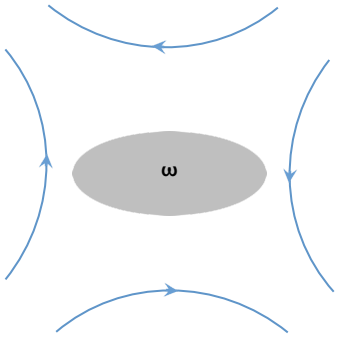

Figure 2.1: Basic configuration of the vortex patch problem. The vortex patch (with vorticity ω) is shown in grey, while the straining field flow is shown in blue.

2.1 Previous Work

Moore and Saffman (1971) found that elliptical vortex patches were steady solutions in a straining field. In order to investigate this family of solutions, they

limited themselves to elliptical vortices aligned with the x and y axes, and used elliptical coordinates to define the flow outside the vortex. Inside the vortex, the stream function is

$$\Psi_{in} = -\frac{1}{2}\Omega ab\left(\frac{x^2}{a^2}+\frac{y^2}{b^2}-1\right), \tag{2.6}$$

where a is the major axis of the ellipse, b is the minor axis, ω_0 is the vorticity, and $\Omega = \omega_0 ab/(a^2+b^2)$. Outside the vortex, the stream function is

$$\Psi_{out} = \frac{1}{4}ec^2\cosh 2\xi\cos 2\eta + Se^{-2(\xi-\xi_0)}\cos 2\eta - \frac{\Gamma}{2\pi}(\xi-\xi_0), \tag{2.7}$$

where e is related to the strength of the straining field (see Eq. 2.5), $c^2 = a^2 - b^2$, S is a constant defined by the vortex size and straining field, $\Gamma = \pi ab\omega_0$, and the coordinate system (ξ,η) is defined by

$$x = c\cosh\xi\cos\eta, \tag{2.8}$$

$$y = c\sinh\xi\sin\eta, \tag{2.9}$$

so that $\xi =$ constant are ellipses and $\eta =$ constant are hyperbolas, and the vortex boundary is defined by $\xi = \xi_0$. The boundary conditions lead to a set of equations in S that can only be satisfied for the relation

$$\frac{e}{\omega_0} = \frac{\theta(\theta-1)}{(\theta^2+1)(\theta+1)}, \tag{2.10}$$

where $\theta = a/b$. This is an equation relating the shape of the ellipse to the nondimensional parameter relating the straining field to the vorticity. A plot of the solutions to this equation is shown in Fig. 2.2. Along with computing these families of elliptical vortices in other flow fields such as shear, Moore and Saffman also carried out a stability analysis

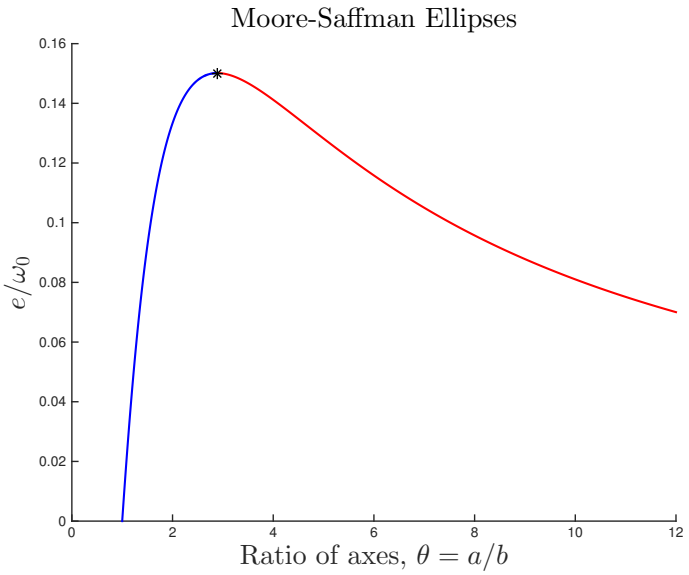

Figure 2.2: A plot of the parameter e/ω_0, the nondimensional parameter relating the strength of the straining field to the uniform vorticity in the vortex core, versus the ratio of the axes of the vortex, $\theta = a/b$. As can be seen, for values of e/ω_0 that aren't too large, there exist two solutions, with one solution (the stable one, in blue) closer to a circle, and a more elongated, unstable solution (in red). The critical value $\theta = 2.8901$, where there is only one solution, is shown by the black star.

for irrotational perturbations, and found that the growth rate of the mth mode was

$$\sigma_m = \sqrt{-\frac{\omega_0^2}{4}\left(\frac{2m\theta}{\theta^2+1}-1\right)^2 - \frac{1}{4}\left(\frac{\theta-1}{\theta+1}\right)^{2m}}, \tag{2.11}$$

where $\theta > 1$ is the ratio of the axes of the ellipse. The points where $\sigma_n = 0$ are the expected places for folds and bifurcations from the main elliptical family. Kamm (1987) used this as the basis of his continuation method, and searched for bifurcations near the points predicted by Moore and Saffman (1971). The point for $m = 2$ is the fold point in the family, where the stability changes from stable to unstable, and the ellipses become more eccentric for the same value of e/ω_0. Kamm showed the beginning of the next three bifurcating families, but was unable to calculate far along these families due to limitations of his continuation method. Families that bifurcate at even values of m are

symmetric about both the x- and y-axes, while those that bifurcate at odd values of m were found to be symmetric only across the x axis.

2.2 Procedure

While the basic problem investigated in this chapter is the same as the vortex patch problem above, the formulation is altered slightly. In this work, the far field stream function goes as

$$\Psi = \gamma\left(x^2 - y^2\right). \tag{2.12}$$

Notice that this is the same as Eq. 2.5, but with a new parameter $\gamma = e/2$. The problem was also nondimensionalized as follows:

$$x = Lx^*, \quad u = L\omega u^*, \quad \mu = \frac{\gamma}{\omega}. \tag{2.13}$$

Although this problem is described in terms of the stream function, the actual computation is done using only the shape of the vortex boundary. Given boundary points (x,y) and the nondimensional parameter μ from Eq. 2.13, one can calculate the normal vector for the vortex boundary, the velocity at any point in the flow, and the area and centroid of the vortex.

Given some parameterization of the vortex boundary $\tilde{s}$, the boundary of the vortex is $(x(\tilde{s}), y(\tilde{s}))$. In this work, although the definition of $\tilde{s}$ may change, we consistently use points that are equispaced in $\tilde{s}$. To calculate the normal vector along the vortex boundary, we use Fourier transforms to obtain the derivatives $\mathrm{d}x/\mathrm{d}\tilde{s}$ and $\mathrm{d}y/\mathrm{d}\tilde{s}$. The total perimeter of the vortex is calculated through integration of $\mathrm{d}x/\mathrm{d}\tilde{s}$ and $\mathrm{d}y/\mathrm{d}\tilde{s}$ along the vortex boundary.

Once the normal vector has been computed at each point along the vortex bound-

ary, we calculate the velocity at each point. The complex velocity due to the vortex sheet can be calculated using a boundary integral, as shown in Luzzatto-Fegiz and Williamson (2011):

$$\mathbf{u}_{\text{patch}}(\mathbf{x}) = \frac{\omega}{2\pi} \oint \frac{\mathbf{x}-\mathbf{X}}{|\mathbf{x}-\mathbf{X}|^2}(\mathbf{x}-\mathbf{X}) \cdot \frac{\mathrm{d}\mathbf{X}}{\mathrm{d}\tilde{s}} \mathrm{d}\tilde{s}, \tag{2.14}$$

where $\mathbf{u}_{\text{patch}}$ is the velocity due to the patch, and the total velocity is

$$\mathbf{u}(\mathbf{x}) = \mathbf{u}_{\text{patch}}(\mathbf{x}) + \mathbf{u}_{\text{strain}}, \tag{2.15}$$

where the velocity due to the straining field is $\mathbf{u}_{\text{strain}} = (-2\mu y, -2\mu x)$.

The main condition we enforce for this problem is that the boundary of the vortex is a streamline (Eq. 2.3). This is equivalent to requiring there be no velocity normal to the vortex boundary along the boundary, which can be enforced by

$$\mathbf{u} \cdot \hat{\mathbf{n}} = 0. \tag{2.16}$$

If we define $\mathbf{n} = (\mathrm{d}y/\mathrm{d}\tilde{s}, -\mathrm{d}x/\mathrm{d}\tilde{s})$, we can write $\hat{\mathbf{n}} = \mathbf{n}/|\mathbf{n}|$. Since $\mathbf{u} \cdot \mathbf{n} = 0 = \mathbf{u} \cdot \hat{\mathbf{n}}$, we can apply previously calculated quantities to the unnormalized version of this equation.

As in Luzzatto-Fegiz and Williamson (2011), we add our size and position parameters to this equation. For the vortex patch in a straining field, there is a preferred alignment of any non-circular vortex in the field, so it is unnecessary to worry about possible rotations of the solutions. However, it is important to constrain the size and position of the vortex. Setting the area of the vortex to be π defines the length scale in the problem, which is important to allow convergence to a single solution. Since we are interested in the vortex in strain, we require that the centroid of the vortex be located at

the origin. The area is calculated through the boundary integral

$$A = \oint x \frac{\mathrm{d}y}{\mathrm{d}\tilde{s}} \mathrm{d}\tilde{s}. \tag{2.17}$$

The centroids are calculated from

$$x_C = -\frac{1}{2A} \oint x^2 \frac{\mathrm{d}y}{\mathrm{d}\tilde{s}} \mathrm{d}\tilde{s} \quad \text{and} \quad y_C = \frac{1}{2A} \oint y^2 \frac{\mathrm{d}x}{\mathrm{d}\tilde{s}} \mathrm{d}\tilde{s}. \tag{2.18}$$

The full equation, including the constraints, is

$$\mathbf{u} \cdot \mathbf{n} + a\hat{s} x_c + b\hat{s}^2 y_c + c\hat{s}^3 (A - \pi) = 0, \tag{2.19}$$

where a, b, and c are weights for the functions, and $\hat{s}$ is the normalized $\tilde{s}$, so that $0 \leq \hat{s} \leq 1$. This equation forms the basis for all of the continuation methods.

Equispaced by Inverse Velocity

A choice of parameterization for the calculated points on the vortex boundary is necessary. In their work on Kirchhoff vortices, Luzzatto-Fegiz and Williamson (2011) noted that the cusps and other sharp features occur where the speed is lowest. They used an inverse velocity discretization to cluster points around places with low speed and sharp features, and spread the points out in areas with high speeds and smooth features. The inverse velocity discretization is

$$\tilde{s}(s) = A \int_0^s \frac{\mathrm{d}s'}{|\mathbf{u}(s')|}, \tag{2.20}$$

where A is chosen so $0 \leq \tilde{s} \leq 2\pi$, s is the arclength, and $\mathbf{u}$ is the velocity in the reference frame of interest. Points that are equispaced in $\tilde{s}$ will be closer together in areas of low

speed, and farther apart where the speed is higher. Figure 2.3 shows an example of this point clustering. The left panel shows 64 points that are equispaced by arclength. The right panel shows 64 points equispaced by inverse velocity. The clustering near the cusp is apparent. These are demonstrated on the shape shown in Fig. 2.7(b).

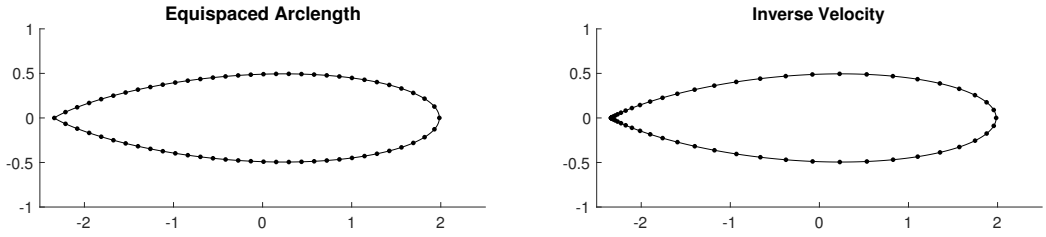

Figure 2.3: A comparison of arclength and inverse velocity parameterizations using 64 points. On the left are the points equispaced by arclength, while the right panel shows the points equispaced in inverse velocity. The inverse velocity method clusters the points where the speed is low, in this case at the cusp of the shape. The line is a plot of the data, which is 512 points and is the same as that in Fig. 2.7(b).

2.2.1 Our Procedure

Our procedure uses a similar method to that in Luzzatto-Fegiz and Williamson (2011) to utilize the inverse velocity parameterization. Given a solution, we use cubic splines to adjust the points so they are equispaced in inverse velocity. Then the normal vectors of these points are frozen in space, and we calculate the adjustment to each point along its normal vector to satisfy Eq. 2.19. That is to say,

$$x_i^n = x_i + \alpha(\tilde{s}_i) n_x, \tag{2.21}$$

$$y_i^n = y_i + \alpha(\tilde{s}_i) n_y, \tag{2.22}$$

where (x_i^n, y_i^n) are the locations of the new points, (x_i, y_i) are the locations of the previous (equispaced in inverse velocity) points, $\alpha(\tilde{s})$ is the scalar correction along the normal

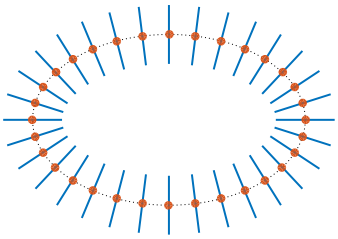

Figure 2.4: Overview of the numerical scheme. Given a shape (dotted black line), we calculate the points that are equispaced in $\tilde{s}$, shown by the red dots. We then compute the normal vectors to each point and lock these in place (blue lines). We then change the parameter and compute a scalar function $\alpha(\tilde{s})$ that describes the adjustments to each point along the normal vectors.

vectors, and $\mathbf{n} = (n_x, n_y)$. The numerical scheme calculates the Fourier modes of $\alpha(\tilde{s})$, and the correction function α at each point on the vortex boundary is obtained through an IFFT. Since α is a real-valued scalar function, we perform our Newton iteration on the error function $\mathbf{F}$, where

$$\mathbf{F}_1 = \begin{bmatrix} \mathrm{Re}\left(\hat{\mathbf{F}}\right) \\ \mathrm{Im}\left(\hat{\mathbf{F}}\right) \end{bmatrix}, \tag{2.23}$$

$$\mathbf{F} = \mathbf{u}\cdot\mathbf{n} + a\hat{s}x_c + b\hat{s}^2 y_c + c\hat{s}^3(A-\pi), \tag{2.24}$$

and $\hat{\mathbf{F}}$ is the FFT of $\mathbf{F}$.

As discussed in Appendix A, our continuation method involved doing pseudo-arclength continuation of this equation. At bifurcation points, we used a simple perturbation to calculate perturbed points on the bifurcating branches. Using these perturbed points as initial guesses, we then performed continuation of the actual problem. These results are discussed below.

2.3 Results

We performed numerical continuation on the vortex patch with both 128 and 512 points. Using 128 points has the advantage of increased speed, but there is difficulty converging to solutions with sharp features. Increasing the number of points slowed computation time, but allowed better convergence and solutions farther along solution branches. In the following sections, we discuss the results from this continuation. We begin with an overview of the elliptical solutions, then use a perturbation method to switch branches and plot the overall families of solutions for the patch vortex. We then discuss in more detail the first four bifurcating families.

2.3.1 Moore-Saffman Elliptical Solutions

In Fig. 2.5, we show the calculated Moore-Saffman elliptical patch vortex solutions, up to the last converged shape. The analytically known solutions follow this curve all the way to the origin. The blue line is the calculated solutions from our continuation code. We started with a nearly circular ellipse, at the top of the plot, and then used the pseudo-arclength continuation to follow the family as the vortices became more elongated. The black circles are the locations where the growth modes of perturbations go to zero in Moore and Saffman (1971), and discussed above in Eq. 2.11. The red dots are the bounding points where the continuation code detected bifurcation and fold points. Since the code only detects that a fold or bifurcation occurred between two points, we have plotted both the points that bookend the segment where the special point occurs. The pairs are very close together, and generally appear to both fall within the marker for the theoretical points.

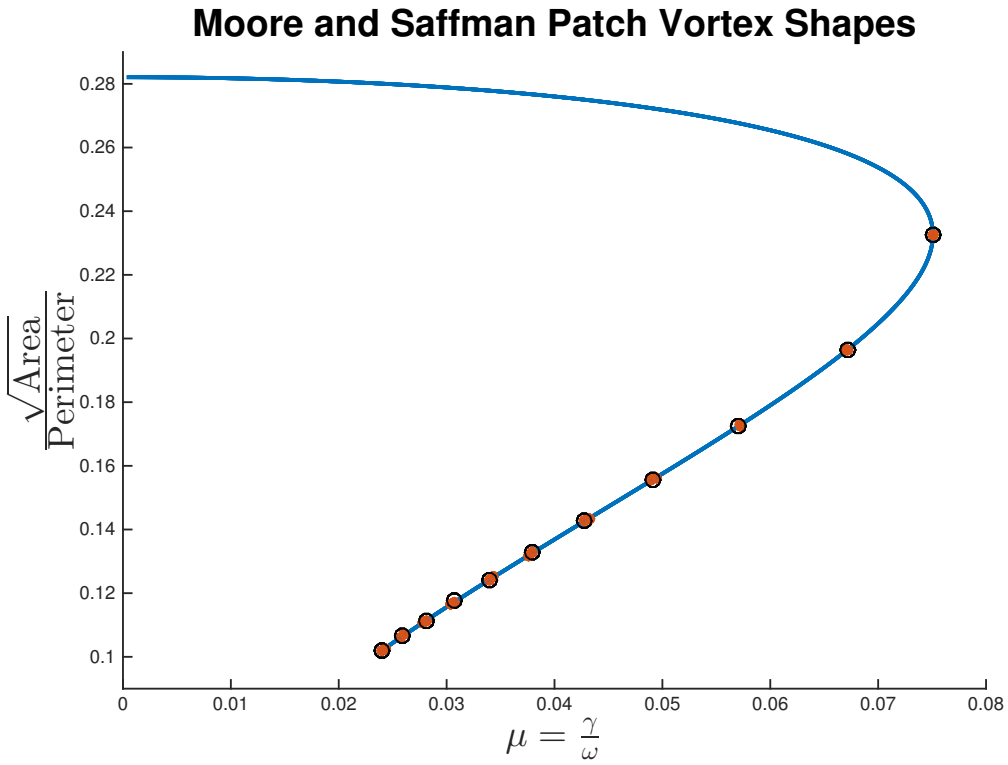

Figure 2.5: A plot of the parameter μ, the nondimensional parameter relating the strength of the straining field to the uniform vorticity in the vortex core, versus the nondimensional shape parameter. The blue line is the calculated ellipses, the black circles are the expected fold and bifurcation points from the theory, and the red dots are the bounding points of the calculated fold and bifurcation points (the bifurcation or fold point falls between each pair of red dots). The red dots are so close together they cannot be distinguished.

2.3.2 Bifurcating Families

Continuation of the elliptical solutions confirmed the expected locations of the bifurcation and fold points. To switch branches onto the bifurcating families, we used the perturbation method discussed in Appendix A. These perturbed solutions were then used as the starting solutions for continuation of the unperturbed problem along the bifurcating families.

In Fig. 2.6, we plot these non-elliptical branches. The elliptical solutions are in blue, and the bifurcation and fold points predicted by theory are the black stars. The

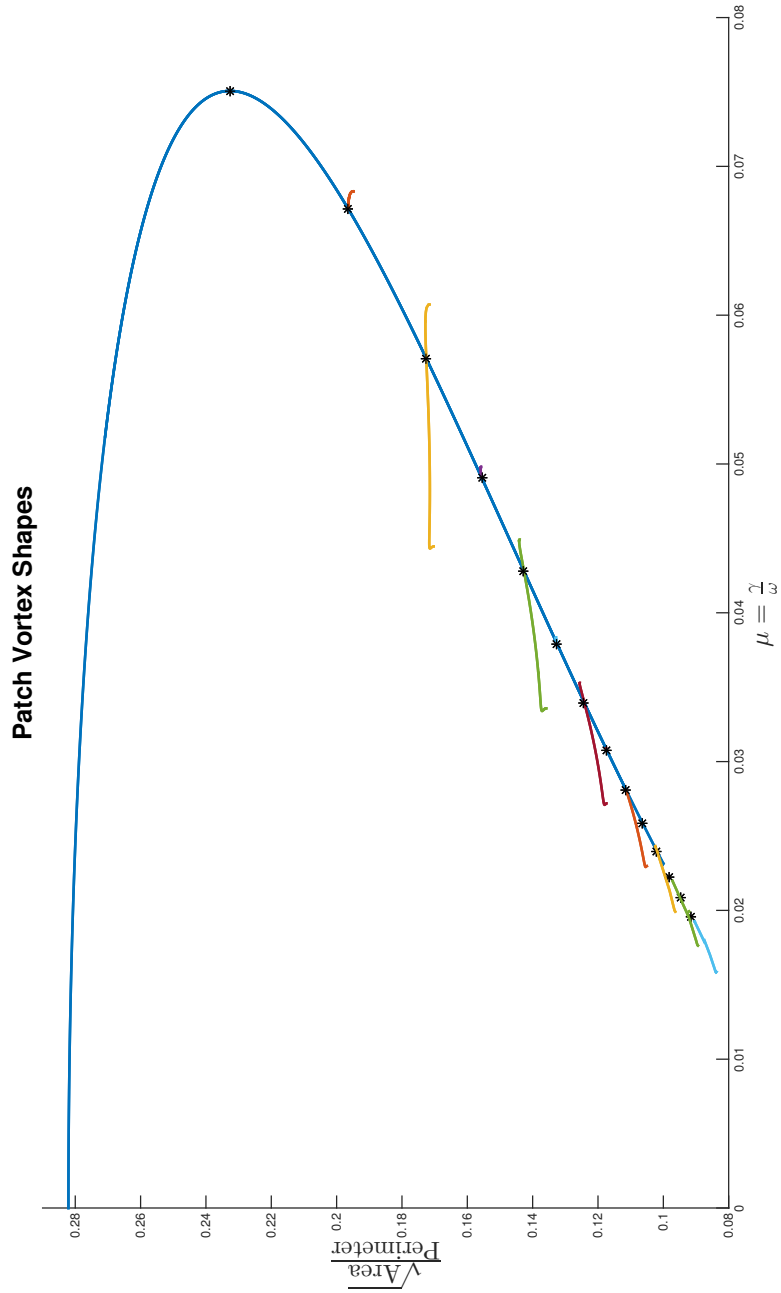

Figure 2.6: Bifurcating families from the elliptical solutions: a plot of the parameter μ, the nondimensional parameter related the strength of the straining field to the uniform vorticity in the vortex core, versus the nondimensional shape parameter. The blue line corresponds to the calculated ellipses, while the black stars show the theoretical bifurcations and fold points. The colored branches are calculated using a perturbation method to switch branches at bifurcation points.

colored branches show those we calculated by switching branches using the perturbation method. As can be seen, we were able to calculate at least part of the bifurcated families at eleven different bifurcation points. As the bifurcations occur on more elongated ellipses, we expect to need more points and modes to accurately calculate the shapes. It also becomes more difficult to perturb the solutions, because the more elongated shapes of both the elliptical family and the bifurcating branches are very similar. Figure 2.6 shows the solutions we were able to obtain with 512 points and 128 modes. Solution families end when convergence failed, or solutions were nonphysical (when the vortex boundary crossed itself, or high frequency oscillations at the Nyquist mode became apparent).

Bifurcation at $m = 3$

The first bifurcation point occurs at $m = 3$ in Eq. 2.11. As Kamm (1987) calculated, this family is not symmetric about the y-axis, and has a teardrop shape. Figure 2.7 shows an overview of this family, including an intermediate shape and the limiting shape. The spacing of the calculated solutions changes based on our objectives; in the middle of the family, the continuation code ran easily and the shapes progress clearly from the ellipse to the teardrop. Near the limiting shape, a smaller step size was used in the continuation code to get as accurate a shape as possible with 512 points and 128 complex modes. Since the code uses splines to rediscretize the points in inverse velocity, there is always a slightly rounded cusp on small enough scales. However, when viewing the whole shape it seems there is a sharp angle at the cusp. Previously, the shapes at the cusps of vortex patches have been studied by Saffman and Tanveer (1982) and Overman (1986).

The asymmetry in this shape necessitates some discussion of the symmetries of the background straining field. In Fig. 2.7, we have shown shapes that have the cusp on the left and the rounded side on the right. The numerical continuation also calculated

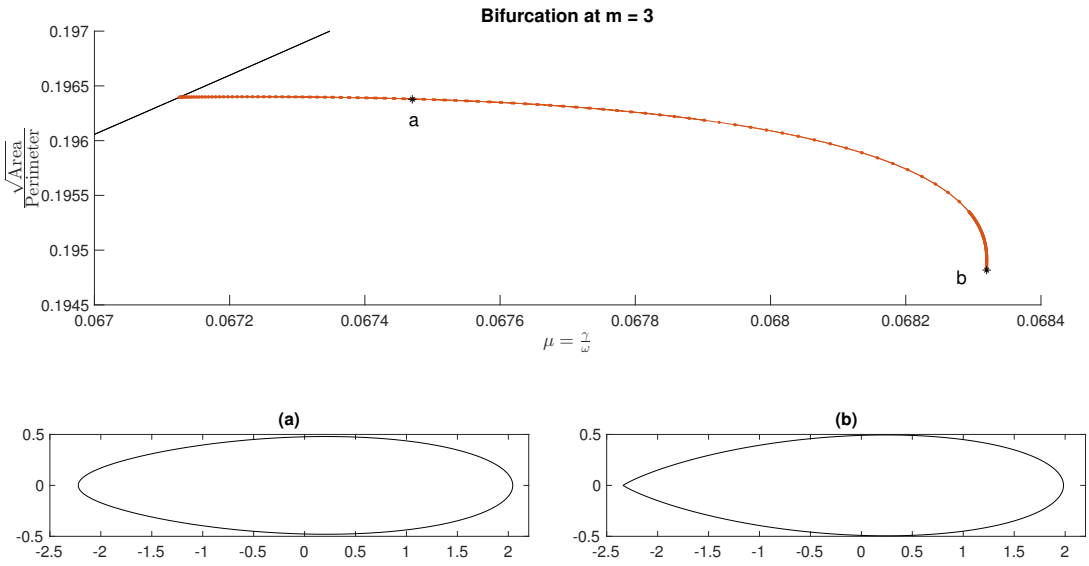

Figure 2.7: Detail of the bifurcation at $m = 3$. The black line shows the elliptical solutions, while the red dots show calculated shapes on the bifurcating branch. The left ($\mu = 0.06747$) and right ($\mu = 0.06832$) stars indicate the shapes plotted in (a) and (b), respectively. This family occurs only on the outside of the elliptical solutions, where μ is larger and the vorticity inside is weaker with respect to the straining field strength.

shapes that had the cusp on the right and the rounded side on the left. When plotted on top of each other, choosing to reflect one of these shapes across the y-axis, these shapes were identical, because they are actually the same solutions. For a 2D straining field, a rotation of the entire field by π results in the same flow. Therefore there is no preferred direction for these shapes, and given a flow with an asymmetric vortex in it, one cannot tell whether the vortex is pointing left or right with respect to the flow. In the rest of the paper, we have chosen to show the asymmetric shapes facing a single direction, but it should be understood that a vortex facing the other direction is allowed and is in fact the same flow.

Bifurcation at $m = 4$

The next bifurcation point occurs at $m = 4$ in Eq. 2.11. This family has two different solutions, depending on whether μ is increasing or decreasing. When μ is increasing (which can be thought of as a decrease in the strength of the vortex patch, or an increase in the strength of the straining field), this family moves from an ellipse to a doubly symmetric football shape with two cusps (Fig. 2.8(a) and (c)). When μ is decreasing, this family pinches off in the center, but remains doubly symmetric (Fig. 2.8(b) and (d)). Kamm (1987) was able to calculate the cusped shape for larger values of μ, but he was unable to calculate the vortex shapes with the pinch off.

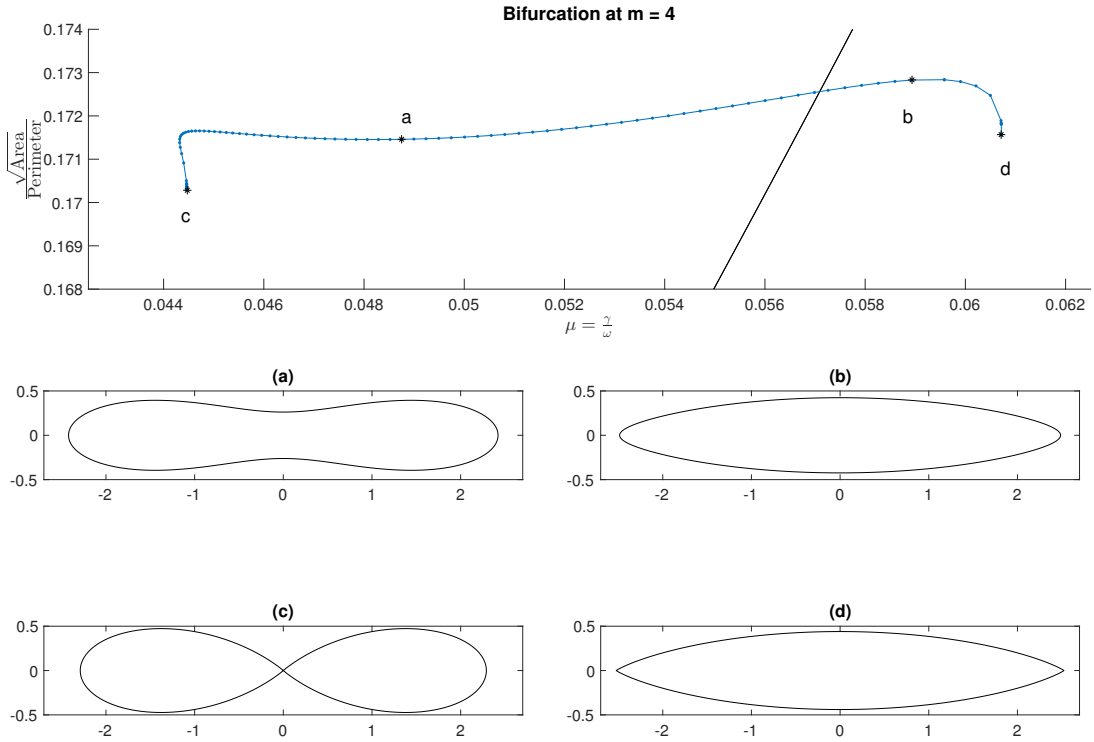

Figure 2.8: Detail of the bifurcation for $m = 4$. The black line is the calculated ellipses, and the blue dots are calculated solutions of the bifurcating family. The black stars show the limiting solutions which are plotted in a ($\mu = 0.04875$), b ($\mu = 0.05893$), c($\mu = 0.04446$), and d ($\mu = 0.06072$).

Bifurcation at $m = 5$

Continuing along the elliptical branch, the next bifurcation occurs at $m = 5$. As with the previous odd m value, this branch only occurs on the side of the elliptical family with larger values of μ, and again has symmetry about the x-axis but not the y-axis. As before, one side of the vortex is rounded, and the other side becomes cusped. However, as this shape is more elongated, the maximum width occurs closer to the cusp than the rounded side. This branch, shown in Fig. 2.9, was the last calculated by Kamm (1987). The vortex shapes in this family share some features with those from the bifurcating

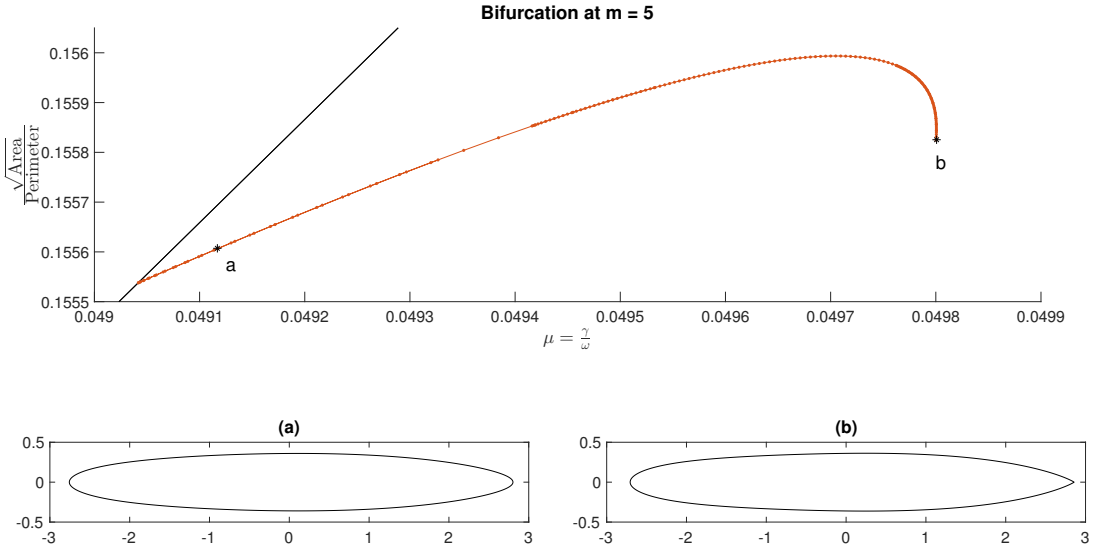

Figure 2.9: Detail of the bifurcation for $m = 5$. The black line is the calculated ellipses, and the red dots are calculated solutions of the bifurcating family. The left ($\mu = 0.04912$) and right ($\mu = 0.04980$) black stars show the solutions which are plotted in (a) and (b), respectively.

family at $m = 3$. Bifurcating families at odd values of m are asymmetric about the y-axis, and as they branch off from more elongated ellipses, they too become more elongated in the center.

Bifurcation at $m = 6$

The next even bifurcation occurs at $m = 6$, and it begins to show the pattern for the even bifurcating families. Again, the smaller μ family has pinch offs, but this time there are two, whereas for $m = 4$ there was only one. For larger μ, the family again has two cusps, but is more elongated in the middle. These shapes and the family are shown in Fig. 2.10. The bifurcating family also has a steeper slope, as the angle between the bifurcating family and the elliptical family becomes smaller as m increases.

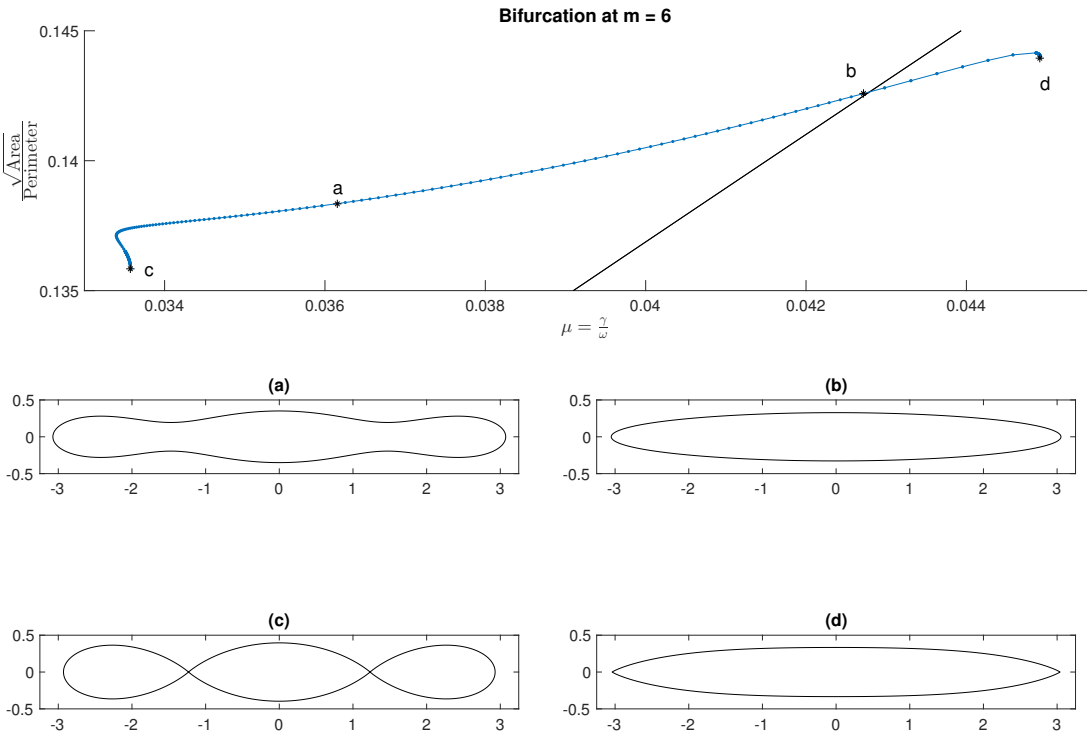

Figure 2.10: Detail of the bifurcation for $m = 6$. The black line is the calculated ellipses, and the blue dots are calculated solutions of the bifurcating family. The black stars show the solutions that are plotted in a($\mu = 0.03615$), b ($\mu = 0.04271$), c ($\mu = 0.03358$), and d ($\mu = 0.04492$).

Later bifurcating families

The pattern of an increase in the number of pinch offs and elongation of the cusped shapes continues as m increases. While we didn't focus on the solutions for branches with higher values of m, Fig. 2.11 shows the last shape for the branch with seven pinch offs, which occurs at $m = 16$. For the even values of m, the bifurcating family with smaller μ will have $m/2 - 1$ pinch offs.

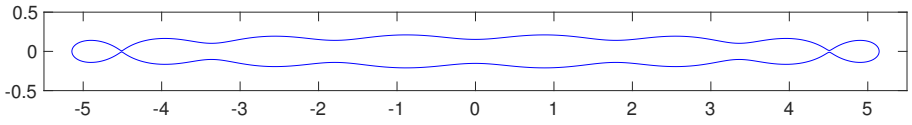

Figure 2.11: Vortex shape for the bifurcating family with smaller μ at $m = 16$, showing 7 developing pinch offs.

2.3.3 Solutions for $\mu < 0$

We previously discussed that the 2D straining field is symmetric and remains unchanged by rotations of π. There is one other geometric property of the flow that is of interest to our work. Since our straining field is defined as

$$(u, v) = (-2\mu y, -2\mu x), \tag{2.25}$$

reflection of the straining field across the line $y = x$ also leaves the straining field unchanged. If a vortex solution for $\mu > 0$ is reflected across the line $y = x$, the straining field remains the same but the vortex now has the opposite sign of vorticity ($\mu < 0$). These solutions were also found by our numerical continuation by decreasing μ as we continued through the circular solution at $\mu = 0$ and into the negative values of μ. Given some solution for $\mu_1 > 0$, one can simply rotate the vortex by $\pi/2$, leaving the straining field

unchanged, and that will be a solution for $-\mu_1$. In the straining field used in this chapter, this leads to the long axis of the vortices aligned with the y-axis instead of the x-axis.

2.4 Summary

In this chapter, we used an inverse velocity parameterization to solve for the shape and velocity of patch vortices in a 2D straining field. Bifurcating families from the elliptical solutions were found at the expected locations, and these bifurcating families alternate between shapes with one axis of symmetry and shapes with two axes of symmetry. Our calculated shapes for the first few bifurcating branches seem to be the same as those previously found by Kamm (1987), with these branches ending in pinch offs or cusps.

Chapter 2 is currently being prepared for submission for publication. Freilich, Daniel; Llewellyn Smith, Stefan. "The Sadovskii Vortex in Strain". The dissertation author was the primary investigator and author of this material.

Chapter 3

The Vortex Sheet

In this chapter, we formulate the problem for steady shapes of vortex sheets in a straining field. To compare solutions with previous work, we begin by solving for the hollow vortex solutions, where $\rho_{in} = 0$. We use two independent methods to calculate the shapes, one similar to a boundary element type method (with no assumptions about the form of the flow), the other similar to the inverse velocity method used in the vortex patch case (which computes the flow as a superposition of the vortex sheet and straining field). Our solutions agree with those found in Llewellyn Smith and Crowdy (2012). We discuss a possible bifurcation point, and the effect of density on the problem.

Problem Description

Vortex sheets occur at discontinuities in velocity in a flow. The standard example is a two layer flow, where the top layer has constant velocity v_1 and the bottom layer has a constant velocity v_2. When $v_1 \neq v_2$, there is a discontinuity in velocity at the boundary between the two layers, which is a vortex sheet (see Fig. 3.1). While the vortex patch has no singularities in the vorticity, a vortex sheet still has a singularity in the vorticity, but in this case it is spread over some contour. A point vortex in 2D is a two dimensional Dirac

delta function, a vortex sheet is a one dimensional Dirac delta function, and a vortex patch is nonsingular.

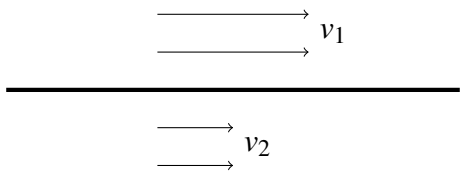

Figure 3.1: The bold line shows the location of the vortex sheet. The fluid above the sheet is moving at v_1, and the fluid below the sheet is moving at v_2. The discontinuity in velocity leads to a concentration of vorticity at the interface.

The relationship between the point vortex and vortex sheet is also evident in the equation for the velocity due to a vortex sheet. As Saffman (1992) shows, a vortex sheet induces the following velocity (for points not on the vortex sheet):

$$u - \mathrm{i}v = \frac{-\mathrm{i}}{2\pi} \int \frac{\kappa(s',t)\mathrm{d}s'}{z - Z(s',t)}, \tag{3.1}$$

where $(u(x,y), v(x,y))$ is the induced velocity, $z = x + \mathrm{i}y$ is the point of interest and κ and Z are parameterized by arclength and time. If the velocities on each side of the vortex sheet are known, κ is the difference in speed across the vortex sheet (by definition, the jump in velocity must be tangential to the vortex sheet). This integral is the same as the flow field due to a set of point vortices along the contour, with the correct circulation. For points on the vortex sheet, that integral becomes a principal value integral, and the induced velocity gives the velocity of the vortex sheet. To get the velocity just on either side of the sheet, half the velocity jump is added or subtracted to the principal value:

$$u - \mathrm{i}v = \frac{-\mathrm{i}}{2\pi} \fint \frac{\kappa(s',t)\mathrm{d}s'}{z - Z(s',t)} \pm \frac{\kappa}{2} \left(x' - \mathrm{i}y'\right), \tag{3.2}$$

where x' and y' are the components of the unit tangent vector of the boundary.

3.1 The Hollow Vortex

Previous research has focused on the hollow vortex, which is a vortex sheet surrounding a constant pressure region (this is equivalent to setting $\rho = 0$ inside the vortex). The hollow vortex in a straining field was solved by Llewellyn Smith and Crowdy (2012) using a conformal mapping. In this problem, the fluid outside the vortex is irrotational, so we are solving Laplace's Equation for the stream function

$$\nabla^2 \Psi = 0. \tag{3.3}$$

For points far away from the vortex, the velocity field is the same as that from a point vortex in a straining field, so the complex potential is

$$w(z) \to \gamma z^n - \frac{\mathrm{i}\Gamma}{2\pi} \log z + \text{analytic function} \tag{3.4}$$

as $|z| \to \infty$.

If the vortex sheet strength is known, the velocity field can be calculated from Eq. 3.1. When the sheet strength isn't known, a different boundary condition is required. One option, used in Llewellyn Smith and Crowdy (2012), is a Bernoulli-type kinematic boundary condition, where a constant induced velocity is specified on the boundary. This condition can be written as

$$\left| \frac{\mathrm{d}w}{\mathrm{d}z} \right| = \text{constant} \tag{3.5}$$

on the vortex boundary. Finally, the vortex sheet, which is the vortex boundary, must also be a streamline, so

$$\Psi = \text{constant} \tag{3.6}$$

on the vortex boundary.

Using a conformal map from the unit disc to the fluid outside the vortex, Llewellyn Smith and Crowdy (2012) found a closed form for the shape of the vortex

$$z(\zeta) = a\left[\frac{1}{\zeta} - 2i\beta\zeta + \frac{\beta^2}{3}\zeta^3\right] \tag{3.7}$$

for a second order straining field. The boundary of the vortex is defined as $|\zeta| = 1$, and

$$\beta = -\frac{\mu_h}{1+\sqrt{1-\mu_h^2}}, \quad \mu_h = \frac{8\pi\gamma a^2}{\Gamma}, \tag{3.8}$$

where γ is the strength of the straining field, Γ is the circulation of the vortex sheet, and a is a length scale. From the conformal mapping, it is clear that as we go around the unit circle in a counterclockwise direction, we traverse the vortex boundary in a clockwise direction.

3.2 Procedure

We solved the vortex sheet problem using two different iterative methods. In the first method, a boundary element type method, both the shape of the vortex and the velocities on the inside and outside of the vortex boundary were treated as unknowns. In this method, nothing is assumed about the form of the solution, except that the flow outside of the vortex sheet must be irrotational, and therefore the velocity must be analytic outside. In the second method, we use knowledge of the physical problem to calculate the velocity based on a superposition of the velocity fields due to the straining field and the vortex sheet. In this method, the boundary points are discretized by inverse velocity.

3.2.1 Boundary element type method

In the boundary element type method, we use boundary points that are equispaced by arclength. Since the velocity on the outside of the vortex sheet is constant (Eq. 3.5), this is the same discretization as inverse velocity would give (if the inverse velocity were calculated using the outside velocity). The boundary conditions of this problem are that there is no normal flow on the boundary of the vortex

$$\mathbf{u} \cdot \hat{\mathbf{n}} = 0, \tag{3.9}$$

and that the jump in the Bernoulli constant across the vortex sheet is constant:

$$|\mathbf{u}_{out}|^2 - \rho|\mathbf{u}_{in}|^2 = q^2, \tag{3.10}$$

where ρ is the density ratio ρ_{in}/ρ_{out} and $q^2 = Q/\rho_{out}$ is related to the jump in the Bernoulli constant. In the case of the hollow vortex, $\rho = 0$ and $|\mathbf{u}_{out}| = q$. In order to nondimensionalize this problem, we use the following nondimensional parameters:

$$x = Lx^*, \quad u = L\gamma u^*, \quad \lambda_s = \frac{\gamma L}{q}, \quad \rho = \frac{\rho_{in}}{\rho_{out}}, \tag{3.11}$$

where L is a length scale, γ is the strength of the straining field, ρ_{in} and ρ_{out} are the inside and outside densities of the fluids, and q is the speed on the outside of the vortex sheet, which is a measure of the strength of the vortex sheet. In this nondimensionalization, λ_S plays a similar role to μ_h, in that both parameters relate the strength of the straining field to the vortex sheet strength. However, the relationship between the jump in Bernoulli constant and the total circulation of the vortex sheet is nontrivial. Llewellyn Smith and Crowdy (2012) specified the total circulation at infinity, which made the choice of μ_h straightforward. The length scale of the problem was adjusted afterwards to set the vortex

area. In our boundary element method, we set the vortex area, and the circulation outside the vortex can only be calculated after a solution has been found. The circulation outside the vortex is

$$\Gamma = \oint \mathbf{u} \cdot \mathrm{d}\mathbf{s}, \tag{3.12}$$

which can be simplified to Pq in the hollow case, where q is the velocity on the boundary of the vortex and P is the perimeter length of the vortex. If Γ is replaced by Pq in Eq. 3.8,

$$\lambda_s = \frac{\mu_h PL}{8\pi a^2}. \tag{3.13}$$

Notice that P and L have dimensions of length, as does a.

The boundary element type method calculates the shape of the boundary (x,y), and the velocity of the fluid at these points, $\mathbf{u} = (u,v)$. This is a total of $4N$ variables, so $4N$ conditions are required to fully determine the problem. One condition is straightforward: we require boundary points to be equispaced by arclength, so that

$$\left(\frac{\mathrm{d}x}{\mathrm{d}s}\right)^2 + \left(\frac{\mathrm{d}y}{\mathrm{d}s}\right)^2 = 1. \tag{3.14}$$

Since this applies at each point, this is N conditions. The dynamic boundary condition, also applied at each point, requires

$$(u+2x)^2 + (v-2y)^2 = \lambda^{-2}, \tag{3.15}$$

where we have separated the velocity due to the vortex sheet (u,v) from the velocity due to the straining field $(2x,-2y)$.

The kinematic boundary condition requires

$$(u+2x)\frac{\mathrm{d}y}{\mathrm{d}s} = (v-2y)\frac{\mathrm{d}x}{\mathrm{d}s}, \tag{3.16}$$

so the vortex sheet will be a streamline ($\mathbf{u}_T \cdot \hat{\mathbf{n}} = 0$, where $\mathbf{u}_T$ is the total velocity and $\hat{\mathbf{n}}$ is the unit normal vector of the vortex boundary).

This is $3N$ equations for $4N$ variables. To fully determine the system of equations, we need another set of conditions. As was done by Vanden-Broeck (1991) when studying waves, we use a Cauchy condition on the velocity, which requires the velocity to be analytic. In fact, since the Cauchy integral is complex, one could get $2N$ conditions out of it, but we choose to use v as the condition, so that

$$v(t) = \mathrm{Im}\left\{-\frac{\mathrm{i}}{\pi}\oint \frac{(u(a)+\mathrm{i}v(a))}{[x(a)+\mathrm{i}y(a)]-[x(t)+\mathrm{i}y(t)]}\left(\frac{\mathrm{d}x(a)}{\mathrm{d}s}+\mathrm{i}\frac{\mathrm{d}y(a)}{\mathrm{d}s}\right)\mathrm{d}a\right\}. \tag{3.17}$$

We tested this condition using u as well, and found the solution was unaffected. These integrals are evaluated as discrete sums over the boundary points. Evaluating these integrals on the points of interest would require dealing with singularity that would occur in the denominator, since at the point of interest $z(a) = z(t)$. To avoid this, we use the method described by Baker and Nachbin (1998). The usual FFT and IFFT are

$$X_k = \sum_{n=-\frac{N}{2}}^{\frac{N}{2}-1} x_n \mathrm{e}^{-2\pi \mathrm{i}kn/N}, \quad x_n = \frac{1}{N}\sum_{k=-\frac{N}{2}}^{\frac{N}{2}-1} X_k \mathrm{e}^{2\pi \mathrm{i}kn/N}. \tag{3.18}$$

To get the midpoints, we actually want

$$x_{n+1/2} = \frac{1}{N}\sum_{k=-\frac{N}{2}}^{\frac{N}{2}-1} X_k \mathrm{e}^{2\pi \mathrm{i}k(n+1/2)/N}, \tag{3.19}$$

which can be rewritten as

$$x_{n+1/2} = \frac{1}{N}\sum_{k=-\frac{N}{2}}^{\frac{N}{2}-1} \left(X_k \mathrm{e}^{\pi \mathrm{i}k/N}\right) \mathrm{e}^{2\pi \mathrm{i}kn/N}. \tag{3.20}$$

Operationally, we take the FFT, multiply this by the exponential, and then take the

standard IFFT. To enforce the boundary conditions at the actual boundary points, the midpoints are used for a in the integral, and t remains the actual points of interest.

Although this is enough equations, there are still have a few degrees of freedom we haven't addressed. To set the length scale, we choose an area for the vortex. We also require the vortex to be centered at the origin. As in Luzzatto-Fegiz and Williamson (2011), we add these three constraints to one of the conditions. After some experimentation, it seems the numerical scheme worked best with the extra conditions added to the dynamic condition. The area is calculated through the boundary integral

$$A = \oint x \frac{\mathrm{d}y}{\mathrm{d}s} \mathrm{d}s. \tag{3.21}$$

The centroids are calculated from

$$x_C = -\frac{1}{2A} \oint x^2 \frac{\mathrm{d}y}{\mathrm{d}s} \mathrm{d}s \quad \text{and} \quad y_C = \frac{1}{2A} \oint y^2 \frac{\mathrm{d}x}{\mathrm{d}s} \mathrm{d}s. \tag{3.22}$$

The full dynamic condition, including constraints, is

$$\lambda^2 \left[(u+2x)^2 + (v-2y)^2 \right] - 1 + a t_1 x_c + b t_2 y_c + c t_3 (A - \pi) = 0, \tag{3.23}$$

where a, b and c are weights, and t_1, t_2, t_3 are the first three Legendre polynomials Note that these Legendre polynomials are functions of the normalized arclength $\hat{s}$, with $-1 \leq \hat{s} \leq 1$. It seems that using functions that are orthogonal for the constraints results in solutions that are more likely to satisfy the constraints. We used weights of $a = b = c = 100$ for this problem.

As shown in Fig. 3.2, the boundary element type method data follows the analytical curve. With 512 points, it is unable to compute solutions near the end of the family, where the shape pinches off in the middle and becomes multiply connected. Convergence

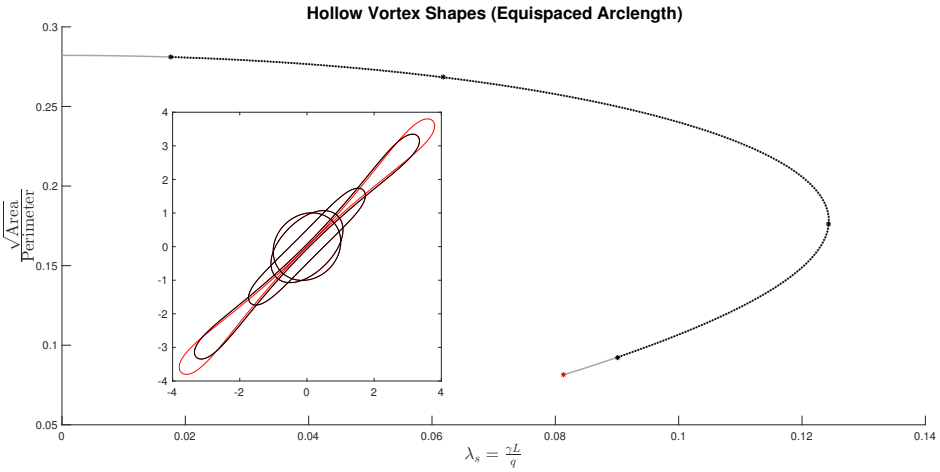

Figure 3.2: Overview of hollow vortex shapes calculated using equispaced points. In this plot, the shape parameter is plotted against λ_s, a nondimensional parameter relating the straining field strength to the vortex sheet strength. The solid grey line shows the results obtained from Llewellyn Smith and Crowdy (2012), while the dotted black line shows the data we obtained through continuation of our boundary element method using the BEM type method. The inset box shows selected hollow vortex shapes, with their location marker by the stars on the main plot. For each shape, the analytical results are plotted in red underneath the black lines showing our calculated shapes. The red shape shown is the limiting analytical shape.

near this point is difficult because the code has trouble converging as the distance between points becomes similar to the width of the narrowest parts of the vortex. Calculated shapes are shown at $\lambda_s = 0.017666, 0.061762, 0.124321, 0.090117$ as indicated by the black stars. These shapes, plotted in the inset, are shown in black. The analytical shapes are plotted in red underneath, but are not visible due to the agreement in shapes. The red star shows the pinch off point at $\lambda = 0.081375$, which is plotted in red. Due to the limitations noted near the pinch off point, we were unable to calculate that shape.

3.2.2 Calculation based on vortex sheet strength

The other method for calculating the vortex sheet shapes is similar to that used in the vortex patch solutions. Given a vortex sheet of known sheet strength, the velocity due to the sheet can be calculated from Eq. 3.2. This velocity (u, v) is then used in the same

conditions as for the boundary element method, Eq. 3.15 and Eq. 3.16. In this case, the unknowns are only the shape of the vortex sheet and the vortex sheet strength at each boundary point.

As in the vortex patch case, we require a known solution as a starting point. Again, the basis for the boundary points and sheet strength are set, and the numerical method calculates the adjustment to these values:

$$x_i^n = x_i + \alpha(\tilde{s}_i) n_x, \tag{3.24}$$

$$y_i^n = y_i + \alpha(\tilde{s}_i) n_y, \tag{3.25}$$

$$\kappa_i^n = \kappa_i + \alpha_k(\tilde{s}_i), \tag{3.26}$$

where (x_i, y_i) are the boundary points and κ_i are the vortex sheet strengths. The functions α and α_k are calculated based on their Fourier coefficients, as described in Section 2.2.1. The velocity, based on the vortex sheet shape and strength (x_i^n, y_i^n) and κ_i^n, can then be calculated and the boundary kinematic and dynamic boundary conditions checked. Between iterations, the points are moved along the boundary so they are equispaced in inverse velocity. In this method, we use the average velocity on the vortex sheet (Eq. 3.1) and the straining field for the inverse velocity calculation.

The two boundary conditions are

$$F_1 = u_i \frac{\mathrm{d}y}{\mathrm{d}\tilde{s}} - v_i \frac{\mathrm{d}x}{\mathrm{d}\tilde{s}} + a t_1 x_c + b t_2 y_c + c t_3 (A - \pi) \tag{3.27}$$

$$F_2 = \left[\left(u_o^2 + v_o^2 \right) - \rho \left(u_i^2 + v_i^2 \right) \right] \lambda_s^2 - 1 + a t_1 x_c + b t_2 y_c + c t_3 (A - \pi), \tag{3.28}$$

where (u_i, v_i) and (u_o, v_o) are the total velocities on the inside and outside of the vortex sheet, (x_c, y_c) is the vortex centroid, and A is the are of the vortex. For this version of the code, we have used Legendre polynomials as the nontrivial functions t_1, t_2, and t_3,

in the hopes that it would eliminate some issues found when these functions were not orthogonal. As with the boundary element type formulation, these Legendre polynomials are functions of the normalized inverse velocity $\hat{s}$. Current tests seem to show more reliable solutions with the Legendre functions, using $a = b = c = 100$ for the constraint weights. As in the patch case, we take the FFT of both F_1 and F_2, and use the real and imaginary parts of these as the error function.

Because we are interested in the links between the vortex sheet and vortex patch, it is important to standardize the straining field. The straining field used in Llewellyn Smith and Crowdy (2012) and the previous section is aligned with the x and y axes, which leads to vortices that are symmetric about $x = y$ and $x = -y$. In the vortex patch work, we followed Moore and Saffman (1971), where the straining field is aligned with $x = y$ and $x = -y$, which leads to vortices that are symmetric about the x and y axes. In the rest of this work, we use this straining field, so that the vortices are aligned with the x and y axes.

Figure 3.3 shows the agreement between the inverse velocity calculation and the analytical solutions from Llewellyn Smith and Crowdy (2012). In the inset, showing the calculated vortex shapes with 256 points at $\lambda_s = 0.017061, 0.089225, 0.124307, 0.091360$ (black stars), and the analytical limiting shape at pinch off (red star). For the shapes indicated by the black stars, the analytical shapes have been rotated to align with the straining field, and then plotted in red underneath the black calculated shapes. These are not visible due to the agreement between the two methods. As with the boundary element type method, convergence is difficult as the distance between points becomes similar to the width of the shape, so the inverse velocity method was not able to converge at the pinch off shape.

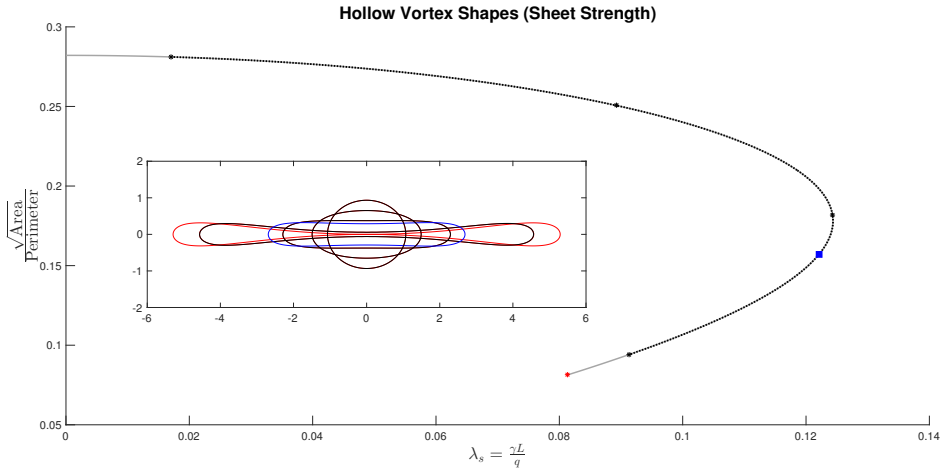

Figure 3.3: Overview of hollow vortex shapes calculated using the vortex sheet strength method. In this plot, the shape parameter is plotted against λ_s, a nondimensional parameter relating the straining field strength to the vortex sheet strength. The solid grey line shows the results obtained from Llewellyn Smith and Crowdy (2012), while the dotted black line shows the data we obtained through continuation of our sheet strength/inverse velocity method. The inset shows calculated vortex shapes plotted at the points indicated by black stars on top of red analytical shapes (not visible because of agreement). The red star indicates the limiting analytical vortex shape. The blue square shows a bifurcation point at $\lambda_s = 0.122073$, and the shape is plotted in blue in the inset.

3.2.3 Possible bifurcation point

In both the boundary element method and the inverse velocity method, we track bifurcation and fold points while performing the numerical continuation. The boundary element method found the fold point, but no other bifurcation points. The inverse velocity method found a bifurcation point shown by the blue square in Fig. 3.3. After using a perturbation method to switch branches at this point, we were unable to calculate vortex shapes that satisfied the constraints on the area and centroid. In Fig. 3.4(a), we show the shape of the hollow vortex at the calculated bifurcation point. In (b), we show one of the calculated shapes on the bifurcating branch, although this shape does not satisfy the centroid and area constraints.

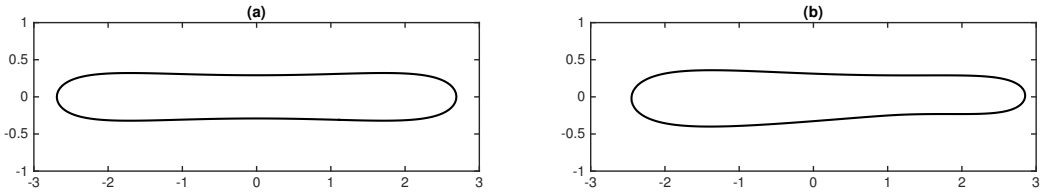

Figure 3.4: Hollow vortex shapes at bifurcation point. In (a), the vortex shape is shown at the bifurcation point at $\lambda_s = 0.122073$. In (b), a possible vortex shape is shown for the bifurcating family at $\lambda_s = 0.123651$. This vortex does not satisfy the area and centroid constraints.

3.3 Density Effects

The results shown above were calculated for the hollow case, where $\rho_{in} = 0$. This is equivalent to setting the velocity inside the vortex to be 0. In cases where $\rho_{in} \neq 0$, the steady solutions remain unchanged. This is because the flow inside the vortex is irrotational, so

$$\nabla^2 \Psi = 0 \tag{3.29}$$

inside the vortex as well. Since the vortex sheet is a streamline, Ψ has constant value along the boundary of the vortex interior. From the maximum principle, the maximum and minimum values of Ψ must occur on the vortex boundary, so Ψ is constant inside the vortex and there is no flow. Continuation in the variable ρ confirmed that it has no effect on the steady vortex sheet shapes.

3.4 Summary

In this chapter, we showed that the use of two different problem formulations, along with numerical continuation, calculated solutions that agree with the previously known hollow vortex in strain solutions. We also showed the possible location of a

bifurcation point. We then showed that the density of the fluid inside the vortex core has no effect on the solution, and in the case of an irrotational background flow the core is stagnant.

Chapter 3 is currently being prepared for submission for publication. Freilich, Daniel; Llewellyn Smith, Stefan. “The Sadovskii Vortex in Strain”. The dissertation author was the primary investigator and author of this material.

Chapter 4

The Sadovskii Vortex

In this chapter, we formulate the problem for the Sadovskii vortex, which is a combination of the previous two chapters: a vortex patch surrounded by a vortex sheet. We use the same two methods as in Chapter 2 to solve the problem. In this case, the boundary element method is used to solve for the irrotational part of the velocity inside the vortex, while a known solution is used to satisfy the rotational condition. In the inverse velocity method, we solve for the shape of the vortex using a superposition of the flows due to the vortex patch, vortex sheet, and straining field. This method groups points near sharp features, and seems to give better convergence over the solution manifold.

Problem Description

The Sadovskii vortex is a patch of fluid with uniform vorticity surrounded by a vortex sheet. This is a combination of the two previously discussed desingularizations. Inside the vortex, we require constant vorticity, so we solve Poisson's equation

$$\nabla^2 \Psi = -\omega, \tag{4.1}$$

where Ψ is the stream function and ω is the vorticity. Outside the vortex, the flow is irrotational, so we solve Laplace's equation

$$\nabla^2\Psi = 0. \tag{4.2}$$

Since we're interested in solving for the solution in a straining field, we require that far from the vortex, the stream function looks like strain with a point vortex,

$$\Psi \sim \gamma\left(x^2 - y^2\right) - \frac{\Gamma}{2\pi}\ln|z| \quad \text{as} \quad |z| \to \infty, \tag{4.3}$$

where γ is related to the strength of the straining field.

We require the boundary of the vortex to be a streamline, which means that

$$\Psi = \text{constant} \tag{4.4}$$

on the boundary of the vortex. Since we can define the stream function Ψ up to a constant without a loss of generality, we set $\Psi = 0$ on the boundary.

Finally, if the boundary of the vortex is a vortex sheet, there will be a discontinuity in the velocity there, which can be written as a Bernoulli-type condition

$$\frac{\rho_{out}}{2}\left|\mathbf{U}_{T(out)}\right|^2 - \frac{\rho_{in}}{2}\left|\mathbf{U}_{T(in)}\right|^2 = Q, \tag{4.5}$$

where ρ_{in} is the density inside the vortex core, ρ_{out} is the density outside the vortex, $U_{T(in)}$ is the total velocity on the inside edge of the vortex sheet, and $U_{T(out)}$ is the total velocity on the outside edge of the vortex sheet. As in the patch case, setting $\Psi = 0$ on the boundary eliminates the term due to the constant vorticity.

In the limiting case where the vortex sheet has zero strength, $U_{T(in)} = U_{T(out)}$ and

this is just the patch case. The case where the vorticity is zero ($\omega = 0$) is the vortex sheet case.

4.1 Solution methods

As in the vortex sheet case, there are two types of methods to solve for the steady states of the Sadovskii vortex. The boundary element type method is more general. This method assumes the stream functions inside and outside the vortex can be separated into different components. For the stream function inside the vortex, where the vorticity patch exists, the velocity field is separated into a known rotational part that satisfies Poisson's equation, and an unknown part that is irrotational. Outside the vortex, the velocity field is separated into a contribution from the straining field and an irrotational part due to the circulation of the vortex patch and sheet. This method has more unknowns, since the location of the vortex boundary, as well as the velocities inside and outside the vortex at those points, must be solved for.

The other method assumes the velocity field of the steady solution can be written as a superposition of the velocity due to the vortex patch, vortex sheet, and the straining field. This method combines the work of the previous chapters, in which the boundary points are discretized according to the inverse velocity. In the vortex patch case, the velocity due to the vorticity could be written as a contour integral around the vortex boundary, and is a function of the boundary and the vorticity alone:

$$\mathbf{u}_{\text{patch}}(\mathbf{x}) = \frac{\omega}{2\pi} \oint \frac{\mathbf{x}-\mathbf{X}}{|\mathbf{x}-\mathbf{X}|^2}(\mathbf{x}-\mathbf{X}) \cdot \frac{\mathrm{d}\mathbf{X}}{\mathrm{d}\tilde{s}} \mathrm{d}\tilde{s}. \tag{4.6}$$

If the vortex sheet strength is known at each point on the vortex boundary, the velocity

due to the vortex sheet can be calculated as a contour integral:

$$u_{\text{sheet}}(z) - \mathrm{i}v_{\text{sheet}}(z) = \frac{-\mathrm{i}}{2\pi}\fint \frac{\kappa(s')\mathrm{d}s'}{z - Z(s')} \pm \frac{\kappa}{2}\left(x' - \mathrm{i}y'\right), \tag{4.7}$$

where $(u_{\text{sheet}}, v_{\text{sheet}})$ is the velocity just on the outside of the vortex boundary for the positive sign, and just on the inside of the vortex boundary for the negative sign. This is the equation for the velocity at the vortex sheet from Saffman (1992) in the steady state.

4.1.1 Boundary element type formulation

In the boundary element formulation, we use the location of the boundary points x and y as variables, as well as the velocities both inside and outside the vortex. This leads to a total of $6N$ variables: $x, y, u_{in}, v_{in}, u_{out}, v_{out}$. While the above overview of the problem was given in terms of conditions on the stream function, they can be rewritten to use the positions and velocities of the boundary points.

The velocities can be separated into rotational and irrotational parts. Inside the vortex, the velocity field $(-\omega y/2, \omega x/2)$ has the correct vorticity. The irrotational velocity is then the unknowns (u_{in}, v_{in}), and the total velocity is $(u_{in} - \omega y/2, v_{in} + \omega x/2)$. Outside the vortex, the velocity due to the straining field is $(-2\gamma x, -2\gamma y)$, and the irrotational velocity due to the circulation of the vortex, is the unknowns (u_{out}, v_{out}), so that the total outside velocity is $(u_{out} - 2\gamma y, v_{out} - 2\gamma x)$.

This formulation uses an equispaced by arclength parameterization, which leads to the condition

$$\left(\frac{\mathrm{d}x}{\mathrm{d}s}\right)^2 + \left(\frac{\mathrm{d}y}{\mathrm{d}s}\right)^2 = 1. \tag{4.8}$$

The dynamic boundary condition is a Bernoulli condition,

$$\rho_{out}\left|\mathbf{U}_{out}\right|^2 - \rho_{in}\left|\mathbf{U}_{in}\right|^2 = q^2, \tag{4.9}$$

where $\mathbf{U}_{out} = (u_{out} - 2\gamma y, v_{out} - 2\gamma x)$ and $\mathbf{U}_{in} = (u_{in} - \omega y/2, v_{in} + \omega x/2)$. The kinematic conditions require that the boundary of the vortex is a streamline, so there must be no normal flow across the vortex boundary:

$$\left(-\frac{\omega}{2}y + u_{in}\right) y' = \left(\frac{\omega}{2}x + v_{in}\right) x' \tag{4.10}$$

$$(-2\gamma x + u_{out})\, y' = (-2\gamma y + v_{out})\, x'. \tag{4.11}$$

The last two equations are the Cauchy conditions, which require that the velocities we are solving for are harmonic. These are enforced through

$$v_i(t) = \mathrm{Im}\left\{ \frac{\mathrm{i}}{\pi} \oint \frac{(u_i + \mathrm{i}v_i)}{[x + \mathrm{i}y] - [x(t) + \mathrm{i}y(t)]} \left(\frac{\mathrm{d}x}{\mathrm{d}s} + \mathrm{i}\frac{\mathrm{d}y}{\mathrm{d}s} \right) \mathrm{d}s \right\}, \tag{4.12}$$

$$v_o(t) = \mathrm{Im}\left\{ -\frac{\mathrm{i}}{\pi} \oint \frac{(u_o + \mathrm{i}v_o)}{[x + \mathrm{i}y] - [x(t) + \mathrm{i}y(t)]} \left(\frac{\mathrm{d}x}{\mathrm{d}s} + \mathrm{i}\frac{\mathrm{d}y}{\mathrm{d}s} \right) \mathrm{d}s \right\}. \tag{4.13}$$

These integrals have opposite signs because they must be traversed in opposite directions, since one is for inside the contour and the other is for outside the contour.

There are two basic ways to nondimensionalize this problem. One formulation works better for solutions near the vortex sheet, while the other formulation works better near the vortex patch solutions with a weaker vortex sheet.

4.1.2 Nondimensionalization near vortex sheet

Near the vortex sheet solution, we nondimensionalize with respect to the straining field strength γ. This is the same nondimensionalization as we used in the sheet case, with the added parameter μ_s to incorporate the inside vorticity, and this formulation works better for solutions near the hollow case. The nondimensionalization is

$$x = Lx^*, \quad u = L\gamma u^*, \quad \mu_s = \frac{\omega}{\gamma}, \quad \lambda_s = \frac{\gamma L}{q}, \quad \rho = \frac{\rho_i}{\rho_o}, \tag{4.14}$$

and this leads to the following boundary conditions:

$$\lambda_s^{-2} = \left[(u_{out} - 2y)^2 + (v_{out} - 2x)^2\right] - \rho\left[\left(u_{in} - \frac{\mu_s}{2}y\right)^2 + \left(v_{in} + \frac{\mu_s}{2}x\right)^2\right], \tag{4.15}$$

$$0 = \left(u_{in} - \frac{\mu_s}{2}y\right)\frac{dy}{ds} - \left(v_{in} + \frac{\mu_s}{2}x\right)\frac{dx}{ds}, \tag{4.16}$$

$$0 = (u_{out} - 2y)\frac{dy}{ds} - (v_{out} - 2x)\frac{dx}{ds}. \tag{4.17}$$

The Cauchy conditions remain unchanged by nondimensionalization.

4.1.3 Nondimensionalization near vortex patch

The second nondimensionalization is with respect to the vorticity inside the core. The vortex patch solutions have $0 \leq \gamma/\omega < 0.8$, so it makes sense to use ω. We use the same nondimensionalization used for the vortex patch case, with the new parameter λ to incorporate the vortex sheet. Here, the nondimensionalization is

$$x = Lx^*, \quad u = L\omega u^*, \quad \mu = \frac{\gamma}{\omega}, \quad \lambda = \frac{q}{\omega L}, \quad \rho = \frac{\rho_i}{\rho_o}, \tag{4.18}$$

and the boundary conditions are

$$\lambda^2 = \left[(u_{out} - 2\mu y)^2 + (v_{out} - 2\mu x)^2\right] - \rho\left[\left(u_{in} - \frac{y}{2}\right)^2 + \left(v_{in} + \frac{x}{2}\right)^2\right], \tag{4.19}$$

$$0 = \left(u_{in} - \frac{y}{2}\right)\frac{dy}{ds} - \left(v_{in} + \frac{x}{2}\right)\frac{dx}{ds}, \tag{4.20}$$

$$0 = (u_{out} - 2\mu y)\frac{dy}{ds} - (v_{out} - 2\mu x)\frac{dx}{ds}. \tag{4.21}$$

4.1.4 Validation

Although the boundary element method assumes only the form of the rotational part of the solution inside the vortex, the results can be checked using the known form of

the solution. From the velocity at each boundary point, the vortex sheet strength at each point is

$$\kappa(s) = \sqrt{(u_{out} - 2\mu y)^2 + (v_{out} - 2\mu x)^2} - \sqrt{\left(u_{in} - \frac{y}{2}\right)^2 + \left(v_{in} + \frac{x}{2}\right)^2}. \tag{4.22}$$

This allows calculation of the velocity due to the vortex sheet through a trapezoidal rule integration of Eq. 4.7, since the points are equispaced in s. The velocity due to the vortex patch can be calculated from Eq. 4.6. The total velocity will also include the contribution from the straining field, that is,

$$U_T = u_{\text{sheet}} + u_{\text{patch}} + u_{\text{strain}}, \tag{4.23}$$

where U_T is the total velocity in the x direction. The equation is similar for V_T. While the patch and strain terms are the same on both sides of the vortex sheet, the velocity due to the vortex sheet depends on whether the point is inside or outside the vortex. Putting these velocities in terms of the quantities calculated by the boundary element type method,

$$u'_{in} = u_{\text{sheet}} + u_{\text{patch}} - 2\mu y + \frac{y}{2}, \tag{4.24}$$

$$v'_{in} = v_{\text{sheet}} + v_{\text{patch}} - 2\mu x - \frac{x}{2}, \tag{4.25}$$

$$u'_{out} = \tilde{u}_{\text{sheet}} + u_{\text{patch}}, \tag{4.26}$$

$$v'_{out} = \tilde{v}_{\text{sheet}} + v_{\text{patch}}. \tag{4.27}$$

Comparison of the original velocities (u_{in}, v_{in}) and (u_{out}, v_{out}) with the newly calculated quantities (u', v') indicates whether the boundary element method calculates solutions with the expected form. Since these calculations are performed with 128 points, the expected error for the integrals is $O(h^{-2}) = O(10^{-3})$, where h is the arclength

between points. For solutions that appear physical, the error was $O(10^{-3})$. When the error was larger than that, the solutions seemed to be nonphysical.

Results

Continuation in μ for the patch solutions using equispaced points allowed investigation of the bifurcation point at $m = 4$. Depending on which starting point was used, continuation with 128 points from the elliptical family would either pass the bifurcation point while remaining on the elliptical family (solid line in Fig. 4.1), or it would continue onto the bifurcating family with the pinch off (dashed line). In (b), one of the dashed lines was continuation that began above the bifurcation point, while the other began below. With the equispaced points, the numerical continuation only accesses solutions on the branch with the pinch off. However, we know from Chapter 2 and Kamm (1987) that there is another branch on the other side of the bifurcation point with sharp cusps on both ends.

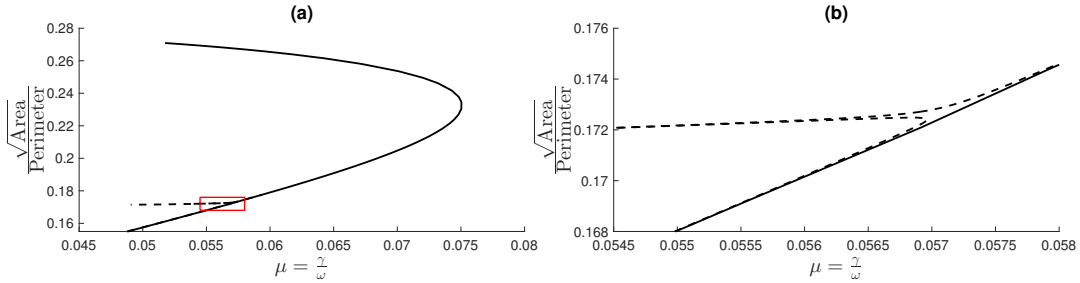

Figure 4.1: A plot of the $m = 4$ bifurcation in the patch case, with $\lambda = 0$, using equispaced points. The solid line shows continuation that passed through the bifurcation point, while the dashed line shows continuation that switched branches at the bifurcation point. (a) gives an overview, while (b) shows an enlarged view of the area shown by the red box in (a).

Beginning with these vortex patch solutions, continuation using equispaced points was performed around this bifurcation point to investigate the behavior of the bifurcating families as the vortex sheet was turned on. As soon as the vortex sheet is turned on, the bifurcation point disappears, and the elliptical patch vortex family becomes split.

The more circular elliptical vortices above the bifurcation point remain connected to the bifurcating family with the pinch off, but the more elongated elliptical family becomes connected to the family with the sharp corners. This can be seen in Fig. 4.2, where the solid line shows the family with the more circular ellipses and those with a pinch off, and the dashed line shows the family with the sharp corners and the more elongated ellipses. As λ is increased, the two families become farther away from each other. Figure 4.2 can be compared directly with Fig. 4.1(b), as both figures have the same limits and are the same size. The values of λ in Fig. 4.2 are not equal because the continuation in μ was begun from a previous continuation in λ, and these two continuations in μ did not calculate shapes at identical values of λ.

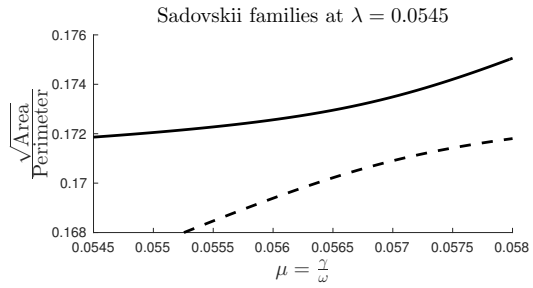

Figure 4.2: A plot of the $m = 4$ bifurcation for Sadovskii vortices near $\lambda = 0.0545$, using 128 equispaced points. The solid line ($\lambda = 0.0545547$) shows the family of more circular ellipses that is now connected with the pinch off, while the dashed line ($\lambda = 0.0543887$) shows the more elongated ellipses that are now connected with the family with sharper corners. This figure can be compared directly with Fig. 4.1(b), as both figures are the same size and have the same limits.

Although continuation using equispaced points was unable to calculate the solutions with two cusps in the patch case (Fig. 4.1), once the vortex sheet was turned on and the families split at the bifurcation point, these shapes were calculated by the code, as they are on the dashed line in Fig. 4.2 and Fig. 4.3(b). The family in Fig. 4.2 shown by the dashed line ends when the solutions no longer satisfied the area and centroid calculations, or failed the validation test of the velocities.

Some shapes of Sadovskii vortices are plotted in Fig. 4.3. In (a) is an example

of a shape on the branch with the pinch off. In (b) is the last converging shape on the branch with the sharper corners, which is connected to the more elongated ellipses. It is clear in (b) that the use of 128 points that are equispaced in arclength does not give much resolution near the sharp corners, which makes it difficult to determine the shape of the vortex at these points. Although the addition of the vortex sheet eliminates the cusps this shape can be compared to those in Fig. 2.8(b) and (d), which used more points and clustered them at the corners.

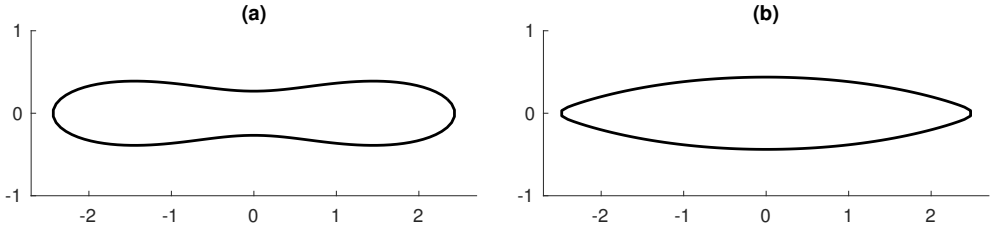

Figure 4.3: This figure shows two Sadovskii vortex shapes with 128 equispaced points. In (a), a shape on the branch with the pinch off at $\mu = 0.049128$, $\lambda = 0.054232$. In (b), the last shape to converge with sharp corners and 128 points, with $\mu = 0.060079$ and $\lambda = 0.054389$.

4.2 Inverse Velocity Formulation

In the inverse velocity formulation, points are clustered in areas where the velocity on the vortex sheet is lower. This method assumes a form of the solution, in that it treats the full flow as a superposition of three velocity fields: the background straining flow, the vortex patch, and the vortex sheet. It is a combination of the inverse velocity formulations used for the vortex patch and vortex sheet solutions in Chapters 2 and 3. This method uses less unknowns than the boundary element method, since the method solves for adjustments to the boundary position of the vortex and the vortex sheet strength.

As in the inverse velocity methods presented in the vortex patch and sheet chapters,

this method begins with a known solution. The boundary points are then rediscretized according to the inverse velocity, using cubic splines to evaluate the location of the new points and the new vortex sheet strength at these points. The normal vectors to the vortex boundary are then frozen in space, and the method calculates the adjustments to the boundary points along these normal vectors, as well as the adjustment to the vortex sheet strength, through

$$x_i^n = x_i + \alpha(\tilde{s}_i)n_x, \tag{4.28}$$

$$y_i^n = y_i + \alpha(\tilde{s}_i)n_y, \tag{4.29}$$

$$\kappa_i^n = \kappa_i + \alpha_k(\tilde{s}_i), \tag{4.30}$$

where (x_i, y_i) are the boundary points and κ_i are the vortex sheet strengths. As in both the vortex patch (Section 2.2.1) and vortex sheet chapters, the functions α and α_k are calculated based on their Fourier coefficients.

Given the location of points on the vortex boundary, and the vortex sheet strength at those points, all necessary values can be computed for solving the boundary conditions. There are essentially two unknowns in this problem, the M complex Fourier coefficients of α and the M complex Fourier coefficients of α_k. The two boundary conditions are that the vortex boundary is a streamline so there is no normal flow,

$$\mathbf{u} \cdot \mathbf{n} = 0, \tag{4.31}$$

and the dynamic (Bernoulli) condition,

$$\rho_{out} |\mathbf{U}_{out}|^2 - \rho_{in} |\mathbf{U}_{in}|^2 = q^2. \tag{4.32}$$

In this notation, $\mathbf{U} = \mathbf{u}_{\text{patch}} + \mathbf{u}_{\text{sheet}} + \mathbf{u}_{\text{strain}}$, where $\mathbf{u}_{\text{patch}}$ is calculated from Eq. 4.6 and

$\mathbf{u}_{\text{sheet}}$ is calculated from Eq. 4.7. Just as the average velocity on the vortex boundary is used for the discretization of the points, that average velocity (which is the principal value part of Eq. 4.7, without the $\pm\kappa(x' - \mathrm{i}y')/2$ term), it is also used in the kinematic condition. This works because the additional term, due to the vortex sheet at the point of interest, is defined to change the velocity only in the tangential direction, and so can't affect the normal velocity.

As in the previous chapters, we actually solve a constrained problem, where each of the boundary conditions has added terms to ensure the vortex is centered at the origin and has a set area. The area and centroids are calculated from

$$A = \oint x \frac{\mathrm{d}y}{\mathrm{d}\tilde{s}} \mathrm{d}\tilde{s}, \quad x_C = -\frac{1}{2A} \oint x^2 \frac{\mathrm{d}y}{\mathrm{d}\tilde{s}} \mathrm{d}\tilde{s}, \quad \text{and} \quad y_C = \frac{1}{2A} \oint y^2 \frac{\mathrm{d}x}{\mathrm{d}\tilde{s}} \mathrm{d}\tilde{s}. \tag{4.33}$$

The constraints, which are then added to Eqs. 4.31 and 4.32, are

$$a t_1 x_c + b t_2 y_c + c t_3 (A - \pi) = 0, \tag{4.34}$$

where a, b and c are weights, and t_1, t_2, t_3 are the first three Legendre polynomials. We used weights of $a = b = c = 100$ unless otherwise noted.

After continuation was completed, the data was checked to make sure it satisfied the area and centroid constraints. After reviewing much of the data, we found that high frequency Nyquist mode oscillations or nonphysical shapes seemed to occur when $|x_c| > 5 \times 10^{-7}$, $|y_c| > 5 \times 10^{-7}$, or $|A - \pi| > 5 \times 10^{-6}$. We then used these limits to throw out any converged solutions that had the area or centroids larger than these values. In the rest of this dissertation, the end of convergence should be understood to mean either the code was unable to converge, or the solutions had centroid or area errors that were too large.

4.2.1 Comparing vortex patch and sheet solutions

The nondimensional parameters used for numerical continuation to compute solutions of the Sadovskii vortex were

$$\mu = \frac{\gamma}{\omega}, \quad \lambda = \frac{q}{\omega L}, \quad \text{and} \quad \mu_s = \frac{\omega}{\gamma}, \quad \lambda_s = \frac{\gamma L}{q}. \tag{4.35}$$

In order to compare solutions computed with both nondimensionalizations, the relations are

$$\mu = \frac{1}{\mu_s} \quad \text{and} \quad \lambda = \frac{1}{\lambda_s \mu_s}. \tag{4.36}$$

In this parameter space, vortex sheet solutions have undefined values for μ and λ, and vortex patch solutions have undefined values of λ_s. To allow comparison of sheet and patch solutions, as well as all Sadovskii solutions in between, we use a different set of nondimensional parameters based on the total circulation.

There are two roles we want these parameters to play: the first is to give a measure of how much of the vortex strength is due to the uniform vortex patch, and how much is due to the vortex sheet. The other parameter measures how strong the vortex is relative to the background straining field. In the cases we are considering, where the vortex sheet and vortex patch have the same sign of vorticity, the circulation outside the vortex core will be nonzero for the patch, sheet, and all Sadovskii vortices. This provides a good measure of the total strength of the vortex.

For the parameter relating the vortex patch strength to the vortex sheet strength, we use the parameter

$$\Lambda = \frac{\Gamma_{in}}{\Gamma_{out}}. \tag{4.37}$$

The vortex patch has $\Lambda = 1$, the vortex sheet has $\Lambda = 0$, and Sadovskii vortices are in the range $0 < \Lambda < 1$.

For the parameter relating the straining field strength to the vortex strength, we use

$$S_r = \frac{\gamma L^2}{\Gamma_{out}}. \tag{4.38}$$

This parameter goes to 0 for solutions that are circular, where the vortex is much stronger than the straining field, and it has an upper bound for all patch, sheet, and Sadovskii solutions. This parameter is similar to the parameter μ_h used in Llewellyn Smith and Crowdy (2012) (see Eq. 3.8).

These two parameters, Λ and S_r, allow us to plot all Sadovskii solutions in a finite area in the parameter space. To calculate the circulation outside the vortex, we use the definition

$$\Gamma_{out} = \oint_{\partial S} \mathbf{u}_{out} \cdot \mathrm{d}\mathbf{s}, \tag{4.39}$$

where $\mathbf{u}_{out}$ is the total velocity just outside the vortex boundary and ∂S is the boundary of the vortex. Since the flow is irrotational outside the vortex, any contour that encloses the vortex will give the same value for Γ_{out}. To calculate Γ_{in}, we again use the definition of circulation, but evaluate the contour just inside the vortex sheet on the vortex boundary:

$$\Gamma_{in} = \oint_{\partial S} \mathbf{u}_{in} \cdot \mathrm{d}\mathbf{s}. \tag{4.40}$$

An equivalent way to write these circulations to show the effect of the different parts of the vortex are

$$\Gamma_{in} = \omega A \quad \text{ and } \Gamma_{out} = \Gamma_{in} + \oint_{\partial S} \kappa \mathrm{d}s, \tag{4.41}$$

where A is the area of the vortex patch and κ is the vortex sheet strength.

4.3 Results

Figure 4.4 shows the calculated solutions of Sadovskii vortices. At $\Lambda = 1$, it includes the vortex patch data, and at $\Lambda = 0$, it includes the vortex sheet data. Blue and green solutions are computed using the vortex patch nondimensionalization (see Eq. 4.18), while the red solutions are computed using the vortex sheet nondimensionalization (see Eq. 4.14). The black circles mark calculated fold points in these nondimensionalizations, while the xs mark calculated bifurcation points. The black stars mark the expected bifurcation points of the patch family (from Moore and Saffman (1971). It is hard to comprehend all the details about Fig. 4.4 from only those plots, so the rest of this chapter focuses on going through the interesting parts of the solution manifold.

For solutions using the patch nondimensionalization (blue and green), continuation in λ led to the lines of solutions that mostly span Λ, while solutions that mostly span S_r are from continuation in μ. For the red solutions calculated with the sheet nondimensionalization, continuation in μ_s led to lines of solutions that mostly span Λ, while continuation in λ_s led to line of solutions that mostly span S_r. In areas where solutions from both nondimensionalizations were computed, solutions from each fall on the same manifold and give the same solutions.

In the figure, the calculated fold points for solutions with $\Lambda \neq 1$ do not occur at the actual fold points in $S_r = \gamma L^2/\Gamma_{out}$. This is because fold points are artifacts of the choice of continuation parameter (note that bifurcation points are not artifacts of parameter choice, and their actual location on the family doesn't change with the parameter choice). For vortex patch solutions, with $\Lambda = 1$, S_r is a scaling of μ, so the fold points are the same in both μ and S_r. In all other cases, this is not true. In Fig. 4.5, we show this difference for the sheet vortex case with $\Lambda = 0$. While the actual location of the fold points isn't important, it shows the direction continuation will go in the shape parameters. In the

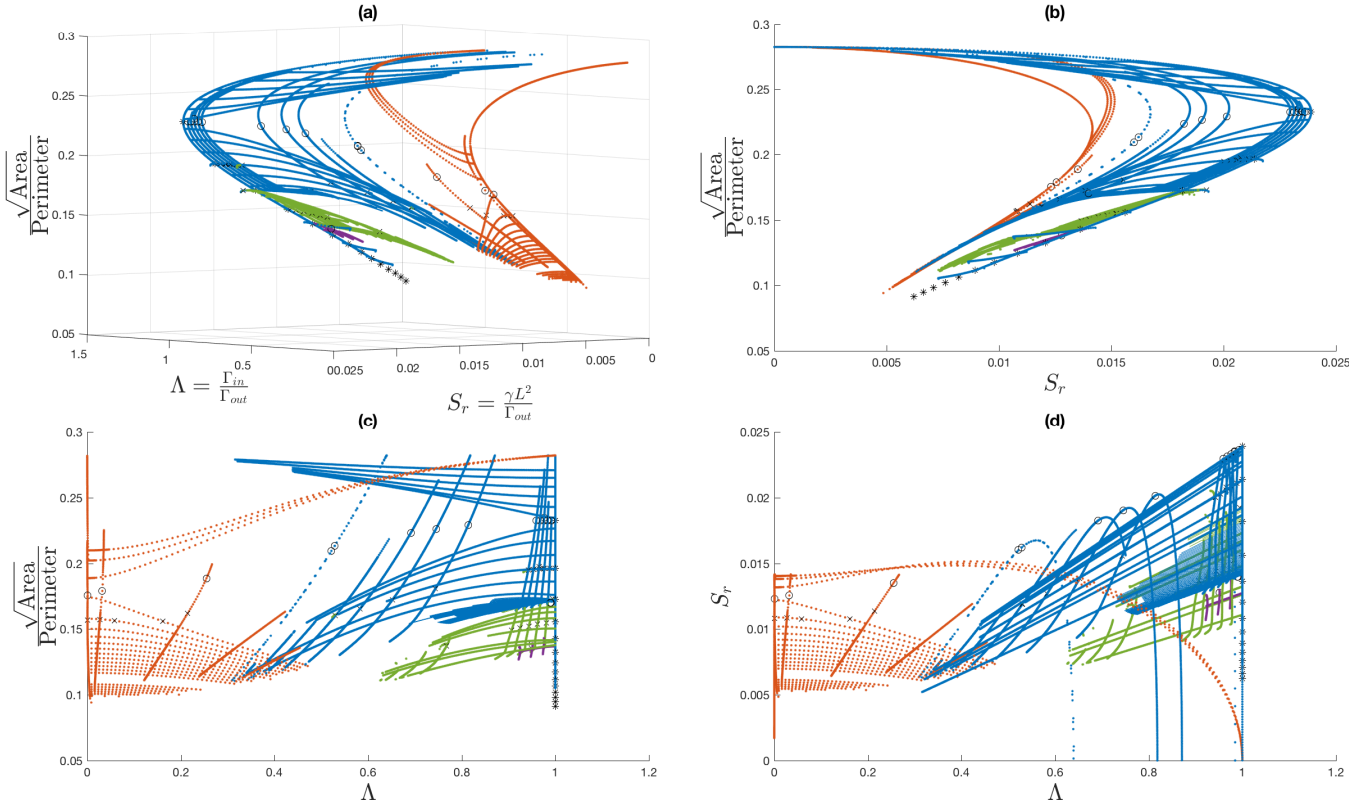

Figure 4.4: Overview of Sadovskii vortex shapes. Each panel shows a different view of the same solutions. Red solutions are calculated using the sheet nondimensionalization, while the blue and green solutions are calculated using the patch nondimensinoalization. The red and blue solutions are in the same family and are connected, while the green family is not connected to that family for $\Lambda < 1$. The purple solutions are the third family, which are also not connected to the other families for $\Lambda < 1$. Black stars show bifurcation points predicted by Moore and Saffman. Black xs represent bifurcation points, and black circles represent fold points in the continuation variables.

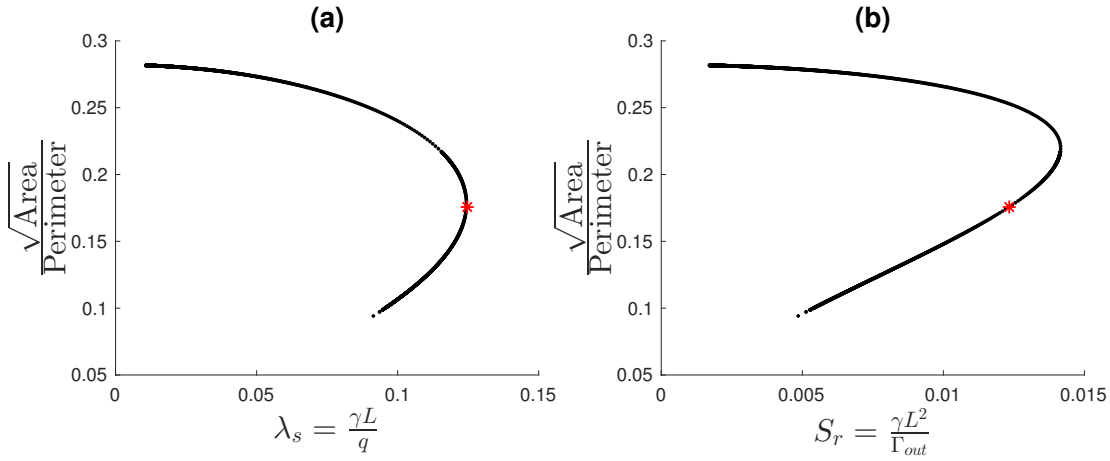

Figure 4.5: Comparison of fold point location for the vortex sheet solutions. In (a), the shape parameter is plotted against λ_s, the parameter used to calculate solutions. In (b), the shape parameter is plotted against S_r, the parameter used to plot the Sadovskii solutions. The black dots indicate solutions that have been calculated, and the red stars show the location of the fold points in λ_S.

cases of increasing λ or μ_s in the patch and sheet nondimensional variables, respectively, this is the same as increasing the total circulation of the vortex. This will result in a decrease in S_r, which can be seen in Fig. 4.4. If the continuation begins above the fold point in λ or μ_s, the solutions will become more circular as the shape parameter increases. If the continuation begins below the fold point, the solutions will become more elongated as the shape parameter decreases. This is visible in the overview plot as the blue and red lines diverge from the fold points.

In the calculations using the boundary element type method, the bifurcation point for the patch case at $m = 4$ was seen to lead to a split in the solution families of the Sadovskii vortex. This split is also evident in the calculations using the inverse velocity method, and can be seen in Fig. 4.4 from the space between the blue and green solutions, and the way only the blue solutions connect to the red solutions. Since calculations were performed in λ and μ, it is easier to show this split in those variables.

Figure 4.6 shows the split between the families occurring. As λ increases, the families get farther apart. In (a), the vortex patch case, the families are still connected. In

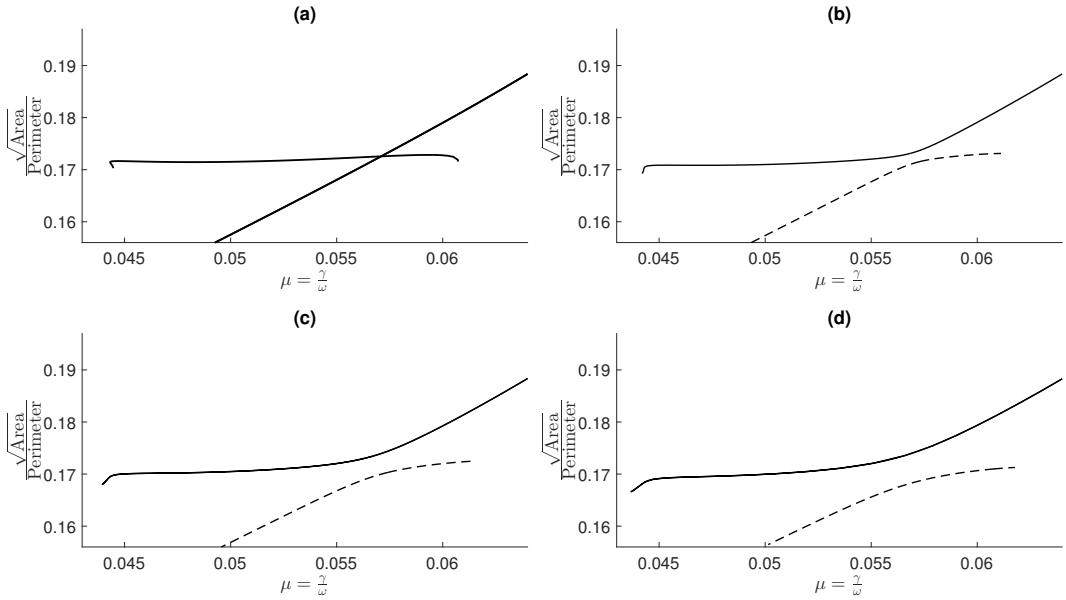

Figure 4.6: Split in Sadovskii vortex families near the $m = 4$ bifurcation point. Patch solutions with $\lambda = 0$ are shown in (a). In (b), (c), and (d), Sadovskii solutions are shown at constant values of $\lambda \approx 0.051, 0.072, 0.089$, respectively. In (b), (c), and (d), the upper family is shown in the solid line and the more elongated family is shown by the dashed line. As λ increases, these families get farther from each other.

(b), the families have split and the upper (more circular) family is shown at $\lambda = 0.050586$, while the dashed line shows the more elongated family at $\lambda = 0.050667$. In (c), the top family is shown at $\lambda = 0.071905$, while the bottom family is shown at $\lambda = 0.071899$. In (d), the top family is shown at $\lambda = 0.088796$, while the bottom family is shown at $\lambda = 0.088728$. The discrepancy in the λ values is due to the starting vortex configurations of the vortices. In order to continue in μ for $\lambda \neq 0$, continuation must first be performed in λ, and continuation of the upper and lower branch did not solve for exactly the same values of λ.

As discussed previously, the top family of more circular vortices remains attached to the family with the pinch off, while the family of patch vortices with sharp cusps becomes attached to the lower family of more elongated shapes. At the next even bifurcation point, $m = 6$, this same split occurs again, so that the lower family (dashed

line) in Fig. 4.6 is also attached to the family with two pinch off points (see Fig. 4.13).

This split in the solution families at even m bifurcation points is important. It explains the difference between the vortex patch and vortex sheet bifurcation diagrams. In the case of the vortex patch, there exist bifurcation points with even m values, and at these points the elliptical solution family is crossed by two branches, one of which has a pinch off point and the other which has cusps at both ends. The addition of any amount of vortex sheet ($\Lambda < 1$) removes the cusps, and in doing so also separates these families. What had previously been a single elliptical family is split into two, with the more circular shapes staying connected to the shapes that include a pinch offs. The more elongated elliptical shapes stay connected to the family with cusps at both ends. This pattern continues at each even value of m on the patch family. It seems that the only solutions that exist for $\Lambda = 0$ are the upper branch, which connects the circular solutions to the solutions with a single pinch off.

4.3.1 Upper branch

The upper branch is shown in red in Fig. 4.7. This is the portion of the Sadovskii solution manifold that connects the vortex patch solutions with the vortex sheet solutions. As the figure shows, this only includes the solutions that were circular or had a single pinch off, but does not include those that had cusps at both ends, were more elongated, or had more than one pinch off.

Generally, it seems the vortex sheet leads to more rounded shapes, as the vortex sheet cannot exist at cusps (discussed in conversations with S. Tanveer; see also Saffman and Tanveer (1982)). As Λ is decreased from 1, the sharp features that exist on the limiting patch vortex shapes become smooth. In the case of the circular vortices, which have a large shape parameter but small S_r, the shapes do not change. This is because they have circular vortices for the limiting cases of the patch and sheet vortices, and all

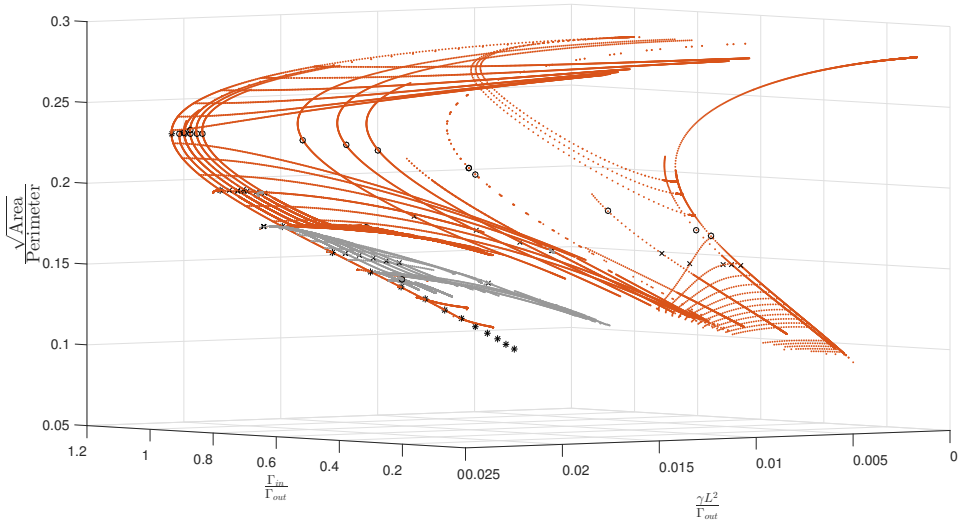

Figure 4.7: The connection between the upper portion of the patch vortex solutions and the entire vortex sheet solution family. The upper branch is plotted in red, while the rest of the Sadovskii solutions are plotted in grey.

Sadovskii vortices in between. This the expected result, since a circular shape is a known solution for a vortex with no other flow field.

The effect of the combination of the two sources of circulation are evident in the limiting shapes of vortices with a single pinch off. This type of vortex exists for both the patch and sheet cases, although with different shapes. In Fig. 4.8, the last converged shapes are shown for various values of Λ. In the patch case, the limiting shape had sharp cusps at the pinch off points, shown in (a). In the vortex sheet case, there is a much smoother transition from the ends to the pinch off in the center, shown in (d). Beginning at the vortex patch, as the vortex sheet strength is increased, the shape of the vortex in the area of the pinch off smooths out and begins to look more like the vortex sheet shape, as shown in (b) and (c). The Sadovskii shapes didn't converge all the way to the pinch off point. It seems the code has difficulty converging when the distance between the boundary points becomes similar to the minimum width of the shape.

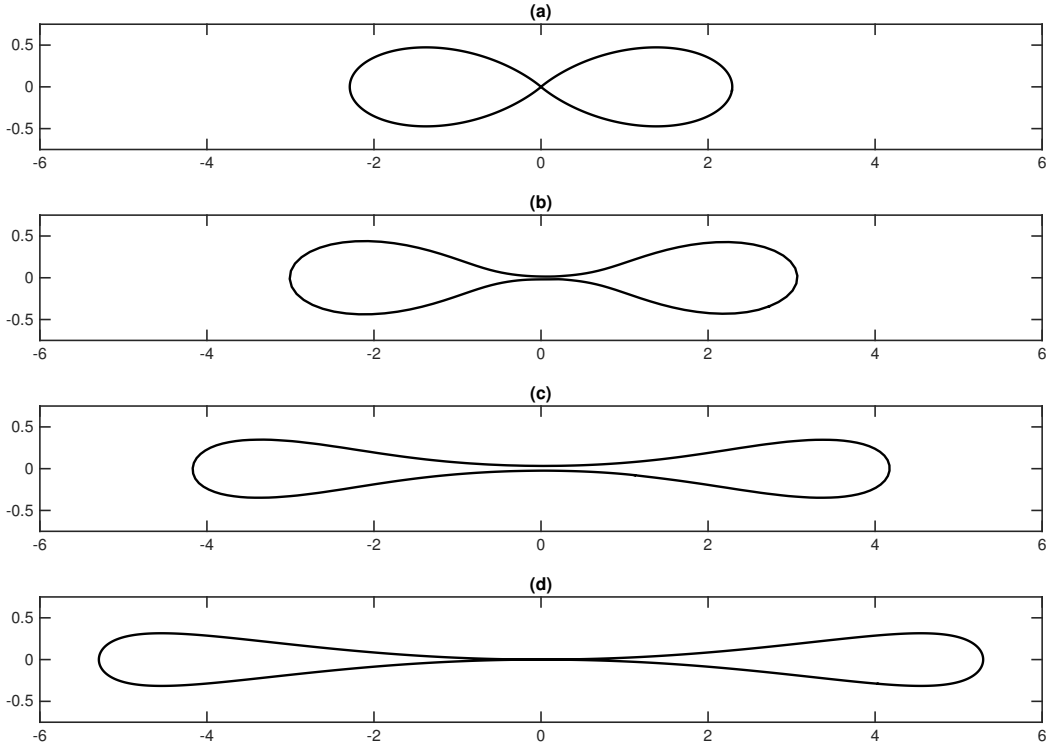

Figure 4.8: A plot of the closest shapes to pinch off for various sheet and vorticity strengths. In (a), the vortex patch shape, with $\Lambda = 1$, using 512 points (see Fig. 2.8(c)). In (b), the last converged Sadovskii shape with $\Lambda = 0.62533$, using 128 points. In (c), the last converged Sadovskii shape with $\Lambda = 0.29238$, using 256 points. In (d), the the theoretical limit for the vortex sheet, from Llewellyn Smith and Crowdy (2012) (see Fig. 3.3).

Bifurcation at $m = 3$

While the bifurcation point at $m = 4$ caused a split in the solution families for $\Lambda < 1$, the asymmetric bifurcating family at $m = 3$ remained attached to the upper family. This pattern of splitting of families at even numbered values of m, while the bifurcating families at odd values of m remain attached to the family, seemed to continue for higher values of m on other branches.

Figure 4.9 shows the location of the bifurcation points for both $m = 3$ and $m = 5$. In this figure, the bifurcation points for the family $m = 3$ are shown by the plus signs, while the bifurcation points for the $m = 5$ family is shown by black stars. The red circles

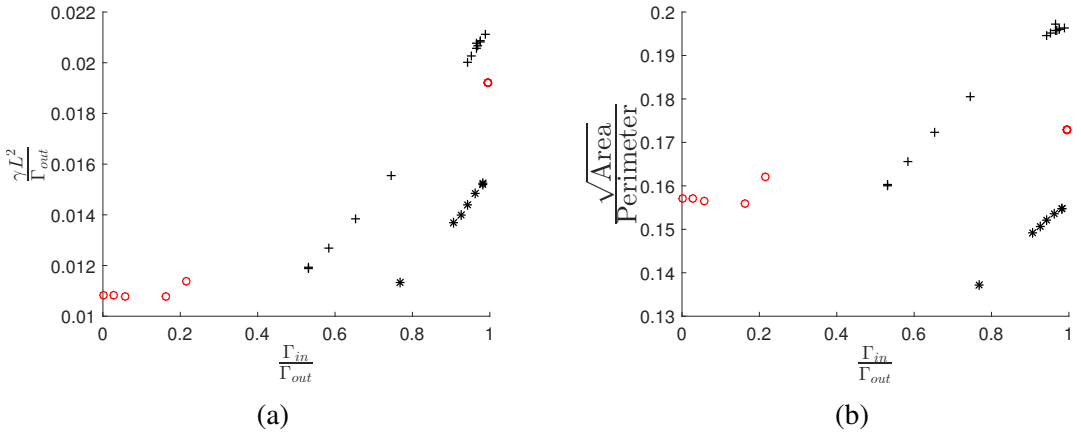

(a) (b)

Figure 4.9: Plots of the bifurcation points for the Sadovskii vortices. Black plus signs are the bifurcation points at $m = 3$, and black stars are the bifurcation points at $m = 5$. The red circles are questionable bifurcation points.

indicate calculated bifurcation points that are possibly spurious. As Λ is decreased, these bifurcation points move to smaller values of S_r (see Fig. 4.9a), and the shape parameter also gets smaller (see Fig. 4.9b).

Figure 4.10 shows the vortex shapes at the $m = 3$ bifurcation point for three different points on the solution manifold. As the bifurcation points move to smaller values of the shape parameter and strain ratio, they take on more of the characteristics of the shapes that were originally on the bifurcating branch at $m = 4$, showing the flattening out and then beginnings of the pinch off in the center.

To calculate the shapes of the asymmetric vortices on the bifurcating families at $m = 3$, we calculated a perturbed solution near the bifurcation point, then used this perturbed solution as a starting point for continuation in μ. Using increased weights on the centroid and area constraints ($a = b = c = 10^5$ instead of 100) gave better convergence to solutions.

In the vortex patch case, the limiting shape for this solution branch had a cusp, shown in Fig. 4.11(a). As the vortex sheet strength increases, the vortex can no longer support a cusp. Instead, the effect of the sheet is to round the cusp out, and it begins

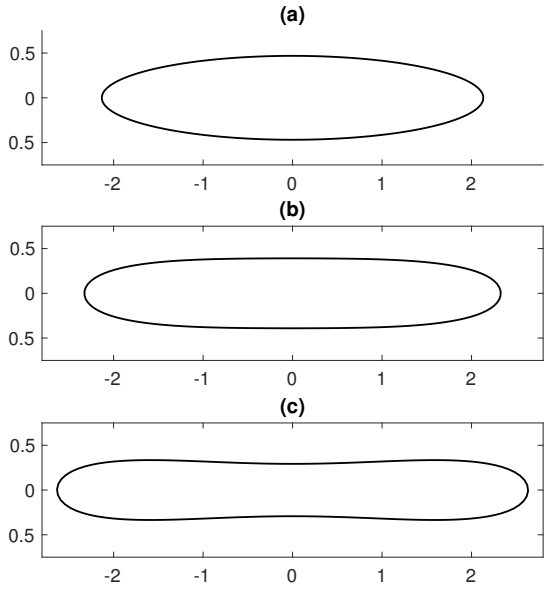

Figure 4.10: The shapes of Sadovskii vortices at the $m = 3$ bifurcation point at three different locations on the solution manifold. In (a), the vortex at the bifurcation point is shown for $\Lambda = 0.9880707955$ and $S_r = 0.0211040482$. In (b) is the vortex at $\Lambda = 0.7436277251$, $S_r = 0.0155457556$. In (c), the vortex at $\Lambda = 0.5303784699$, $S_r = 0.0119169668$.

to extend in a thin finger. As the straining field and vortex sheet become stronger (but remains in the large Λ regime), this thin finger also begins to curve. This shape is shown in Fig. 4.11(b).

As the sheet strength increases (and Λ decreases), convergence becomes more difficult. Figure 4.12(a) shows the asymmetric solution when almost half the circulation is coming from the vortex sheet. It appears the stronger vortex sheet increases the minimum width of the finger. Figure 4.12(b) shows the vortex shape near the bifurcation point where the asymmetric branch connects. As the vortex shape at the bifurcation point has a larger radius of curvature, it seems that the last converged shape we calculated also has a larger radius of curvature at the end that previously had the cusp or finger. We were able to calculate the asymmetric solutions for all the solution families that had the bifurcation point and were calculated using the vortex patch nondimensionalization. However, we

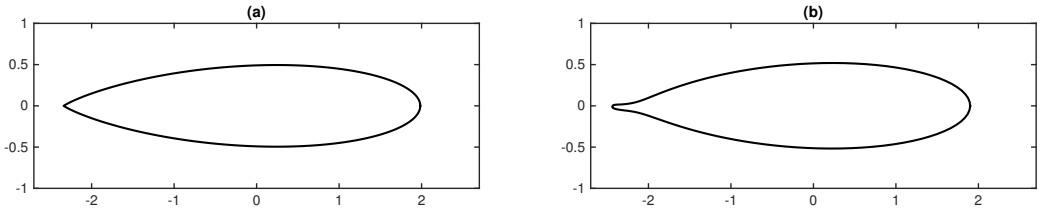

Figure 4.11: Comparison of patch and Sadovskii asymmetric shapes. In (a), the limiting shape for the patch vortex ($\Lambda = 1$) showing the cusp. This comes from the bifurcating family at $m = 3$. In (b), the last converging shape for the related bifurcating family at ($\Lambda = 0.931957, \gamma L^2/\Gamma_o = 0.0205050$). The vortex sheet forces a round shape, and in this case begins to extend the side where the cusp was. There is also a slight curve to the narrow finger that occurs where the cusp was. This curve becomes more pronounced with increasing $\gamma L^2/\Gamma_o$.

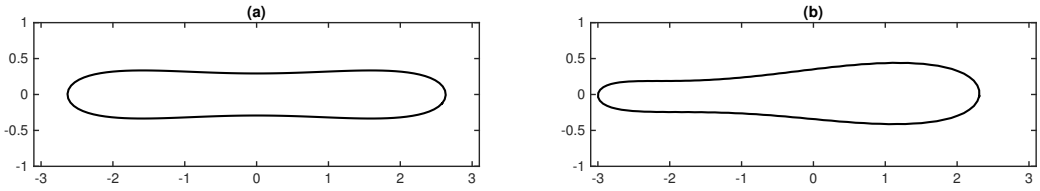

Figure 4.12: Asymmetric branch for a Sadovskii vortex. In (a), the symmetric shape at the bifurcation point ($\Lambda = 0.530378, \gamma L^2/\Gamma_o = 0.0119170$). In (b), the last converged shape for the Sadovskii vortex ($\Lambda = 0.523509, \gamma L^2/\Gamma_o = 0.0119086$) showing the asymmetry. This comes from the bifurcating family at $m = 3$.

were not able to calculate solutions on the bifurcating branch using the vortex sheet nondimensionalization. Because of this, it is not clear how far the bifurcation point exists on the family, and whether the possible bifurcation points calculated using the vortex sheet nondimensionalization are spurious or actually exist.

4.3.2 Branch at $m = 4$ to $m = 6$

As was shown in Fig. 4.6, the bifurcation point at $m = 4$ becomes a separation of two families for $\Lambda \neq 1$. This same type of separation is also seen at $m = 6$, and it seems that it occurs for larger even values of m. The family of solutions between the doubly

cusped vortices at $m = 4$ is connected to the family with two pinch off points at $m = 6$. The separation of this from the branch with two cusps and more elongated solutions is shown in Fig. 4.13. This family between $m = 4$ and $m = 6$ is shown in green in Fig. 4.14.

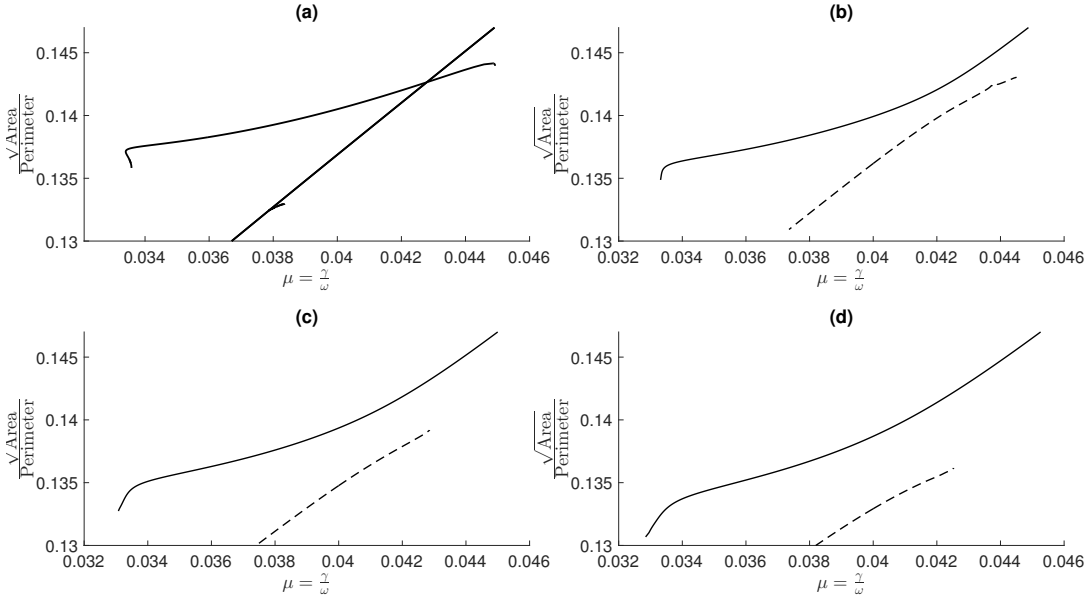

Figure 4.13: Split in Sadovskii vortex families near the $m = 6$ bifurcation point. Patch solutions with $\lambda = 0$ are shown in (a). In (b), (c), and (d), Sadovskii solutions are shown at constant values of $\lambda = 0.050586, 0.071905, 0.088796$, respectively. In (b), (c), and (d), the upper family is shown in the solid line and the more elongated family is shown by the dashed line. As λ increases, these families get farther from each other.

The behavior of the cusps is similar to the single cusp in the $m = 3$ branch. In this case, it occurs on both sides, and it doesn't appear to exhibit the slight curve shown in Fig. 4.11(b). As the sheet strength is increased, thin fingers again extend outward from where the cusps were. As the sheet continues to increase in strength, these fingers get wider at the edges, and the shape appears closely related to one with two pinch off points (see Fig. 4.16). This appears to occur as a shrinking of the manifold as the sheet strength increases. In Fig. 4.15, we show the cusped patch shape and compare it to a Sadovskii shape showing the bulging fingers on both ends.

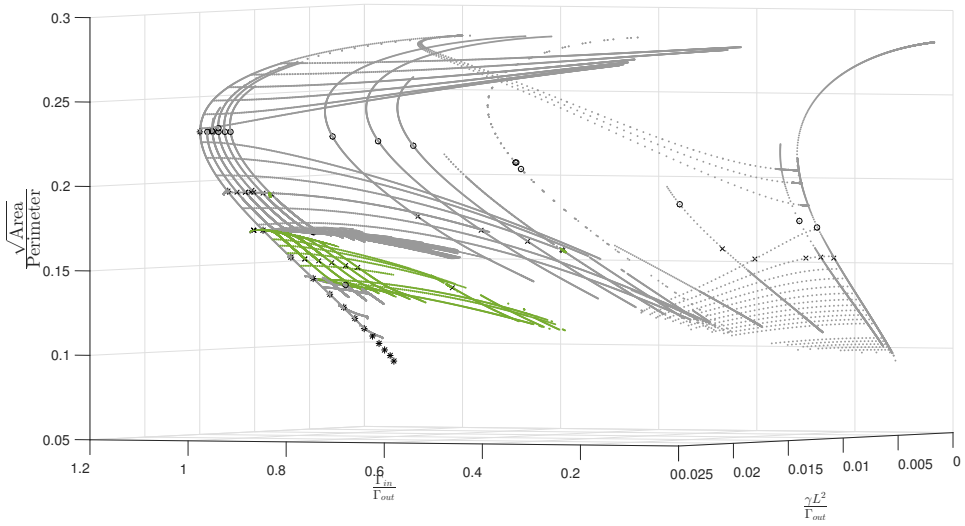

Figure 4.14: The family of Sadovskii solutions connecting the doubly cusped solutions at the $m = 4$ patch bifurcation with the solutions with two pinch off points at the $m = 6$ patch bifurcation is shown in green. All other Sadovskii solutions are shown in grey.

As Fig. 4.16 shows, as the vortex sheet strength increases, the pinch off points on the $m = 6$ branch are smoothed out much as occurs in the hollow case. No solutions for $\Lambda < 0.6$ converged for this family between $m = 4$ and $m = 6$. It is likely that this family ends at a point where the only solution is at the $m = 5$ bifurcation point.

As Λ is decreased, the shape of the vortices at the bifurcation point began to show the signature of two pinch off locations, as shown in Fig. 4.17. The two shapes, one with the two sharp ends, and one with the two pinch off points, become more similar as the vortex sheet becomes stronger. This can be seen from the shape of Fig. 4.17(b), where it is hard to say which shape this is closer to. It seems that this similarity between the two branches leads to the collapse of the manifold. Figure 4.18 shows the asymmetric shape of a vortex on the bifurcating family, at $\Lambda = 0.7645177864$, $S_r = 0.011900267630435$. One side looks like the symmetric shape in Fig. 4.17(b), while the other side looks more like the shape in Fig. 4.16(b).

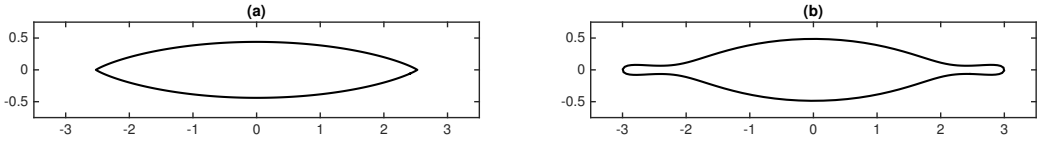

Figure 4.15: Comparison of patch and Sadovskii shapes for $m = 4$ branch. In (a), the limiting shape for the patch vortex ($\Lambda = 1, \mu = 0.060718002281533$) showing the cusps (see Fig. 2.8(d)). In (b), the last converging shape for the related bifurcating family at ($\Lambda = 0.759201712526306, \gamma L^2/\Gamma_o = 0.013255992294233$). The vortex sheet forces a round shape, which leads to the skinny fingers on each side where the cusps had been. This shape is the end of the family of solutions represented by the dashed lines in Fig. 4.6.

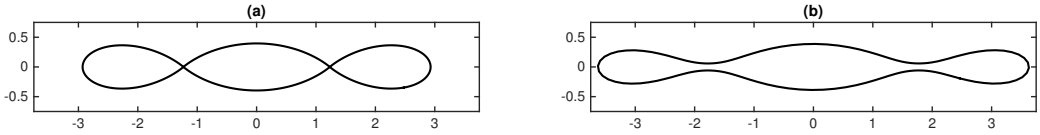

Figure 4.16: Comparison of patch and Sadovskii shapes for $m = 6$ branch. In (a), the limiting shape for the patch vortex ($\Lambda = 1, \mu = 0.033576718581039$) showing the sharp pinch points (see Fig. 2.10(c)). In (b), the last converging shape for the related bifurcating family at ($\Lambda = 0.711623862468520, \gamma L^2/\Gamma_o = 0.007754411438533$). The vortex sheet leads to pinch off points that are closer to those of the hollow vortex, or the vortex sheet alone.

4.4 Summary

In this chapter, we solved for the shape of the solution manifold for the Sadovskii vortex. In the limiting cases, the problem collapses to that of the vortex sheet and the vortex patch. These two problems have different solution families, and our numerical continuation shows the relationship between these solution families. At bifurcation points for even values of m, the solution manifold separates in the presence of any vortex sheet. However, the bifurcation points at odd values of m remain attached to the families, and

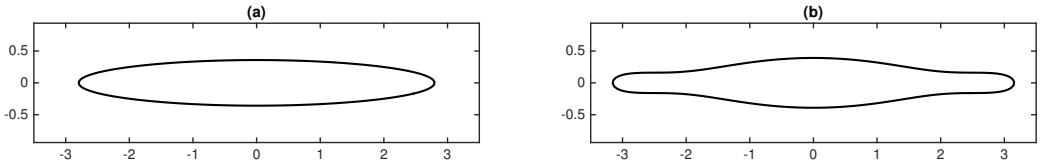

Figure 4.17: Sadovskii vortex shapes at $m = 5$ bifurcation points. In (a), the shape at $\Lambda = 0.9806992343$, $S_r = 0.0152156494$. In (b), the shape at $\Lambda = 0.7678296326$, $S_r = 0.0113405546$.

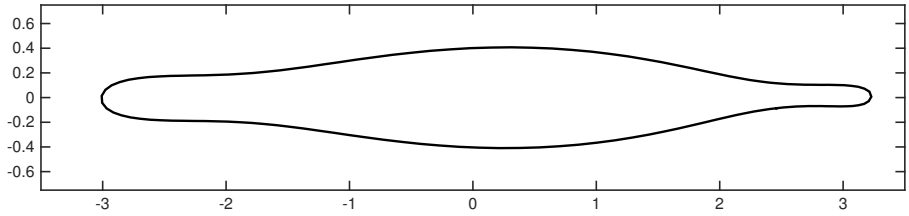

Figure 4.18: Sadovskii vortex asymmetric shape at the $m = 5$ bifurcation point, with $\Lambda = 0.7645177864$, $S_r = 0.011900267630435$. One side of this asymmetric vortex looks like the shape on the symmetric family, while the other side is narrower. Compare this to the patch shape in Fig. 2.9(b).

these asymmetric solutions are shown to exist over a wide range of the parameter space.

The separation of families at even values of m explains the difference between the vortex sheet and vortex patch families. While the vortex patch family includes many bifurcation points and bifurcating families, as well as their associated shapes, the vortex sheet family is a single solution family that goes from the circular vortex to a shape with a single stretched pinch off point. The vortex patch families that exist below the $m = 4$ bifurcation point are completely disconnected from this family for all $\Lambda < 1$. All of these more elongated families that are farther from the circular regime appear to exist only for smaller ranges of $1 \geq \Lambda > 0$, which is why they do not appear on the vortex sheet bifurcation diagram.

We demonstrated that as the vortex sheet strength is increased from the patch solutions, the vortex shapes become smoother. Stronger vortex sheets seem to require smoother shapes with high radii of curvature. In the case of families below the first even bifurcation point, the effect of the vortex sheet seems to limit the family's existence to larger values of Λ.

Chapter 4 is currently being prepared for submission for publication. Freilich, Daniel; Llewellyn Smith, Stefan. "The Sadovskii Vortex in Strain". The dissertation author was the primary investigator and author of this material.

Chapter 5

Surface Tension

In this chapter, we consider the Sadovskii vortex with surface tension. This allows an over-pressure inside the vortex, which leads to a new term in the dynamic condition on the vortex sheet. We study the effect of surface tension on the vortex patch, vortex sheet, and a Sadovskii vortex family near $\Lambda = 0.5$. In the case of the vortex patch, the addition of surface tension is shown to significantly affect the shape of the steady vortices, and leads to a smaller solution manifold than in the case with no surface tension. In the case of the sheet vortex, the addition of surface tension has less noticeable effects. The Sadovskii vortex shows a response that falls between the patch and sheet cases.

Problem Formulation

Previous work has shown that surface tension affects the stability of flows with an interface between two fluids, such as Baker et al. (1982), Pullin (1982), McLean and Saffman (1981), Hou et al. (1997), Rangel and Sirignano (1988), and Nie (2001). Since interfaces between two fluids tend to be susceptible to Kelvin-Helmholtz instabilities, we are interested in the effect of surface tension on steady states of Sadovskii vortices. These steady states can then be used in future investigations into the stability of Sadovskii

vortices, and whether surface tension can stabilize any of the more deformed shapes.

The governing equations for the surface tension case are very similar to the previously discussed Sadovskii case (see Chapter 4). In this case, the interior of the vortex has constant vorticity as before, so we must solve Poisson's equation

$$\nabla^2\Psi = -\omega \tag{5.1}$$

inside the vortex. Outside the vortex, the flow is irrotational, so the stream function satisfies Laplace's equation

$$\nabla^2\Psi = 0. \tag{5.2}$$

The exterior flow field is again a straining field, so the stream function far from the vortex looks like strain with a point vortex at the origin,

$$\Psi \sim \gamma\left(x^2 - y^2\right) - \frac{\Gamma}{2\pi}\ln|z| \quad \text{as} \quad |z| \to \infty, \tag{5.3}$$

where γ is related to the strength of the straining field and Γ is the circulation of any contour that surrounds the vortex. Since the boundary of the vortex is a streamline, Ψ is constant on the vortex boundary, and we use the degree of freedom in the choice of stream function to set $\Psi = 0$ on the vortex boundary.

The final boundary condition for the Sadovskii vortex is the Bernoulli-type dynamic condition,

$$\frac{\rho_{out}}{2}\left|\mathbf{U}_{T(out)}\right|^2 - \frac{\rho_{in}}{2}\left|\mathbf{U}_{T(in)}\right|^2 = Q + \sigma\kappa_c, \tag{5.4}$$

where ρ_{out} is the density outside the vortex, ρ_{in} is the density in the vortex core, $\mathbf{U}_{T(in)}$ is the total velocity on the inside edge of the boundary, $\mathbf{U}_{T(out)}$ is the total velocity on the outside edge of the boundary, σ is the strength of the surface tension, and κ_c is the

curvature of the boundary. The curvature can also be thought of as $1/R$, where R is the radius of curvature of the boundary. This is the Laplace-Young boundary condition, which (in two dimensions) is usually written as

$$[p]_2^1 = \sigma\kappa_c, \tag{5.5}$$

where $[p]$ is the pressure difference across the interface, and σ and κ_c are defined as above. In Eq. 5.5, σ is always positive, and side 1 is the interior of the vortex. If $\kappa_c > 0$, the center of curvature is inside the vortex and the over-pressure will be inside the vortex. If $\kappa_c < 0$, the center of curvature is outside the vortex (for instance, where a pinch off begins to occur in the patch and sheet cases), and the over-pressure will be on the outside of the vortex.

In the case where $\sigma = 0$, there is no surface tension, and the equations revert back to the previously investigated Sadovskii boundary conditions. With the inclusion of surface tension, the available parameter space is increased by another dimension. Because of these complexities, we will focus on the effect surface tension has on the sheet case, the patch case, and finally a middle Sadovskii case near $\Gamma_{in}/\Gamma_{out} \approx 0.5$.

Solution Method

From Eq. 5.4, it is clear that surface tension can be thought of as a vortex sheet that varies in strength depending on the curvature of the boundary. This means that even in the vortex patch case, adding surface tension requires the calculation of a vortex sheet, since the surface tension leads to a discontinuity in velocity. Because of this, we use the inverse velocity method to solve for the steady states of these vortices with surface tension. This allows us to discretize the points based on the inverse velocity, and then calculate the location of the boundary and the vortex sheet strength along the boundary.

In fact, the only modification to the inverse velocity method used for the Sadovskii vortex in Chapter 4 required to solve the surface tension problem is to add the $\sigma\kappa_c$ term to the dynamic boundary condition. We calculate the curvature from

$$\kappa_c = \frac{x'y'' - y'x''}{[(x')^2 + (y')^2]^{3/2}}. \tag{5.6}$$

We again use different nondimensionalizations depending on the vortex regime, particularly if we are close to the vortex sheet solutions.

5.1 Patch vortex with surface tension

When surface tension is added to the vortex patch, the governing equations and method remain the same as in Chapter 2, except for the dynamic (Bernoulli) condition. It has the new surface tension term, and becomes

$$\left|\mathbf{U}_{T(out)}\right|^2 - \rho\left|\mathbf{U}_{T(in)}\right|^2 = \frac{2\sigma\kappa_c}{\rho_{out}}. \tag{5.7}$$

The surface tension term leads to a discontinuity in velocity, and therefore the existence of a vortex sheet when $\sigma \neq 0$. This requires the solution method to include the existence of both a vortex patch and vortex sheet, and so it is similar to that used to calculate the Sadovskii vortex solutions in Chapter 4. Since the nondimensionalization is the same as previously (see Eq. 4.18), the new surface tension term is nondimensionalized by

$$\kappa_c = \frac{\kappa_c^*}{L} \quad \text{and} \quad \sigma = \omega^2 L^3 \rho_{out} \sigma^*. \tag{5.8}$$

When $\sigma = 0$, this equation reverts back to the patch case solved for in Chapter 2. We performed numerical continuation in both σ and μ to investigate the behavior of the patch

vortices with surface tension.

Figure 5.1 shows the vortex patch family and the points used for continuation in σ. These points are chosen to study the behavior of the solutions between the circular solutions and the $m = 5$ bifurcation point.

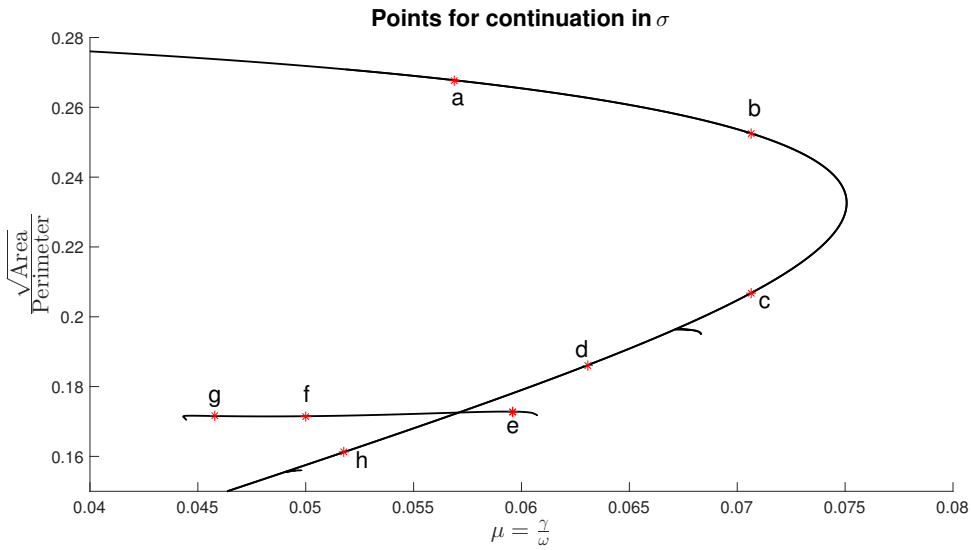

Figure 5.1: Points used for continuation in σ, beginning with patch vortices. These points are shown by the red stars, while the black lines show the patch solutions.

These continuations in σ showed two basic behaviors. In some places, the continuation in σ arced between two sections of the same family. This was seen at continuation in σ from b and c, and also between some parts of the bifurcating branches at $m = 4$ and some parts of the elliptical family (e,f, and h). The form of solution manifold appears to be different from that in the Sadovskii case. When continuing in σ, less of the vortex patch family exists than for continuation in λ.

With surface tension, the shape of the solution manifold of each family is similar, although the extent of each family into σ is different. The first family, closest to the circle (point a), continues to exist for the largest values of σ. The next family with similar shape, going between the branch with a single pinch off point and the more elongated ellipses below it (points b and c), exists for the next largest values of σ. The family

between $m = 3$ and $m = 4$ (point d) does not exist for much surface tension. Continuation in σ beginning on the $m = 3$ branch calculated no solutions for $\sigma > 0$.

The shapes for vortices above $m = 3$ with surface tension are shown in Figs. 5.2-5.5. These shapes were calculated by continuation in σ from point a in Fig. 5.1, with $\mu = 0.056888$. Figure 5.2 shows a vortex with negligible surface tension. On the left is a plot of the vortex shape, with the black star indicating the location of the first point. On the right is a plot of both the vortex sheet strength κ (dotted line, right scale) and the curvature κ_c (solid line, left scale). The curvature of the shape is entirely positive, and the vortex sheet strength is negligible.

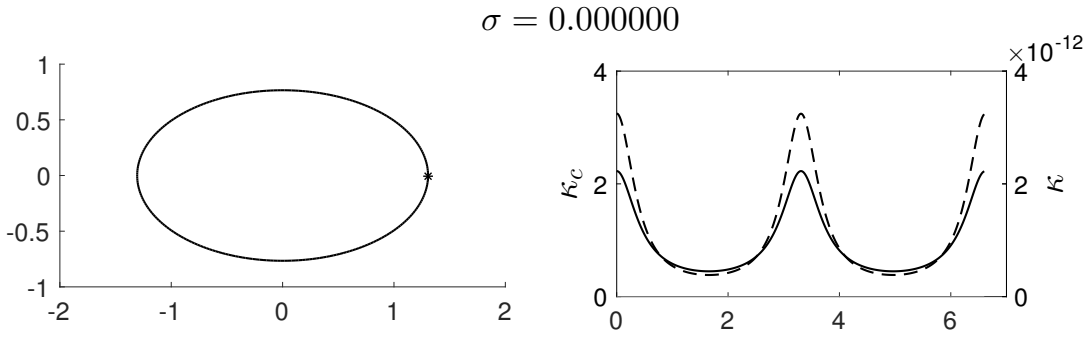

Figure 5.2: A plot of the vortex shape and the vortex sheet strength (κ) and the curvature (κ_c) at $\mu = 0.056888$. The black star on the shape indicates the location of the first point. In the plot on the right, the x-axis is arclength. κ_c is the solid line, with the scale on the left side, and κ is the dashed line, with the scale on the right (note that the vortex sheet strength is negligible). The grey line shows $\kappa_c = 0$ for reference. This shape was computed with 256 points.

As the surface tension is increased, small sections of the vortex boundary gain negative curvature. These areas, near the corners of the vortex, seem to be symmetric, and occur on the side of the vortex where the straining field flow would be into the vortex. This can be seen in Fig. 5.3, shown by the red portions of the vortex boundary. The curvature is larger, and the vortex sheet is also stronger. The vortex sheet has a similar shape to the curvature, which is expected from the the relationship between these two quantities.

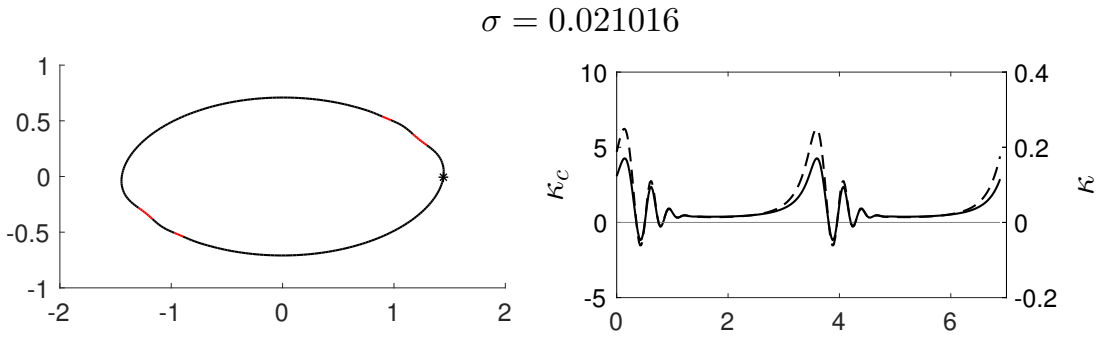

Figure 5.3: A plot of the vortex shape and the vortex sheet strength (κ) and the curvature (κ_c) at $\mu = 0.056888$, $\sigma = 0.021016$. The black star on the shape indicates the location of the first point, while red lines show places on the vortex boundary where the curvature is negative. In the plot on the right, the x-axis is arclength. κ_c is the solid line, with the scale on the left side, and κ is the dashed line, with the scale on the right. The grey line shows $\kappa_c = 0$ for reference. This shape was computed with 256 points.

Figures 5.4 and 5.5 show the vortices as the surface tension continues to increase in strength. While Fig. 5.3 had two sections of negative curvature on each side, the increased surface tension leads to a third section of negative curvature. The curvature and vortex sheet strength continue to increase, although the basic shape of each of them seem to stay the same. These wavy vortex shapes are similar to that seen by Tanveer (1986) in

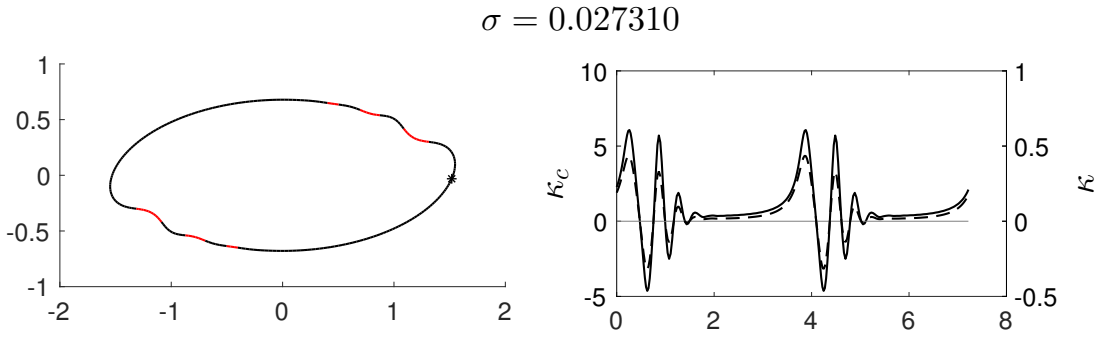

Figure 5.4: A plot of the vortex shape and the vortex sheet strength (κ) and the curvature (κ_c) at $\mu = 0.056888$, $\sigma = 0.027310$. The black star on the shape indicates the location of the first point, while red lines show places on the vortex boundary where the curvature is negative. In the plot on the right, the x-axis is arclength. κ_c is the solid line, with the scale on the left side, and κ is the dashed line, with the scale on the right. The grey line shows $\kappa_c = 0$ for reference. This shape was computed with 256 points.

calculations of Hele-Shaw bubbles. In that paper, Tanveer found the existence of multiple

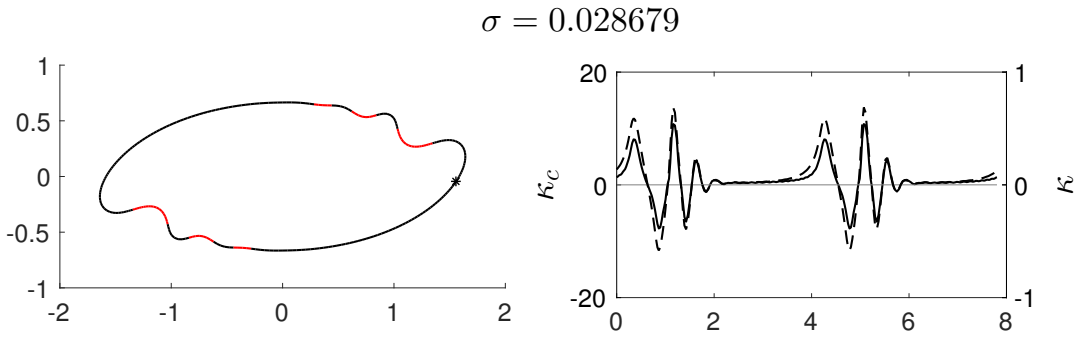

Figure 5.5: A plot of the vortex shape and the vortex sheet strength (κ) and the curvature (κ_c) at $\mu = 0.056888$, $\sigma = 0.028679$. The black star on the shape indicates the location of the first point, while red lines show places on the vortex boundary where the curvature is negative. In the plot on the right, the x-axis is arclength. κ_c is the solid line, with the scale on the left side, and κ is the dashed line, with the scale on the right. The grey line shows $\kappa_c = 0$ for reference. This shape was computed with 256 points.

solutions. He called the more elongated branch, which has the similar oscillations, the "extraordinary solution branch." In both cases the external velocity is in the same direction in relation to the location of these waves (see Fig. 5.6 for the straining field shape). These waves appear on the side of the vortex where the straining field flow is towards the vortex. However, they do not appear where the straining field flow is away from the vortex, as can be seen in Figs. 5.3-5.5.

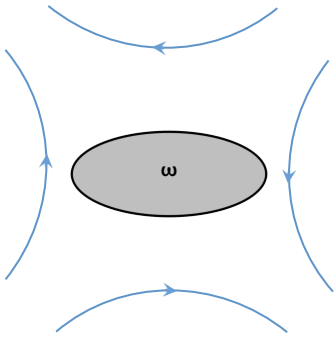

Figure 5.6: Schematic representation of the the Sadovskii vortex in strain with surface tension. The vortex patch is shown in grey, while the vortex sheet (due to the jump in the Bernoulli constant) is shown as the black line. The blue lines show the straining field, with arrows showing the flow direction from the straining field.

Continuation in μ shows that for small values of σ, the bifurcation point at

$m = 3$ remains on the family, and its location is calculated as the continuation crosses it. Solutions at smaller values of σ were computed with 256 points, starting from a σ continuation between the $m = 3$ and $m = 4$ bifurcation points (see blue lines in Fig. 5.7). Continuation at larger values of σ, also using 256 points, did not pass through the bifurcation point at $m = 3$. It seems that as σ increases, the bottom edge of the solution manifold for this family passes through the bifurcation point, at which point the family has no bifurcations. As the figure shows, stronger surface tension reduces the solution manifold extent in S_r. For large enough values of surface tension, we expect the limiting shape to be the same as the last shape in Fig. 5.5.

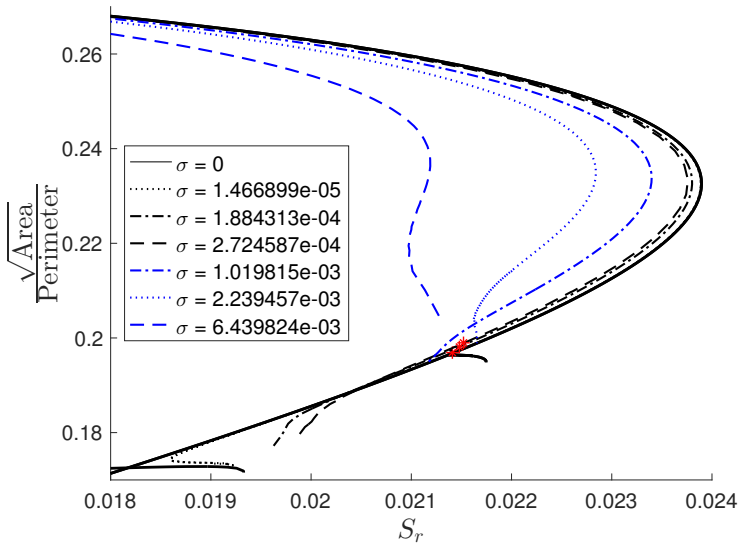

Figure 5.7: Overview of continuations in μ for different values of σ. The black dotted/dashed lines were computed with 256 points, and go past the $m = 3$ bifurcation point. These families have the bifurcation point at $m = 3$, shown by the red stars. The blue lines were also computed using 256 points, and do not pass the bifurcation point.

While we don't see the appearance of waves for all values of surface tension, the first indent near the corner does occur for other parts of this family. Using 256 points, we show the last converged shape in these families, near where the $m = 3$ bifurcation point would be, in Fig. 5.8. For small values of surface tension, the sharp corner seems to

cause a small section of negative curvature. As the surface tension increases, this feature grows, and a second wave appears on the surface. This vortex begins to look like the vortex in 5.5.

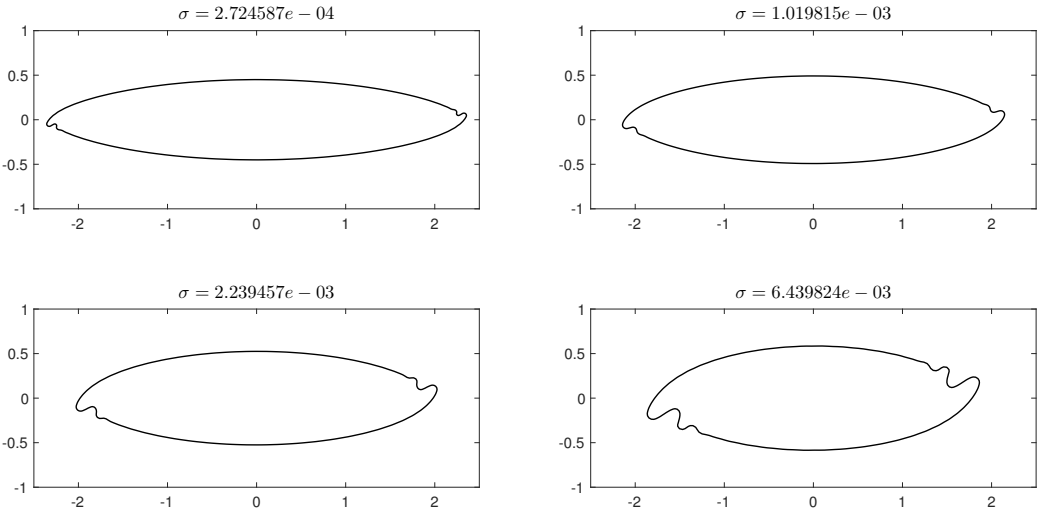

Figure 5.8: Last converged vortices near $m = 3$ bifurcation point. These shapes are calculated using 256 points. As the surface tension increases, the features become larger, and begin to look similar to the wavy vortices in Fig. 5.5.

$m = 4$ and below

Continuation in σ again seemed to show the same basic behaviors, with continuation where $\mu < \mu_5$ extending farther in σ, and those families that started at $\mu > \mu_5$ bridging between the elliptical family and the family with the pinch off (where μ_5 is the value of μ at the $m = 5$ bifurcation point). Figures 5.9-5.11 show shapes for continuation in σ beginning on the $m = 4$ family of vortex patches with a pinch off. As the surface tension increases, it smooths out the pinch off, while simultaneously increasing the curvature at the edges of the vortex shape (compare Figs. 5.9 and 5.10).

As σ continues to increase, the curvature in the corners continues to increase. This is accompanied by an area of negative curvature. This shape is shown in Fig. 5.11.

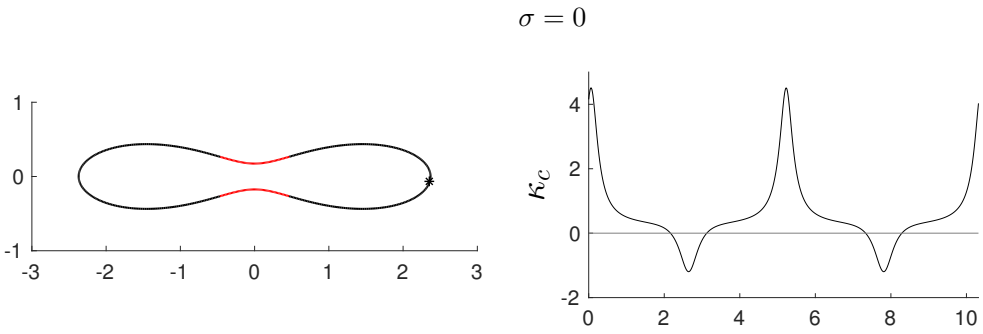

Figure 5.9: A plot of the vortex shape and the curvature (κ_c) at $\mu = 0.0458059$ for the vortex with no surface tension. The black star on the shape indicates the location of the first point, while red lines show places on the vortex boundary where the curvature is negative. In the plot on the right, the x-axis is arclength. κ_c is the solid line, with the scale on the left side. The grey line shows $\kappa_c = 0$ for reference. This shape was computed with 128 points.

Continuation in μ overall seemed to follow the trend seen in the other family, with the manifold for shapes with surface tension generally ending above the $m = 5$ bifurcation point. However, the continuation with the smallest value of σ continued below $m = 5$. These families of μ continuation are shown in Fig. 5.12. The solid black lines show the patch families, and the dotted and dashed lines show continuation at different values of σ.

Figure 5.13a shows the last converged value for the μ continuations shown in Fig. 5.12. Although the first shape appears to be below the $m = 5$ bifurcation, the shape appears to be in the same family as those shapes shown at larger values of the surface tension. As before, there is an area of negative curvature that develops near the corners. It seems to be sharper for smaller values of σ, which makes sense since the vortex sheet strength is closely related to the value of $\sigma\kappa_c$, and so becomes stronger as the surface tension increases. As we saw in the Sadovskii vortices, a stronger vortex sheet leads to wider and more rounded features.

The end of the family with small μ seems to maintain its shape in μ and the shape parameter. However, the vortex sheet affects what happens near the vortex pinch

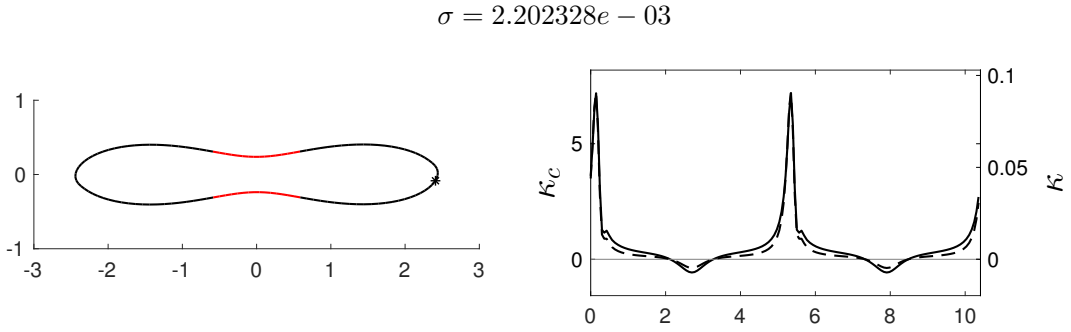

Figure 5.10: A plot of the vortex shape and the vortex sheet strength (κ) and the curvature (κ_c) at $\mu = 0.0458059$. The black star on the shape indicates the location of the first point, while red lines show places on the vortex boundary where the curvature is negative. In the plot on the right, the x-axis is arclength. κ_c is the solid line, with the scale on the left side, and κ is the dashed line, with the scale on the right. The grey line shows $\kappa_c = \kappa = 0$ for reference. The surface tension has smoothed out the pinch off point and increased the curvature at the corners. This shape was computed with 128 points.

off, shown in Fig. 5.13b. Just before pinch off, the area at the pinch point develops an indentation that seems to be similar to those seen at the outside edges of the previous vortices. As the surface tension increases and the vortex sheet gets stronger at the pinch point, this deformation occurs when the vortex is wider. It is interesting that the addition of surface tension seems to desingularize the cusp that had previously existed at the pinch off point.

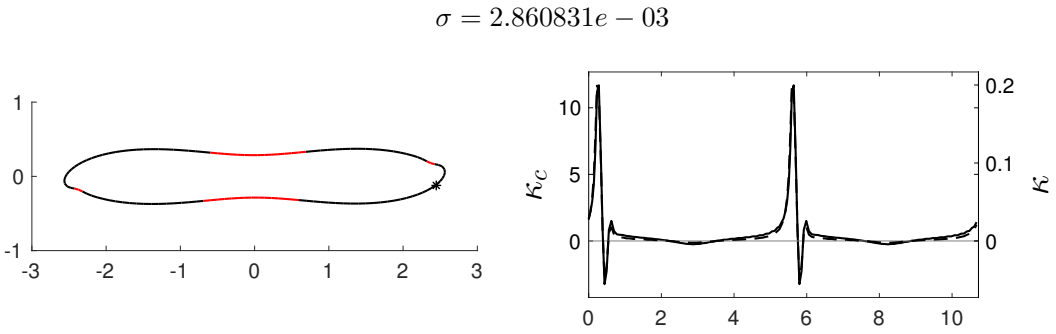

Figure 5.11: A plot of the vortex shape and the vortex sheet strength (κ) and the curvature (κ_c) at $\mu = 0.0458059$. The black star on the shape indicates the location of the first point, while red lines show places on the vortex boundary where the curvature is negative. In the plot on the right, the x-axis is arclength. κ_c is the solid line, with the scale on the left side, and κ is the dashed line, with the scale on the right. The grey line shows $\kappa_c = \kappa = 0$ for reference. The increased surface tension has caused an area of negative curvature near the corners. This shape was computed with 128 points.

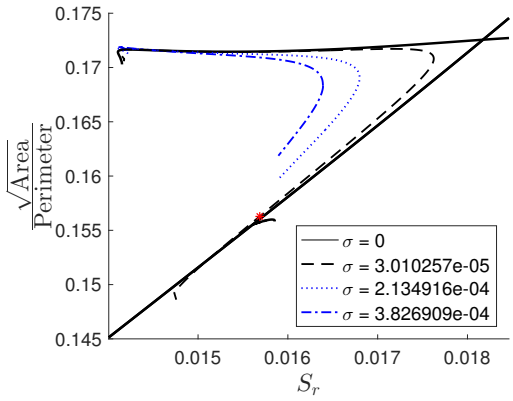

Figure 5.12: Plots of different continuations in μ for various values of σ near the $m = 4$ bifurcation point. The black dashed line goes past the $m = 5$ bifurcation point, and has a bifurcation point indicated by the red star. The blue dotted/dashed lines do not pass the bifurcation point at $m = 5$. For solutions at higher values of S_r and the shape parameter, see Fig. 5.7.

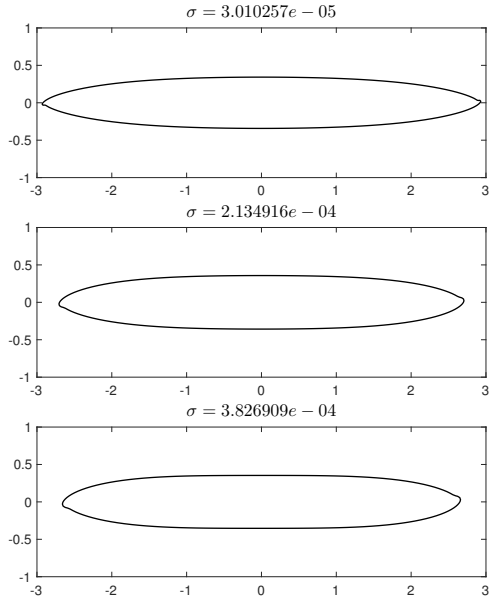

(a) Last converged vortex shapes at different values of σ, showing what happens at the edges when they become sharp.

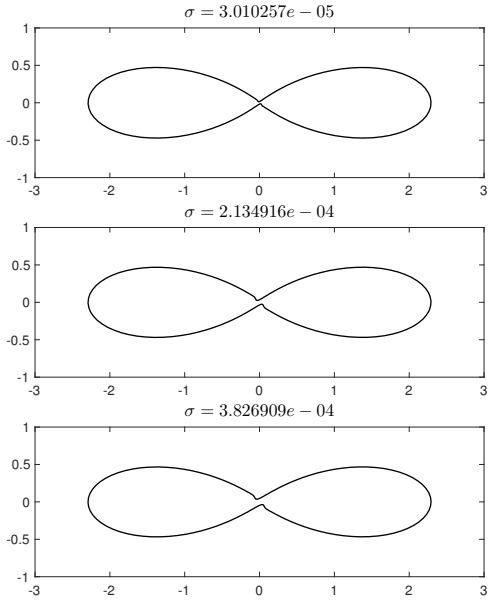

(b) Last converged vortex shapes at different values of σ, showing what happens at the side that previously showed pinch off.

Figure 5.13: Last converged shapes with surface tension along the $m = 4$ bifurcating families.

5.2 Sheet vortex with surface tension

When surface tension is added to the vortex sheet, the governing equations remain the same as in Chapter 3, except for the dynamic condition. It has the surface tension term, and becomes

$$\left|\mathbf{U}_{T(out)}\right|^2 - \rho\left|\mathbf{U}_{T(in)}\right|^2 = \lambda_s^{-2} + 2\sigma\kappa_c. \tag{5.9}$$

The nondimensionalization is the same as previously (see Eq. 3.11), the new surface tension term is nondimensionalized by

$$\kappa_c = \frac{\kappa_c^*}{L} \quad \text{and} \quad \sigma = q^2 L\sigma^*. \tag{5.10}$$

The vortex sheet solutions with surface tensions show some similar characteristics to the vortex patch solutions. However, since the basic family is simpler, the shapes with surface tension are less deformed. This could be partly attributed to the fact that these solutions are beginning with a vortex sheet, and the surface tension is just altering the strength of the vortex sheet, whereas for the vortex patch the surface tension is adding a different type of vorticity.

Figure 5.14 shows the results of some continuation in λ_s at different values of σ. As in the vortex patch case, for small values of the surface tension, the families continue past the bifurcation point. For larger values of σ, the families do not pass the bifurcation point.

Figure 5.15 shows the shapes of the last converged vortices for different values of σ. As the surface tension is increased, the vortices become wider, no longer allowing the pinched off shape that was the end of the family with no surface tension. These vortices also begin to exhibit the same deformation as those from the vortex patch did, with a flattening near the corner leading to some waves as the surface tension is increased. Also,

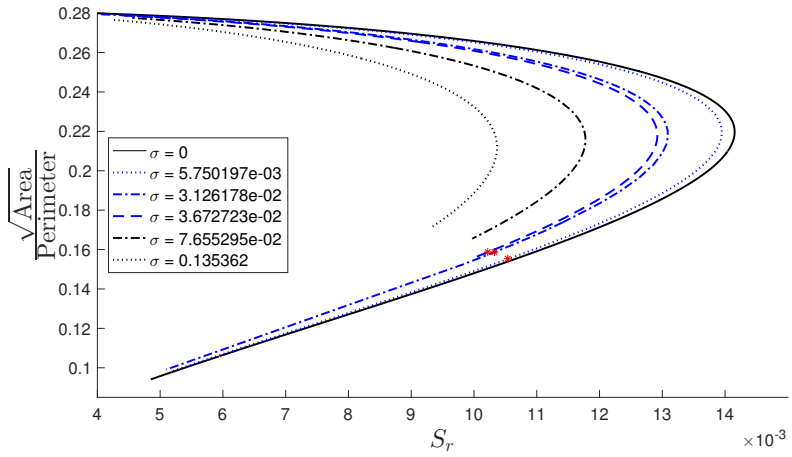

Figure 5.14: Overview of hollow vortex continuations in λ_s for different values of σ. The blue lines show families that have a possible bifurcation point (red stars), while the black lines show families that have no bifurcation points. These solutions were computed with 256 points.

as the surface tension is increased, the large portion of the sheet vortex where there is negative curvature seems to become impossible, and the only portions with negative curvature are much smaller.

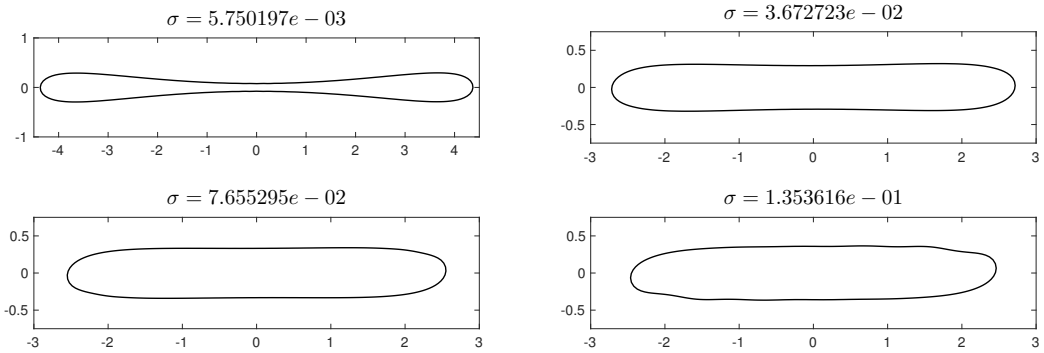

Figure 5.15: Last converged shapes for different values of σ. The top left shape is shown with different axes from the other three, since it is much longer in the x direction. These solutions were computed with 256 points.

5.3 Sadovskii vortices with surface tension

We chose a family of Sadovskii vortices near $\Lambda = 0.5$ to look at the effect of surface tension, and used the vortex patch nondimensionalization. The starting solutions have non-constant values of Λ, since the continuation variable used for the starting parameters was μ. These initial Sadovskii vortices without surface tension are highlighted in Fig. 5.16.

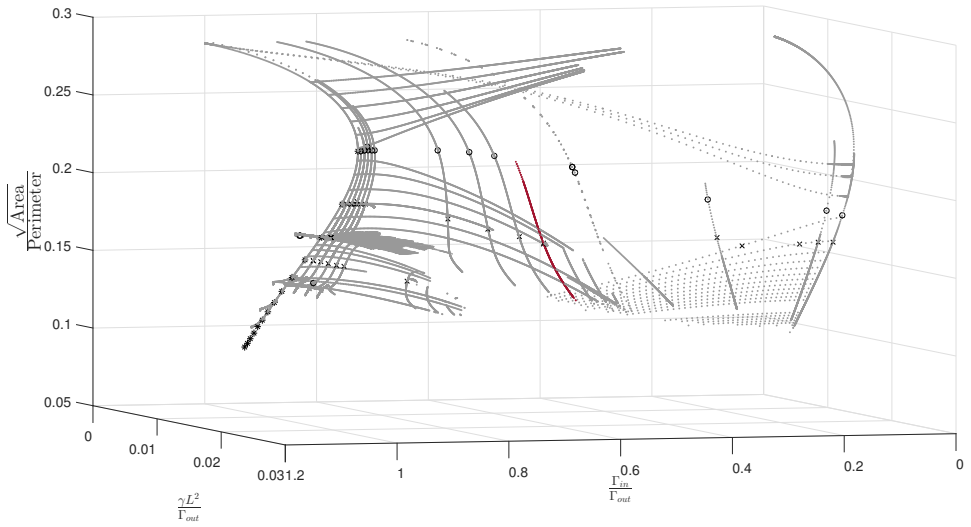

Figure 5.16: Family of Sadovskii vortex solutions used as a initial solutions for the addition of surface tension.

Figure 5.17 shows the continuations in μ at different values of σ. The black line shows the starting family for these solutions. This family, although plotted in S_r, does not have a constant value of Λ; instead, it has constant values of $\lambda = q/\omega L$. The blue lines show continuations that were begun from a solution in σ near the top, while the green lines show continuations from a solution near the bottom. The red star indicates the bifurcation point that was calculated on one of the runs. The other solutions had no bifurcation points.

Figure 5.18 shows the last converged shapes for the black and blue lines in

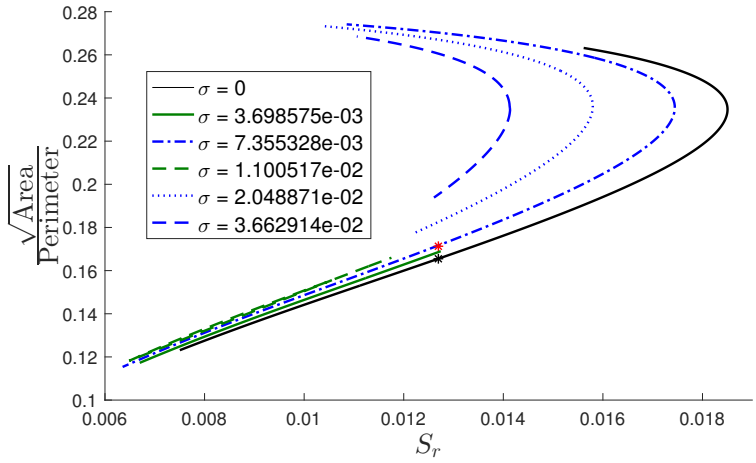

Figure 5.17: Overview of Sadovskii vortex continuations in μ for different values of σ. The blue lines show families with $\sigma \neq 0$, with continuation beginning near the top. The red star shows a bifurcation point on a surface tension solution. The green lines show solutions continued from the bottom. The black line shows the starting solutions of Sadovskii vortices with $\sigma = 0$. These solutions were computed with 256 points.

Fig. 5.17. The top row shows the plots for smaller values of σ, where the solutions crossed the bifurcation point. These vortices show the characteristic pinch off, and it is clear from the shape of the pinch off that the vortex includes both the vortex sheet and vortex patch. The plot on the top right shows a solution closer to pinch off because it was computed with twice as many points as the one on the top left. The two plots in the second row show the last converged solutions for lines that did not cross the bifurcation point. The scales in these two plots are different from the scale in the first row, as these two are wider in y and smaller in x. As can be seen, the surface tension causes the same flattening in the corners as was noted in both the vortex patch and vortex sheet cases, and for a strong enough surface tension the double wave is clear. These vortices have a stronger vortex sheet, and they have a similar shape to the vortex patch solutions, although with wider features, which seems to be the general effect of the vortex sheet.

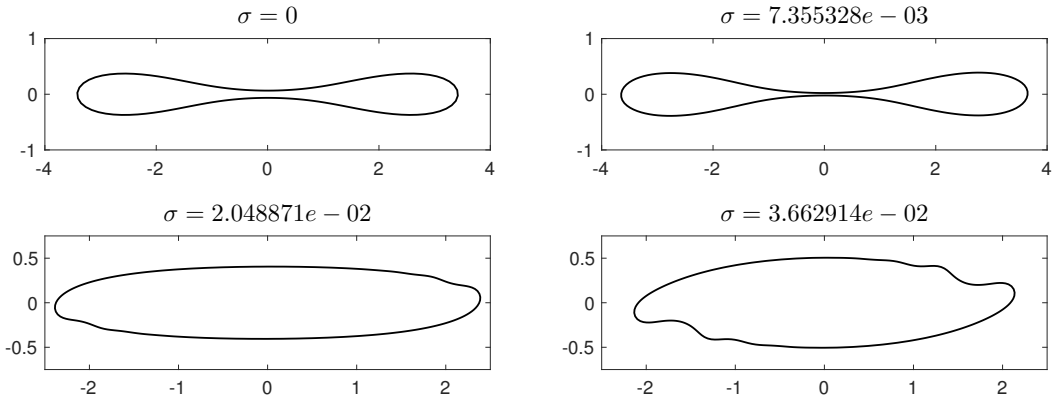

Figure 5.18: Last converged solutions for Sadovskii vortices with surface tension, beginning with more round shapes. These correspond to the last converged solutions for the black and blue lines in Fig. 5.17. Note the difference in scales between the top two and bottom two plots. The top two have smaller values of σ, and pass the bifurcation point. The bottom two have larger values of σ, and do not cross the bifurcation point. The top left plot was computed with 128 points, while the other solutions were computed with 256 points.

5.4 Summary

In this chapter, we showed that the addition of surface tension to the vortex patch, sheet, and Sadovskii shapes causes some deformations. In the patch case, these deformations appeared as a double wave, and the strength of the surface tension seemed to affect the curvature of the boundary oscillations. These oscillations were similar to the "extraordinary" solution branch in a Hele-Shaw cell in Tanveer (1986). Where there had previously been a pinch off on the $m = 4$ branch, the cusp at the pinch point was desingularized, and the interaction between the two sides is greater for stronger surface tension. While vortex patch solutions exist past the bifurcation point at $m = 3$ for small values of the surface tension parameter σ, as the surface tension increases, the solution manifold becomes smaller and does not appear to pass through the bifurcation point.

In the sheet case, there were less visible effects from the surface tension. However, the addition of surface tension led to some deformations where the straining field flow was into the vortex, similar to those seen in the patch case. The deformations in the

Sadovskii case were not as severe as those in the patch case, but were more noticeable than in the sheet case. They again looked similar to the deformations seen in the vortex patch case.

Chapter 5 is currently being prepared for submission for publication. Freilich, Daniel; Llewellyn Smith, Stefan. “The Sadovskii Vortex in Strain with Surface Tension”. The dissertation author was the primary investigator and author of this material.

Chapter 6

Conclusions

In this work, we used the vortex patch and vortex sheet models to investigate the steady shapes of Sadovskii vortices in strain. Using numerical continuation, we were able to trace the solution manifold in $\Lambda = \Gamma_{in}/\Gamma_{out}$ and $S_r = \gamma L^2/\Gamma_{out}$. The limiting cases of the Sadovskii vortex are the vortex patch and vortex sheet, with solutions that had been previously studied. Our method recovered the previously known solutions.

For vortex patches, we used small perturbations to study the families that bifurcate from the elliptical solutions. The calculated vortex shapes were similar to those in Kamm (1987). Some of these families extended farther than Kamm was able to calculate. Bifurcating families at higher m values were found to have more pinch offs, and each bifurcating family follows a pattern. Every other bifurcation point leads to an asymmetric vortex shape that extends only into larger values of S_r. The other bifurcation points lead to families that extend in both directions along S_r, and either have a pinch off or a sharp cusp at either end.

For vortex sheets, our shapes matched with the previously known analytical solutions. We found a possible bifurcation point, but were unable to successfully calculate any possible shapes on the bifurcating family. This possible bifurcation point is interesting,

because it seems to be in a location near where we might expect the $m = 3$ asymmetric family to exist. In the Sadovskii case, this bifurcating family remained accessible using the vortex patch nondimensionalization, so it's not clear if the bifurcation actually ends somewhere on the manifold or if our current calculations have just been unable to access the family using the vortex sheet nondimensionalization.

In the case of the Sadovskii vortex, we were able to calculate the solution manifold in the parameter space. The addition of the vortex sheet to the vortex patch solutions immediately leads to a split in the solution manifold at bifurcation points for even values of m. It is this splitting of the families that leads to the much simpler solution branch for the vortex sheet. The more circular vortex patch solutions remain connected to the family with a single pinch off at $m = 4$, while becoming disconnected from the more elongated elliptical solutions and the family with cusps at both ends.

The addition of the vortex sheet to the vortex patch smooths out the sharp features. As the vortex sheet strength is increased, the radius of curvature also increases, so features such as fingers become wider and less pronounced. This also seemed to lead to a shrinking of the solution manifold, as the more deformed shapes do not seem to exist for strong enough vortex sheet strengths. It also seems that the more elongated families that exist below the $m = 4$ family only exist for small values of the vortex sheet strength, which explains why they do not appear as vortex sheet solutions.

We also added surface tension to the problem, and calculated the vortex shapes for vortex patches, vortex sheets, and selected Sadovskii vortices in the presence of surface tension. Surface tension leads to areas of negative curvature near the corners of vortex shapes, in areas where the background straining field flow is into the vortex. This leads to oscillations on the surface of the vortices, and these oscillations appear similar to those calculated on the "extraordinary branch" in Tanveer (1986). In the case of the vortex patch, the addition of surface tension also removed the cusp at the pinch off point

on the $m = 4$ branch.

In the case of the vortex sheet, surface tension had a less noticeable effect, although it still led to deformations near the edges of the vortices, at locations where the straining field flow was into the vortex. The Sadovskii vortices with surface tension were a mix between the vortex sheet and vortex patch effects, showing deformations that were more pronounced than the vortex sheet but less pronounced than the vortex patch.

The addition of surface tension was also found to limit the solution manifolds in all cases. For small values of surface tension, the solution manifold maintained its basic shape, but for larger values, there were was a much smaller range of possible solutions. The solutions that do exist seem to be less elongated, and have larger values of the shape parameter.

Future directions

We have shown that this method successfully calculates the known vortex shapes, and is also able to calculate the shapes for previously unknown situations. This method will be useful in the future, as it can be used to validate new solutions to any type of Sadovskii vortex problem. For instance, it can provide an independent way to verify the steady states of vortices found through new analytical methods, or calculated by other means.

Although the calculations in this work have been irrotational outside the vortex, this method can also be used in known rotational background flows. In the inverse velocity method, this is simple to do, since the known rotational flow is superimposed on the calculated velocity due to the vortex. In the case of the boundary element type method, this is done by separating the rotational and irrotational flows, so that the velocity the method solves for is irrotational. Preliminary testing of this method in a shear flow has provided some interesting and useful results.

In the future, it is important to investigate the stability of the steady solutions we have calculated. This will be particularly interesting in the presence of surface tension, as it may serve to eliminate the susceptibility to Kelvin-Helmholtz instability.

Appendix A

Continuation Methods

Throughout this dissertation, it was necessary to carry out numerical continuation of large algebraic systems, including fold and bifurcation point detection and branch switching. We were unable to get satisfactory performance from COCO (see Dankowicz and Schilder (2013)) and AUTO, some of the available continuation codes. These codes appear to be mainly written for ODEs, generally with small numbers of state variables.

There are many helpful resources for understanding numerical continuation, so we wrote our own to do the numerical continuation ourselves. We found Govaerts (2000), Allgower and Georg (2003), and Boyd (2014) to be useful in understanding the methods and writing our own code to implement these algorithms for our problem.

A.1 Pseudo-Arclength Continuation

One basic method of continuation comes from the Davidenko equation. It has been discussed in Govaerts (2000), Boyd (2014), and Allgower and Georg (2003), and it is the type of method used in Luzzatto-Fegiz and Williamson (2011). For some function $\mathbf{F}(\mathbf{x}, \zeta)$, solutions to a continuation problem are those values of $(\mathbf{x}, \zeta)$ for which $\mathbf{F}(\mathbf{x}, \zeta) = 0$. If one considers $\mathbf{x} = \mathbf{x}(\zeta)$, the total derivative of $\mathbf{F}$ with respect to ζ can be

written as

$$\frac{d\mathbf{F}}{d\zeta} = \frac{\partial \mathbf{F}}{\partial \mathbf{x}} \frac{d\mathbf{x}}{d\zeta} + \frac{\partial \mathbf{F}}{\partial \zeta}. \tag{A.1}$$

Along solution branches, $\mathbf{F} = 0$, which implies $d\mathbf{F}/d\zeta = 0$. This gives a method for calculating the tangent vector of the solution family

$$\frac{\partial \mathbf{F}}{\partial \mathbf{x}} \frac{d\mathbf{x}}{d\zeta} = -\frac{\partial \mathbf{F}}{\partial \zeta}. \tag{A.2}$$

Govaerts (2000) writes this equation as

$$\left[\mathbf{F}_x \mathbf{F}_\zeta\right] \mathbf{t} = 0. \tag{A.3}$$

where $\mathbf{t}$ is some scaling of $[d\mathbf{x}/d\zeta; 1]$. This is the tangent vector of the solution families; given some solution, it tells how the function inputs $\mathbf{x}$ change at that point with respect to the pseudo-arclength ζ. The matrix is the Jacobian of $\mathbf{F}$, so $\mathbf{t}$ is the nullspace of the Jacobian. We calculate the Jacobian using the finite difference function in Mikofski (2014). The vector $\mathbf{t}$ can be scaled, and this property is necessary for the continuation method. During continuation, it is important to proceed in the same direction along the solution branch. To do this, we must require $\mathbf{t}$ to maintain its sign. This is enforced through the requirement that

$$\mathbf{t}_0^T \mathbf{t}_1 > 1, \tag{A.4}$$

where $\mathbf{t}_0$ is the previous tangent vector and $\mathbf{t}_1$ is the new tangent vector. This condition ensures that the pseudo-arclength is always increasing.

The actual continuation method uses a predictor-corrector iteration, where the prediction is based on the tangent vector $\mathbf{t}_1$, and the corrector iteration then converges to a solution of the full problem $\mathbf{F}(\mathbf{x}, \zeta) = 0$.

A.1.1 Predictor Step

The predictor step gives the first guess for the solution at a new value ζ. It is necessary to know two things: a previous tangent vector to the solution branch, and the current point on the solution branch. In the beginning, as long as one knows a point, one can choose the previous tangent vector to be very simple (zeros everywhere, with a one in the last place). However, once the code is started, the tangent vector at the last point, $\mathbf{t}_0$, will be known. If the current point is given the label 1, so that we know $\mathbf{F}(\mathbf{x}_1, \zeta_1) = 0$, then the prediction is

$$\begin{bmatrix} \mathbf{F}_x & \mathbf{F}_\zeta \\ \mathbf{t}(x)_0^T & t(\zeta)_0 \end{bmatrix} \begin{bmatrix} \mathbf{t}(x)_1 \\ t(\zeta)_1 \end{bmatrix} = \begin{bmatrix} 0 \\ 1 \end{bmatrix}, \tag{A.5}$$

where we have split the tangent vectors $\mathbf{t}$ into their components from $\mathbf{x}$ and the single component from the parameter ζ. This calculation can be done by calculating the nullspace in Eq. A.3 and then scaling $\mathbf{t}_1$ by the dot product

$$\mathbf{t}_0^T \mathbf{t}_1 = 1. \tag{A.6}$$

The step length can be further adjusted by choosing some scaling factor. This scaling factor can be chosen or set by an algorithm. Govaerts (2000) also suggests adjusting it based on the number of Newton iterations required for a solution, where if it takes too many, the step size is halved, but if it converges in 3 or less iterations, the step size is increased. Given some scaling factor Δl, the predicted solution is

$$\begin{bmatrix} \mathbf{x}^0 \\ \zeta^0 \end{bmatrix} = \begin{bmatrix} \mathbf{x}_1 \\ \zeta_1 \end{bmatrix} + \Delta l \begin{bmatrix} \mathbf{t}(x)_1 \\ t(\zeta)_1 \end{bmatrix}. \tag{A.7}$$

A.1.2 Corrector Iteration

Using the prediction $(\mathbf{x}^0, \zeta^0)$, we calculate the actual solution by using a Gauss-Newton iteration to correct the guess. This involves the solution of two problems, if one is to use the minimum norm solution, as in Govaerts (2000). The main correction is the standard one for the main problem,

$$\begin{bmatrix} \mathbf{F}_x & \mathbf{F}_\zeta \\ \mathbf{t}(x)_1^T & t(\zeta)_1 \end{bmatrix} \begin{bmatrix} \Delta_1 x \\ \Delta_1 \zeta \end{bmatrix} = \begin{bmatrix} -\mathbf{F} \\ 0 \end{bmatrix}. \tag{A.8}$$

However, for the kth step, the full corrector is

$$\begin{bmatrix} \Delta x^k \\ \Delta \zeta^k \end{bmatrix} = \begin{bmatrix} \Delta_1 x \\ \Delta_1 \zeta \end{bmatrix} + \eta \begin{bmatrix} \mathbf{t}(x)_k \\ t(\zeta)_k \end{bmatrix}, \tag{A.9}$$

where $\mathbf{t}_k$ is calculated from

$$\begin{bmatrix} \mathbf{F}_x & \mathbf{F}_\zeta \\ \mathbf{t}(x)_1^T & t(\zeta)_1 \end{bmatrix} \begin{bmatrix} \mathbf{t}(x)_k \\ \mathbf{t}(\zeta)_k \end{bmatrix} = \begin{bmatrix} 0 \\ 1 \end{bmatrix}, \tag{A.10}$$

and

$$\eta = -\frac{(\Delta_1 x)^T \mathbf{t}(x) + (\Delta_1 \zeta) t(\zeta)}{\|\mathbf{t}\|^2} \tag{A.11}$$

A.2 Bifurcation Points

While the basics of continuation are outlined above, we also must be able to track where bifurcations occur, and then switch branches to the other solutions.

A.2.1 Locations of Bifurcation Points

A fold point will occur between points 1 and 2 if

$$\mathbf{t}_1^T \mathbf{t}_2 < 0, \tag{A.12}$$

where $\mathbf{t}_i$ is the nullspace of the Jacobian at point i, and we assert that $t(\zeta)_i$, which is the last component of $\mathbf{t}_i$, has a positive value. To check for this in the code, it is important to keep track of the tangent vectors at each point. Also, in the code for solving the actual problem, we scale $\mathbf{t}_{i+1}$ so that $\mathbf{t}_i^T \mathbf{t}_{i+1} = 1$. This won't affect the fold point test, so we can save the scaled tangent vectors, and then multiply by -1 if necessary before running the fold point test.

The bifurcation point test is similar to the fold point (with a similar condition on the value of $t(\zeta)$. The test (from Allgower and Georg (2003)) involves checking if

$$\det \begin{pmatrix} \mathbf{F}_x & \mathbf{F}_\zeta \\ \mathbf{t}(x)^T & t(\zeta) \end{pmatrix} \tag{A.13}$$

changes sign between steps.

These tests don't give the actual location of the fold and bifurcation points. Instead, they indicate whether the bifurcation or fold point occurs between each set of two points. Once we know which regions have fold and bifurcation points, we use a perturbation method to switch branches, and then can calculate the location of the bifurcation points based on the intersection of the two solution branches.

A.2.2 Switching Branches

There are many elegant ways to switch branches once a bifurcation point has been located. Allgower and Georg (2003) points out that the nullspace of the Jacobian will be of dimension 2 at the bifurcation points, so to switch branches, one need only to use the other tangent vector. Boyd (2014) suggests using a Cauchy or Shafer iteration near bifurcation points, since the second root of these methods will follow the other branch near the bifurcation point. However, these methods require the calculation of higher order derivatives. As Boyd (2014) and others mention, we only need a single point on the other branch. After that, we can use normal continuation to calculate the rest of the branch.

Transcritical bifurcation points occur only at specific points in the solution space. If we add a perturbation to the system, we don't expect the bifurcation points to remain; instead, the families will now curve between the perturbed solutions on one branch into perturbed solutions of the other branch. If we plot the perturbed solution families, where the bifurcation point would have been is now an avoided crossing (Boyd (2014), Allgower and Georg (2003)). Using this idea, we developed a method to perturb the problem in the area of bifurcation points and then move backward along the perturbed solution to get to the new branch.

For instance, assume we have a solution branch along with we had run the continuation algorithm. At the end, we have a list of locations for bifurcation points, fold points, and the pseudo-arclength step size. If we know that a bifurcation occurs between points labeled i and $i-1$, and we know that the step size at i was $\Delta l^{(i)}$, we can reverse the direction of traversing by setting our new step size to be $\Delta l_p^{(i)} = -\Delta l^{(i)}$. Our original branch was the solution to

$$\mathbf{F} = 0. \tag{A.14}$$

In the new, perturbed solution space, our equation becomes

$$\mathbf{F} - \mathbf{p} = 0, \tag{A.15}$$

where $\mathbf{p}$ is some constant perturbation vector (for our case, we simply chose a vector like $p_j = 10^{-3}$ for all j). The actual perturbation is unimportant. It is only required to get a starting point to the actual problem on the bifurcating branch.

In the first iteration, we don't do a predictor step, instead starting with the solution at point i to Eq. A.14, and then use our Gauss-Newton solver to get the solution to Eq. A.15. From there, we use the standard predictor-corrector method, but solving the perturbed equation this time, and with our perturbed step size $\Delta l_p^{(i)}$. After covering a specified pseudo-arclength (or if the solver fails), the continuation of the perturbation is stopped.

The next step is not automated, but involves looking at the solutions to the perturbed equation and selecting those that appear to be on the other branch and also are good solutions. Since we are working with perturbed solutions, we found that they tend to have spurious portions quickly, so we tried to choose solutions that appeared good. Using these good points as starting points, we plugged them back into the original continuation code, again with the first iteration using no prediction but instead just starting from the perturbed solution and using the Gauss-Newton solver to converge to the solution to the original equation. As long as this point is on the new solution branch, and not the previous one, we can then run the numerical continuation on the new solution branch.

Bibliography

Adrian, J. R., Christensen, T. K., and Liu, Z.-C. (2000). Analysis and interpretation of instantaneous turbulent velocity fields. *Exp. Fluids*, 29(3):275–290.

Allgower, E. and Georg, K. (2003). *Introduction to Numerical Continuation Methods*. Society for Industrial and Applied Mathematics, Philadelphia, PA.

Ardalan, K., Meiron, D. I., and Pullin, D. I. (1995). Steady compressible vortex flows: the hollow-core vortex array. *J. Fluid Mech.*, 301:1–17.

Baker, G. and Nachbin, A. (1998). Stable methods for vortex sheet motion in the presence of surface tension. *SIAM J. Sci. Comp.*, 19(5):1737–1766.

Baker, G. R., Meiron, D. I., and Orszag, S. A. (1982). Generalized vortex methods for free-surface flow problems. *J. Fluid Mech.*, 123:477–501.

Baker, G. R., Saffman, P. G., and Sheffield, J. S. (1976). Structure of a linear array of hollow vortices of finite cross-section. *J. Fluid Mech.*, 74:469–476.

Batchelor, G. K. (1956a). On steady laminar flow with closed streamlines at large Reynolds number. *J. Fluid Mech.*, 1:177–190.

Batchelor, G. K. (1956b). A proposal concerning laminar wakes behind bluff bodies at large Reynolds number. *J. Fluid Mech.*, 1:388–398.

Boyd, J. (2014). *Solving Transcendental Equations*. Society for Industrial and Applied Mathematics, Philadelphia, PA.

Bunyakin, A. V., Chernyshenko, S. I., and Stepanov, G. Y. (1996). Inviscid Batchelor-model flow past an airfoil with a vortex trapped in a cavity. *J. Fluid Mech.*, 323:367–376.

Bunyakin, A. V., Chernyshenko, S. I., and Stepanov, G. Y. (1998). High-Reynolds-number Batchelor-model asymptotics of a flow past an aerofoil with a vortex trapped in a cavity. *J. Fluid Mech.*, 358:283–297.

Chernyshenko, S. I. (1998). Asymptotic theory of global separation. *Appl. Mech. Rev.*, 51(9):523–536.

Chernyshenko, S. I., Galletti, B., Iollo, A., and Zannetti, L. (2003). Trapped vortices and a favourable pressure gradient. *J. Fluid Mech.*, 482:235–255.

Crowdy, D. G. and Green, C. C. (2011). Analytical solutions for von Kármán streets of hollow vortices. *Phys. Fluids*, 23:126602.

Dankowicz, H. and Schilder, F. (2013). *Recipes for Continuation*. Society for Industrial and Applied Mathematics, Philadelphia, PA.

Deem, G. S. and Zabusky, N. J. (1978). Vortex waves: stationary "V states", interactions, recurrence and breaking. *Phys. Rev. Lett.*, 40:859–862.

Elcrat, A., Fornberg, B., and Miller, K. (2001). Some steady axisymmetric vortex flows past a sphere. *Journal of Fluid Mechanics*, 433:315–328.

Gallizio, F., Iollo, A., Protas, B., and Zannetti, L. (2010). On continuation of inviscid vortex patches. *Physica D: Nonlinear Phenomena*, 239(3-4):190–201.

Govaerts, W. (2000). *Numerical Methods for Bifurcations of Dynamical Equilibria*. Society for Industrial and Applied Mathematics, Philadelphia, PA.

Green, C. (2013). *Mathematical techniques for free boundary problems with multiple boundaries*. PhD thesis, Imperial College London.

Head, M. R. and Bandyopadhyay, P. (1981). New aspects of turbulent boundary-layer structure. *J. Fluid Mech.*, 107:297–338.

Hou, T. Y., Lowengrub, J. S., and Shelley, M. J. (1997). The long-time motion of vortex sheets with surface tension. *Phys. Fluids*, 9(7):1933–1954.

Jiménez, J., Wray, A. A., Saffman, P. G., and Rogallo, R. S. (1993). The structure of intense vorticity in isotropic turbulence. *J. Fluid Mech.*, 255:65–90.

Kamm, J. R. (1987). *Shape and stability of two-dimensional uniform vorticity regions*. PhD thesis, California Institute of Technology.

Lamb, H. (1932). *Hydrodynamics*. Cambridge University Press, Cambridge, sixth edition.

Leppington, F. G. (2006). The field due to a pair of line vortices in a compressible fluid. *J. Fluid Mech.*, 559:45–55.

Llewellyn Smith, S. G. and Crowdy, D. G. (2012). Structure and stability of hollow vortex equilibria. *J. Fluid Mech.*, 691:178–200.

Luzzatto-Fegiz, P. and Williamson, C. H. (2011). An efficient and general numerical method to compute steady uniform vortices. *J. Comput. Phys.*, 230(17):6495 – 6511.

Luzzatto-Fegiz, P. and Williamson, C. H. K. (2012). Determining the stability of steady two-dimensional flows through imperfect velocity-impulse diagrams. *J. Fluid Mech.*, 706:323–350.

McLean, J. W. and Saffman, P. G. (1981). The effect of surface tension on the shape of fingers in a Hele Shaw cell. *J. Fluid Mech.*, 102:455–469.

Mikofski, M. (2014). Newton-Raphson solver. `https://www.mathworks.com/matlabcentral/fileexchange/43097-newton-raphson-solver/content/newtonraphson.m`. Retrieved jacobian function December 2015.

Miyazaki, T., Imai, T., and Fukumoto, Y. (1995). Three-dimensional instability of Kirchhoff's elliptic vortex. *Phys. Fluids*, 7(1):195–202.

Moore, D. W. and Pullin, D. I. (1987). The compressible vortex pair. *J. Fluid Mech.*, 185:171–204.

Moore, D. W. and Saffman, P. G. (1971). Structure of a line vortex in an imposed strain. In Olsen, J. A., Goldburg, A., and Rogers, M., editors, *Aircraft wake turbulence and its detection*, pages 339–354, New York. Plenum.

Nie, Q. (2001). The nonlinear evolution of vortex sheets with surface tension in axisymmetric flows. *J. Comput. Phys.*, 174(1):438 – 459.

Overman, E. A. (1986). Steady-state solutions of the Euler equations in two dimensions II. Local analysis of limiting V-states. *SIAM J. Appl. Math.*, 46(5):765–800.

Pocklington, H. C. (1895). The configuration of a pair of equal and opposite hollow straight vortices of finite cross-section, moving steadily through fluid. *Proc. Camb. Phil. Soc.*, 8:178–187.

Pullin, D. I. (1982). Numerical studies of surface-tension effects in nonlinear Kelvin-Helmholtz and Rayleigh-Taylor instability. *J. Fluid Mech.*, 119:507–532.

Rangel, R. H. and Sirignano, W. A. (1988). Nonlinear growth of Kelvin-Helmholtz instability: Effect of surface tension and density ratio. *Phys. Fluids*, 31(7):1845–1855.

Robinson, A. C. and Saffman, P. G. (1984). Three-dimensional stability of an elliptical vortex in a straining field. *J. Fluid Mech.*, 142:451–466.

Sadovskii, V. S. (1971). Vortex regions in a potential stream with a jump of Bernoulli's constant at the boundary. *App. Math. Mech.*, 35:729–735.

Saffman, P. G. (1992). *Vortex dynamics*. Cambridge University Press, Cambridge.

Saffman, P. G. and Tanveer, S. (1982). The touching pair of equal and opposite uniform vortices. *Phys. Fluids*, 25(11):1929–1930.

Saffman, P. G. and Tanveer, S. (1984). Prandtl-Batchelor flow past a flat plate with a forward-facing flap. *J. Fluid Mech.*, 143:351–365.

Tanveer, S. (1986). The effect of surface tension on the shape of a Hele-Shaw cell bubble. *Phys. Fluids*, 29(11):3537–3548.

Vanden-Broeck, J.-M. (1991). *Gravity-Capillary Free Surface Flows*. Springer US, New York.

Winant, C. D. and Browand, F. K. (1974). Vortex pairing : the mechanism of turbulent mixing-layer growth at moderate reynolds number. *J. Fluid Mech.*, 63:237–255.

Zabusky, N. J., Hughes, M., and Roberts, K. (1979). Contour dynamics for the Euler equations in two dimensions. *J. Comput. Phys.*, 30(1):96 – 106.

Zannetti, L. (2006). Vortex equilibrium in flows past bluff bodies. *J. Fluid Mech.*, 562:151–171.

Zannetti, L. and Iollo, A. (2003). Passive control of the vortex wake past a flat plate at incidence. *Theor. Comp. Fluid Dyn.*, 16(3):211–230.

Zannetti, L. and Lasagna, D. (2013). Hollow vortices and wakes past Chaplygin cusps. *Eur. J. Mech. B/Fluids*, 38(0):78 – 84.